Title
A Computational Assessment of Solar Fuels-Producing Devices from Thermal, Optical and Energy Yield Perspectives

Author
Stevens, John

Publication Date
2015

Peer reviewed|Thesis/dissertation

A COMPUTATIONAL ASSESSMENT OF SOLAR FUELS-PRODUCING DEVICES FROM THERMAL, OPTICAL AND ENERGY YIELD PERSPECTIVES

By

John Colby Stevens

A dissertation submitted in partial satisfaction of the requirements for the degree of

Doctor of Philosophy

in

Engineering – Mechanical Engineering

And the Designated Emphasis

in

Energy Science and Technology

in the

Graduate Division

of the

University of California, Berkeley

Committee in charge:

Professor Tarek I. Zohdi, Chair
Professor Van P. Carey
Professor Duncan Callaway
Doctor Frances Houle

Fall 2015

A Computational Assessment of Solar Fuels-Producing Devices from Thermal, Optical and Energy Yield Perspectives

Abstract

A Computational Assessment of Solar Fuels-Producing Devices from Thermal, Optical and Energy Yield Perspectives

by

John Colby Stevens

Doctor of Philosophy in Engineering – Mechanical Engineering

and the Designated Emphasis

in

Energy Science and Technology

University of California, Berkeley

Professor Tarek Zohdi, Chair

The use of optically concentrating lenses integrated with wireless photoelectrochemical cells provides a mechanism to potentially reduce the energy input required to manufacture solar fuels-producing devices. In this work, a modeling approach is used to assess the annual fuel production from such integrated devices. The model captures optical, heat transfer, photoelectrochemical and climactic phenomena. The variation of design parameters such as cell dimensions, lens type, photovoltaic cell type, optical reflection management coatings and deployment location is investigated for a system that uses an optical concentration ratio of 10. The model then predicts the system's operating temperature, operating current density and solar fuel production efficiency for every hour of the year in any location for which sufficient weather data is available.

It is found that the devices that perform most efficiently are sufficiently small to enable effective optical capture and minimize potential losses in the electrolyte. Small ion exchange membrane coverage fractions are sufficient to enable optimal light capture while exhibiting small ohmic drops in the photoelectrochemical cell. Careful management of antireflection coatings and protection layers is required to maximize optical transmission to the current-limiting junction in the device's photovoltaic cell. Employing simple passive cooling to maintain sufficiently low cell temperatures during extreme, quiescent ambient conditions can be achieved in certain climates but not in others. Additional measures must be undertaken to prevent electrolyte freezing in colder climates. However, despite these challenges, annual weighted average solar to hydrogen efficiency of 11.2% can be realized in high insolation locations, and stably efficient operation is possible with proper cell

design. Locations with very poor direct solar irradiation resources can still exhibit annual weighted average solar to hydrogen efficiencies in excess of 9%. Additionally, the model's predictions of device temperature are found to be in agreement with results produced in COMSOL Multiphysics. These investigations therefore help to elucidate the potential research and development work needed for future development and deployment of this technology.

Dedication

This dissertation is dedicated to my mother, who encouraged me whenever I needed it, who taught me how to work hard and achieve my goals, and who also taught me that there is no short version of any story. It is also dedicated to my father, who taught me how to laugh, and to appreciate the beauty and wonder of the natural world around me.

Acknowledgements

I would like to thank my family first and foremost for providing support down through the years; without them, I would not be where I am or what I am now. I would also like to thank Dr. Tarek Zohdi, for his guidance and assistance, and for teaching me how to code. I thank Dr. Adam Weber for keeping me "out of the weeds" whenever possible, and for providing frank discussions when I needed them. I thank Dr. Frances Houle for her assistance and understanding as I moved towards my graduation. I thank Dr. Duncan Callaway for teaching me about potential ways to integrate more renewable energy in the grid, and I thank Dr. Van Carey for teaching me to have a deeper understanding of many heat transfer-related processes. Finally, I thank my friends at UC Berkeley and the Joint Center for Artificial Photosynthesis; without you, I would have enjoyed life a lot less throughout graduate school.

Portions of this Dissertation have been drawn from the following publications:

J. C. Stevens and A. Z. Weber, "A computational study of optically concentrating, solar fuels-producing devices from annual thermal and fuel production efficiency performance perspectives", Manuscript in Preparation.

R. Sathre, C. Scown, R. Morrow III, J. C. Stevens, I. Sharp, J. Ager III, K. Walczak, F. Houle and J. Greenblatt, "Life-Cycle Net Energy Assessment of Large-Scale Hydrogen Production via Photoelectrochemical Water Splitting," *Energy Environ. Sci.*, no. 7 (2014): 3264–78, doi:10.1039/C4EE01019A.

M. R. Singh, J. C. Stevens, and A. Z. Weber, "Design of Membrane-Encapsulated Wireless Photoelectrochemical Cells for Hydrogen Production," *Journal of the Electrochemical Society* 161, no. 8 (2014): E3283–96, doi:10.1149/2.033408jes.

Chapter 1: Introduction

1.1 Motivation: Why Should We Develop Devices for Producing Renewable Chemical Fuels?

The high standard of living that many humans strive for and others already enjoy relies upon sustained economic growth. Since the advent of the industrial revolution, this growth has been driven by harnessing inexpensive fossil fuels to power our society[1]. The sustained demand for fossil fuels due to economic and population growth factors will speed the development of unconventional sources of oil, of which there is an enormous remaining supply. If even a modest fraction of the remaining fossil fuel reserves are used, the environmental harm resultant from unconventional and conventional fossil fuel extraction, refining and combustion will reduce the quality of life for many people as the effects of global climate change become more pronounced for coming generations[2,3]. A potential solution that can reduce the emissions of greenhouse gases while still enabling sustained economic growth lies in the development of inexpensive renewable energy that can take the place of fossil fuels[1].

There are many renewable energy-harvesting technologies that will be deployed as the price of these technologies declines. Wind energy is likely to lead this drive, and is estimated to overtake hydroelectric energy generation as the largest source of renewable energy in the U.S. by 2040[4]. However, all renewable energy technologies aside from geothermal energy harvest solar energy either directly or indirectly and, as such, are intermittent in nature. This intermittency is not aligned with the energy demand profiles of an industrialized society. Thus, the need for a means of storing energy becomes paramount if we are to deploy renewable energy on a scale that facilitates a meaningful reduction in anthropogenic greenhouse gas emissions[5].

There are numerous means for storing energy. These can be broken down into basic classes: electrochemical, electrical, thermal, mechanical and chemical means. Electrochemical storage includes conventional batteries and flow batteries, which perform coupled redox reactions in order to store and extract electrical energy. Electrical storage methods include capacitors and other means to maintain an internal electrical field in a system until the release of that stored energy is desired. Thermal energy storage involves creating thermal reservoirs whose temperature difference relative to the surrounds or one another can be harnessed in a heat engine (often a device operating on a Rankine cycle). Thermal energy storage can also be used to displace the later use of energy required to heat or cool some system, for example through storing chilled water at night to reduce air conditioning system power demand during the daytime. Potential mechanical energy systems include pumped hydroelectric systems, fly wheels, compressed air energy storage

systems and other means of storing energy as kinetic or potential mechanical energy. Chemical storage can take the form of, for example, hydrogen, biofuels, solar fuels and other chemically reduced compounds that can be oxidized via combustion or other processes to release energy for use at a later point. Each of these storage means has its merits and detractors, as well as applications for which it is most appropriate. The following discussion will narrow in focus to chemical and electrochemical energy storage means.

The ease of decarbonizing a sector of the global economy varies. In particular, the global transportation sector does and will derive its primary energy from the direct combustion of hydrocarbons. This is illustrated in Figure 1.1. In 2010, less than 1% of the primary energy utilized directly for global transportation was from electricity; the rest was derived from the combustion of hydrocarbons. By 2040, the total global transportation energy sourced from electricity is still projected to be less than 2%, even if high oil prices are assumed to be the norm[6]. In 2012, transportation comprised 22% of the global anthropogenic greenhouse gas emissions associated with fuel combustion[7]. This is shown in Figure 1.2. Even assuming high oil prices, the global transportation sector's primary energy consumption is still projected to increase by over 44% compared to 2010 values by 2040[6].

From the above, it is evident that transportation comprises a huge source of global carbon dioxide emissions that is set to increase dramatically in the next 25 years. These data are inherently error-prone projections, but the underlying reason for the difficulty of using fuels other than hydrocarbons for transportation energy is rather simple. The extremely high specific energy capacity (as measured in units of energy per unit mass) and low specific storage cost (as measured in units of cost per unit of stored energy) of hydrocarbons is vastly superior to the alternatives.

Even given probable advancements in battery technology and the greater efficiency of electric motors versus internal combustion engines, it is unlikely that there will ever be a meaningful switch to electric propulsion in the transportation sector. This is because fossil fuels have 1-2 orders of magnitude higher specific energy storage capacity than batteries, and are 4 orders of magnitude less expensive, as shown in Figure 1.3. The specific energy storage capacity of gasoline is roughly 12,000 Wh/kg. This compares to the theoretical energy density of roughly 1,100 Wh/kg for commonly used LiCoO2 cathode/LiC6 anode batteries[8]. Typical vehicular battery packs exhibit specific energy storage capacities on the order of 100 Wh/kg[1]. The cost for vehicular battery packs is on the order of $US 500/kWh in 2015 dollars[9], versus $0.075/kWh for gasoline at average U.S. retail prices, at the time of writing[10]. Batteries are prohibitively expensive, heavy and have insufficient energy storage capacity for most transportation applications. Thus, one must find a means to convert and store renewable energy in the form of such fuels if one is to decarbonize the global transportation sector.

Currently, biofuels represent the largest portion of the transportation sector's primary energy not directly derived from fossil fuel combustion. Ethanol composed 4.2% of the primary transportation energy in the U.S. in 2013, most of which is derived from corn and blended into motor vehicles[11]. However, the

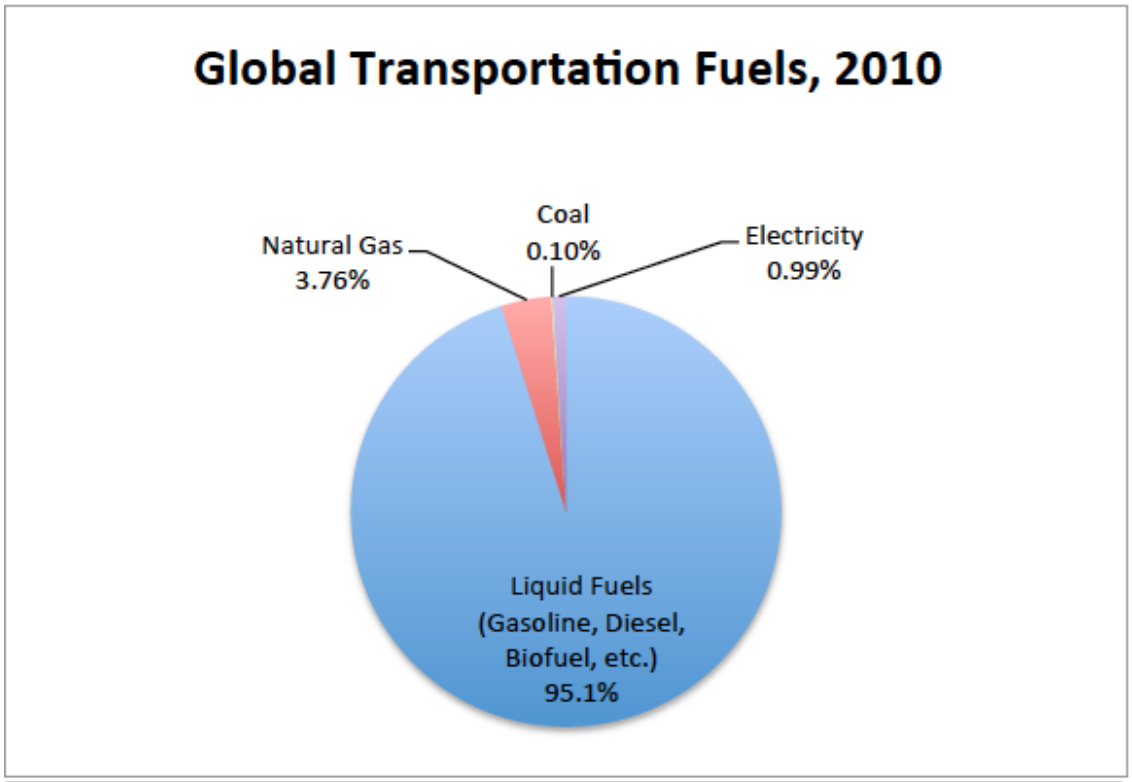

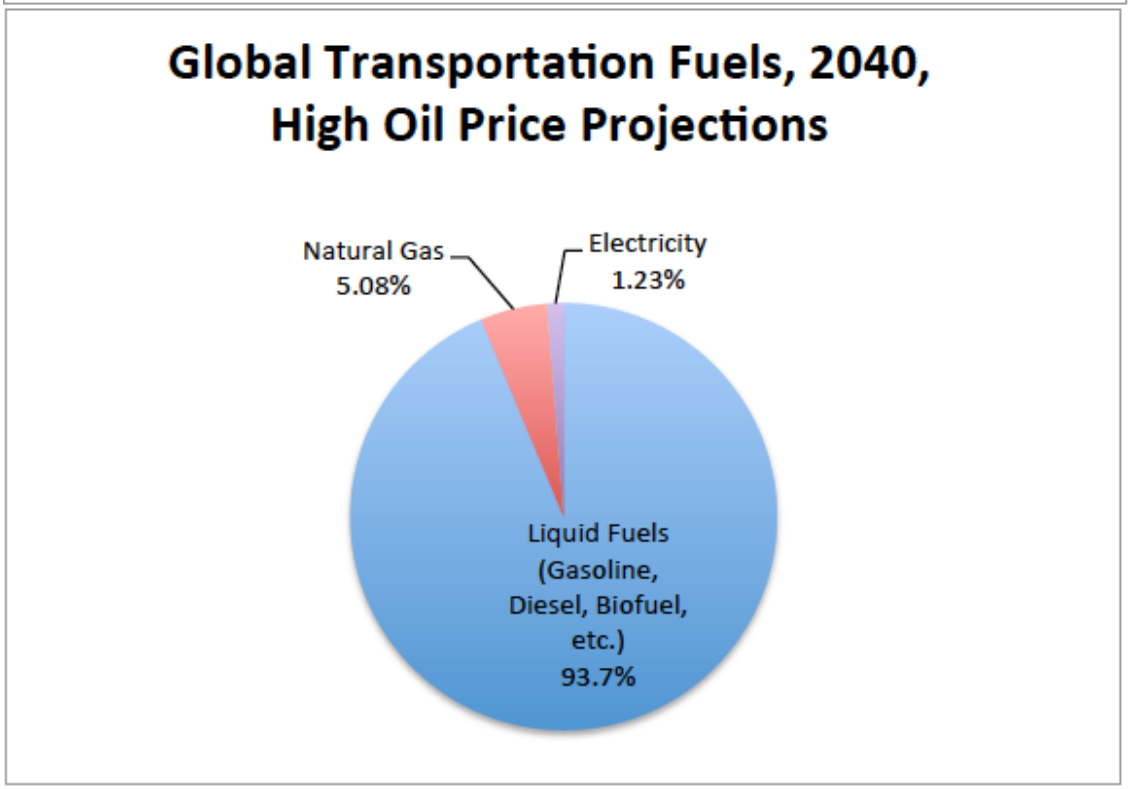

Figure 1.1: Global Transportation Fuel Sources, 2010 and Projected 2040[6]

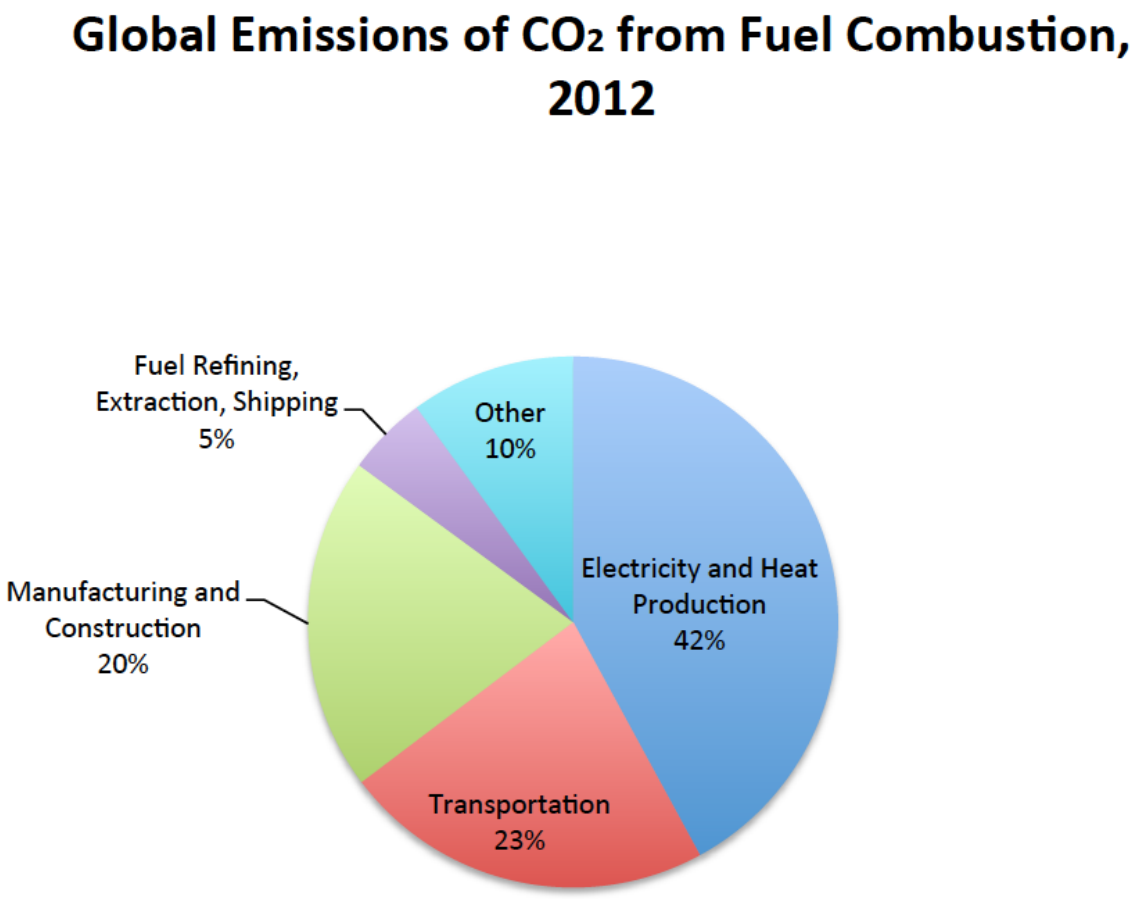

Figure 1.2: Global Carbon Dioxide Emissions from Fuel Combustion by Sector[7]

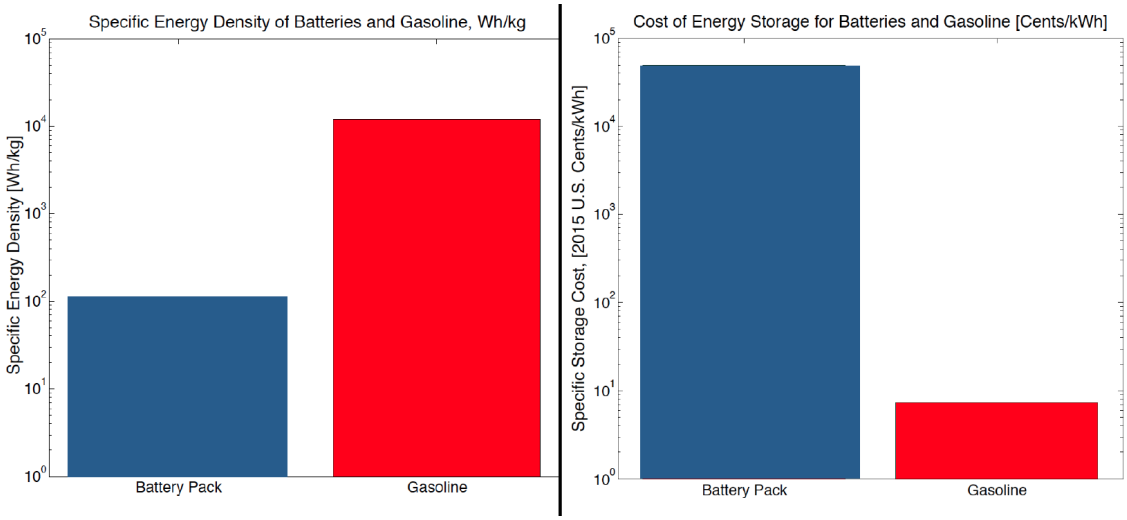

Figure 1.3: Battery Pack vs. Gasoline Specific Energy Storage[8] **and Cost of Energy Storage**[9]

viability of corn-derived ethanol as a sustainable alternative to fossil fuels is questionable.

Studies suggest that anywhere from somewhat less to significantly more energy is required to produce a unit of corn-derived ethanol than is stored in the fuel[12]. For example, Pimentel[13] calculated that 29% more energy is required to produce corn-derived ethanol than is stored in the fuel. Others, such as von Blottnitz and Curran[14], suggest the opposite, estimating that roughly 23% more energy is stored in corn-derived ethanol than is required to produce it. Any renewable energy technology must be significantly energy positive over its life cycle for it to be a viable technology. Turning to greenhouse gas emissions, using the optimistic results from von Blottnitz and Curran[14] and values on ethanol production efficacy from Pimentel[13] indicates that producing a unit of corn-derived ethanol avoids 42% of the greenhouse gases emitted in the combustion of ethanol. Other studies suggest this value is closer to 18%[12]. Clearly, the latter figure represents a rather small decrease in overall emissions. It should be noted that other biofuels, in particular ethanol derived from sugar cane, are far more effective from an energy balance and greenhouse gas abatement standpoint[14].

Looking at biofuels from a food security standpoint paints a more unambiguously negative picture. In 2010, approximately 40% of the U.S. corn crop was used for ethanol production[15], resulting in roughly 4% of the total 2010 U.S. transportation energy[16]. At that conversion and fuel consumption rate, to supply the entire U.S.'s transportation fuel needs with corn-derived ethanol would require roughly 400% of the U.S. land allocated towards grain crop production (corn, soybeans, wheat and rice) in 2011[17]. The reason for this poor performance is that most food crops convert sunlight into carbohydrates at *less than 1% average annual efficiency*[18]. At those conversion rates, an enormous amount of land would have to be allocated to growing enough biofuels to replace humanity's growing demand for liquid hydrocarbon transportation fuels. Plants evolved to successfully reproduce at all costs, not to convert sunlight, water and carbon dioxide into fuel as efficiently as possible. Relying on them to satisfy humanity's appetite for transportation fuel while still attempting to feed an increasing population of ever more affluent humans would be a harsh lesson in thermodynamics.

We are left with relatively few options to renewably synthesize chemical transportation fuels. The produced fuel needs to pass the metrics of sustainability that biofuels and batteries often fail. The device used to produce the fuel must convert significantly more renewable energy into fuel than is required to produce, operate and decommission said device. The device must produce very little greenhouse gas emissions per unit of produced fuel. The fuel must have high specific energy storage capacity. It must also require much less land to produce a unit of fuel than biofuel production methods. And, most importantly, the device must be capable of producing a fuel that can eventually compete economically with conventional fossil fuels. One potential method to deliver such a fuel is with solar fuels-producing, photoelectrochemical cells (PECs).

1.2 An Introduction to Photoelectrochemical Devices

1.2.1 Basics of Electrochemical Processes

PECs convert solar energy into the chemical energy stored in a fuel. All PECs first collect sunlight and convert it into electrical energy using photovoltaic (PV) cells. Most demonstrated systems then convert this electrical energy into chemical energy by splitting water into hydrogen and oxygen. A small fraction of demonstrated devices use the captured solar energy to produce hydrocarbons, using water and carbon dioxide as inputs. As such, all PECs convert hydrocarbon combustion products back into chemical fuels, using photoelectrochemical processes.

The basic electrochemical processes involved in water-splitting PECs that produce hydrogen fuel proceed in two half-reactions, one at an anode (where electron holes generated by the PV cell oxidize the reactants) and the other at a cathode (where electrons generated by the PV reduce the reactants). Figure 1.4 shows a typical PEC, with the light absorption, electron-hole pair generation and migration processes, as well as the reduction and oxidization reactions illustrated.

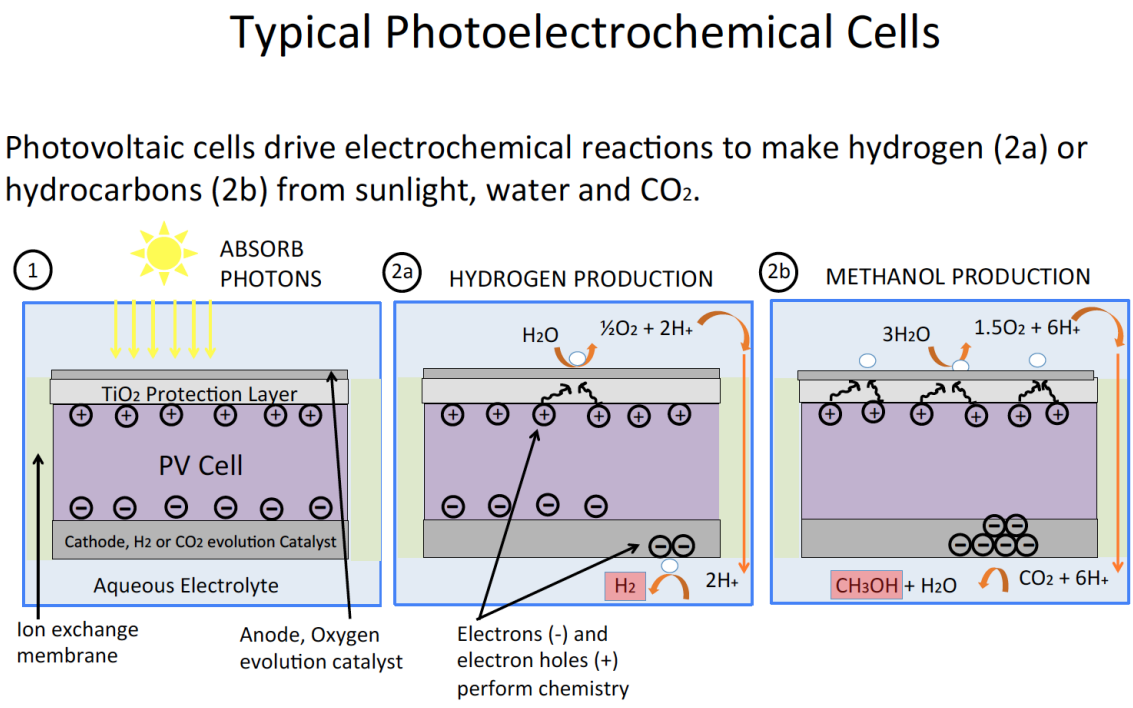

Figure 1.4: Typical Wireless Photoelectrochemical Cell Architecture and Chemical Processes

Though all PECs operate utilizing water as their input, this water is delivered to the anode and cathode in the form of an electrolyte, typically forming a strong acid or base. The reasons for this will be made clear shortly. The reaction pathway for fuel generation in PECs depends on whether the electrolytic medium is acidic or alkaline. In PECs that produce only hydrogen and oxygen as products and that utilize acidic media, the water-splitting reaction can be understood using three simplified reaction steps. In the first step, in order to produce 1 molecule of oxygen

gas and 2 molecules of hydrogen gas, $4n_J$ photons above the band gap energy of the PV cell must be absorbed to create 4 electron holes (h^o) and 4 electrons (e^-), where n_J is the number of junctions in the PV cell (details of PV cell operation will be discussed in Chapter 3),

$$4n_J h\nu \rightarrow 4h^o + 4e^-. \quad (1.1)$$

In step 2, the electron holes are employed to oxidize (remove electrons from) the water at the anode as follows,

$$4h^o + 2H_2O_{(l)} \rightarrow O_2 + 4H^+. \quad (1.2)$$

In step 3, the electrons produced in step 1 reduce (donate electrons to) the 4 hydrogen ions produced in step 2 at the cathode as follows,

$$4e^- + 4H^+ \rightarrow 2H_{2\,(g)}, \quad (1.3)$$

Alternatively, in alkaline media, the water-splitting reaction proceeds again with step 1 outlined above, followed by the reduction of water at the cathode to produce hydroxyl ions (OH-) and hydrogen,

$$4e^- + 4H_2O \rightarrow 2H_{2\,(g)} + 4OH^-. \quad (1.4)$$

The hydroxyl ions are transported to the anode, where they are oxidized as follows,

$$4h^o + 4OH^- \rightarrow 2H_2O_{(l)} + O_{2\,(g)}. \quad (1.5)$$

Regardless of the pH of the electrolyte in which the water-splitting reaction occurs, the overall reaction, which is the sum of the two half reactions, is

$$4h^o + 4e^- + 2H_2O \rightarrow 2H_{2\,(g)} + O_{2\,(g)}. \quad (1.6)$$

PECs that produce hydrocarbon products can utilize many different reaction pathways, depending on the product. A more full description of these pathways can be found elsehwhere[19]. Products that are commonly produced via electrochemical reduction are carbon monoxide, formate, formaldehyde, methanol, methane and ethylene. For example, as illustrated in Figure 1.4, the overall reaction forming ethanol begins with the generation of 6 electron-hole pairs,

$$6n_J h\nu \rightarrow 4h^o + 6e^- \quad (1.7)$$

Following this, (in acidic media), water is oxidized at the anode to release protons and oxygen

$$6h^o + 3H_2O_{(l)} \rightarrow 1.5O_2 + 6H^+. \quad (1.8)$$

Next, these protons are reduced along with carbon dioxide in multistep processes at the cathode. A one-step reaction that summarizes these processes is,

$$6h^+ + 6e^- + CO_2 \rightarrow CH_3OH_{(l)} + H_2O_{(l)}. \quad (1.9)$$

In most demonstrated systems, a mixture of hydrocarbons is produced simultaneously, though this is not desired, as typically only one chemical product is desired. Reducing the number of products generated during the electrochemical reduction of CO_2 is a subject of intense ongoing research. The reader is directed to Singh, Clark and Bell[19], and its references to more full understand this class of PEC.

1.2.2 Determining Electrode Potential

In order for the reduction and oxidization reactions to occur in any electrochemical system, there must be the passage of electrons between an electrode, and some chemical species in contact with the electrode. Different chemical species at the same temperature and pressure have differing internal energies, referred to as enthalpies of formation. Thus, by conservation of energy, in order for those oxidization and reduction reactions to take place, some energy must be exchanged between the chemical species and the electrodes. This energy takes the form of an applied electrode potential, which is made clear when one considers the units of voltage, Joules/Coulomb of charge passed by the electrodes.

The minimum potential difference applied between the anode and cathode to split water occurs when the reaction is reversible. Because a reversible system is in the system can return to its original state without any net change in the entropy of the system and the surrounds, and one in which in infinitesimal change in the driving force can reverse some thermodynamic process, the minimum useful work done on a reversible system would also equal the maximum useful work obtainable from the system. The maximum useful work derivable from a thermodynamic system is known as the Gibbs free energy. We defining the Gibbs Free Energy for a pure system as

$$G = U + pV - TS, \quad (1.10)$$

which is equivalent to

$$G = H - TS, \quad (1.11)$$

where G is the Gibbs free energy, U is the internal energy, H is the enthalpy, p is the pressure of the system, V is its volume, T is its absolute temperature and S is the entropy of the system. For an isothermal process, the net change in Gibbs free energy in the system from one thermodynamic state to another is given as

$$\Delta G = \Delta H + T\Delta S, \quad (1.12)$$

As the Gibbs free energy is equal to the minimum amount of work that must be performed on an electrochemical system to elicit some chemical change in the system, we can write,

$$\Delta G = -nF\mu_{Th,To}, \tag{1.13}$$

where n is the number of transferred electrons required to form a molecule of a chemical species from reactants at an electrode, F is the Faraday's constant (equal to the magnitude of the electric charge of a mole of electrons, or F ≈ 96,485) and $\mu_{Th,To}$ is the potential difference between the electrode and the reactant species at standard conditions. $\mu_{Th,To}$ is also known as the standard potential of the cell reaction.

To determine the minimum potential that must be applied at standard conditions to split liquid water, we calculate the net change in Gibbs free energy from the products of both half reactions (equations 1.2 and 1.3) to the reactant input for the process (water),

$$\Delta G^o = \Delta H^o + T\Delta S^o =$$

$$\left(\left(0.5H^o_{O_2} + H^o_{H_2}\right) - H^o_{H_2O}\right) - 298.15(\left(0.5S^o_{O_2} + S^o_{H_2}\right) - S^o_{H_2O} \tag{1.14}$$

where the coefficient of ½ denotes the molar quantity of oxygen gas in one mole of water, and the superscript denotes standard entropies and enthalpies of formation. Calculating the energy input to reversibly split 1 mole of liquid water, we obtain,

$$\Delta G^o = 237.19 \text{ kJ/mol}$$

where a positive sign for the Gibbs free energy change denotes an non-spontaneous, or endothermic process. Combining equations 1.13 and 1.15, we obtain,

$$\mu_{Th,To} = -1.229\ V. \tag{1.16}$$

Here, we use the convention laid forth in[20], that a process with a positive potential is spontaneous.

The enthalpy of formation of liquid water is larger in magnitude than the Gibbs free energy for splitting water. If a water-splitting electrochemical process occurred at a net electrode potential of -1.229 volts at standard conditions, extra energy, in the form of heat, must be supplied in order to compensate for the resultant change of entropy in the system. This can be seen by defining the reversible heat released in a reaction, and rearranging equation 1.14

$$Q_{Rev} = -T\Delta S^o = \Delta G^o - \Delta H^o. \tag{1.17}$$

Substituting equation 1.13 into equation 1.17, we obtain,

$$Q_{Rev} = -nF\mu_{Th,To} - \Delta H^{o}. \quad (1.18)$$

Because Q_{Rev} is positive, the net flow of heat must be into the system for a reversible water-splitting process. In an adiabatic system, this would result in a temperature drop of the system over time. We therefore define a thermoneutral potential, $\mu_{Thermoneutral}$, defined as the potential at which no net heat must be supplied or removed from the system in order to maintain isothermal operation. This value can be determined by knowing that

$$Q_{Rxn} = Q_{Rev} + Q_{Irr}, \quad (1.19)$$

where Q_{Irr} is the irreversible heat generated during the reaction. Setting equation 1.19 equal to zero gives us a relation between the reversible and irreversible heat. Using the entropy term in equation 1.17 to determine the value of the irreversible heat, adding it to both sides of equation 1.18 and using the link between electrical and chemical energy demonstrated in equation 1.13, we obtain,

$$\mu_{Thermoneutral} = -\frac{\Delta H^{o}}{nF}. \quad (1.20)$$

For liquid water splitting at standard conditions, we obtain $\mu_{Thermoneutral}$= -1.481 V. Equations 1.19 and 1.20 will be valuable in subsequent chapters of this dissertation for calculating the net heat generated in a system during the water-splitting process.

1.2.3 Calculating System Efficiency

Practical water-splitting (and, indeed, all electrochemical) processes do not occur at the standard potential of the cell reaction, because this potential applies to a reversible process that is in thermodynamic equilibrium. Real electrochemical systems exhibit irreversibility due to ohmic drop in the solution and overpotentials at the electrode surfaces. The ohmic drop is caused by the passage of ionic species involved in a particular reaction through an electrolyte, and by the passage of electrons and electron holes through solid media that have finite electrical resistance. The overpotential at the electrode surfaces is manifested by the need to overcome chemical activation barriers and so disturb the system from a state of equilibrium in order for a transfer of charge between a chemical species and the electrodes to occur at a finite rate. These combined effects can be summarized in a term known as the electrochemical overpotential, or the net difference between the equilibrium and actual potentials at the anode and cathode to elicit a certain flow of electrons from the electrodes to the dissolved chemical species. This is given as

$$\eta = V_{Op} - \mu_{Th,To}, \quad (1.21)$$

where V_{Op} is the net applied potential on the system. Because the change in the Gibbs free energy of the system is unchanged, the overpotential results in reduced

system efficiency. Thus, we define the electrochemical efficiency of a water-splitting system as

$$Eff_{Echem} = \frac{j_{Op}\mu_{Th,To}}{j_{Op}\mathrm{V}_{Op}} = \frac{\mu_{Th,To}}{\mathrm{V}_{Op}}, \tag{1.22}$$

where j_{Op} is the operating current density of the system. This concept will be explored more in Chapter 3. Typically, real water-splitting systems operate at a minimum potential of 1.7 volts[21], thus most system efficiencies are, at maximum, roughly 70% in storing electrical energy in the form of fuel. Total system efficiency in a PEC is also governed by the PV cell efficiency, given as

$$Eff_{PV} = \frac{j_{Op}\mathrm{V}_{Op}}{I_{Sun}}, \tag{1.23}$$

where I_{Sun} is the incident radiation intensity on the PV system from the atmosphere. Actual operational PV cell efficiencies vary considerably, but an upper limit of 46% is the current state of the art for a cell that could perform water splitting [22]. Combining equations 1.22 and 1.23, our maximum possible solar to hydrogen efficiency η_{STH} is given as

$$\eta_{STH,Max} = Eff_{PV}Eff_{Echem} = \frac{j_{Op}\mu_{Th,To}}{I_{Sun}}, \tag{1.25}$$

At the current state of the art, this simple analysis yields a potential $\eta_{STH,Max}$ *of approximately 33%* (neglecting other losses in the system). More in depth analyses put this number at 31%, maximum, with in excess of 25% existing semiconductor materials[23]. And thus is the point of such research: *the efficiency of harvesting solar energy in the form of a fuel using PECs has the potential to be an order of magnitude greater than that of natural photosynthesis*. Thus, the land areas required to replace anthropogenic fossil fuel demand, while still immense, are tractable.

1.2.4 Different Demonstrated and Proposed PECs

Having outlined the basic photoelectrochemical processes in PECs, one must now understand what architecture PECs can be built in to carry out these fuel production reactions. PECs fall into several broad categories. These classify devices by their electrochemical architecture, the type and phase of reactants that they use, and the products they generate. This general discussion is given in more detail in Sathre et al.[24]. Though the definitions differ somewhat, a more full description of the distinctions between PECs can be found in Nielander et al.[25].

The architecture of PECs can be "wired" or "wireless". As shown in Figure 1.5, wired devices are physically integrated, while maintaining chemical isolation between all parts of the photovoltaic cells and the electrolyte[26–32], or can allow contact between the electrolyte and the anodic or cathodic portion of a photovoltaic cell, while performing the corresponding cathodic or anodic reactions, respectively,

on a separate, wired electrode[33]. "Wireless" devices perform electrochemistry directly on the photovoltaic cell's surfaces, either with or without some layer to protect the active semiconductor material from the chemical reactions[34,35]. A more comprehensive list of lab-demonstrated wired and wireless hydrogen-producing devices can be found in Ager et al.[36], which details notable demonstrated hydrogen-producing PECs.

PECs can additionally be classified by the type and phase of the input reactant they use. This is depicted in Figure 1.5, which depicts liquid water fed devices, and Figure 1.6, which depicts a water vapor fed device. Most wireless and wired devices use liquid water as a solvent to form an aqueous electrolyte that is in contact with the electrodes[26,30,34]. Typically, the solute in the electrolyte is a strong acid or base that confers conductivity to the electrolyte to enable ion transport. This must be done because, in order to transport current in an electrolyte, one must maintain an ion rather than an electron flux. In PECs using aqueous basic or acidic electrolyte, hydroxyl ions or protons respectively serve to carry this current. By contrast, pure water is a fairly good insulator. Common electrolytes used in PECs are KOH and NaOH (which form alkaline electrolytes), or H_2SO_4 (which forms acidic electrolyte).

Most demonstrated PECs use liquid electrolyte as an input reactants, but some can operate using gaseous water. The latter devices employ a polymer electrolyte membrane (PEM) in place of an aqueous medium in order to conduct protons or hydroxyl ions from the anode to the cathode. Descriptions of possible ways to design such vapor-fed devices can be found in [21,37]. Without a PEM or liquid electrolyte, the transport of ions is prevented, and thus circuit that an electrochemical cell makes is broken, and the device will not operate.

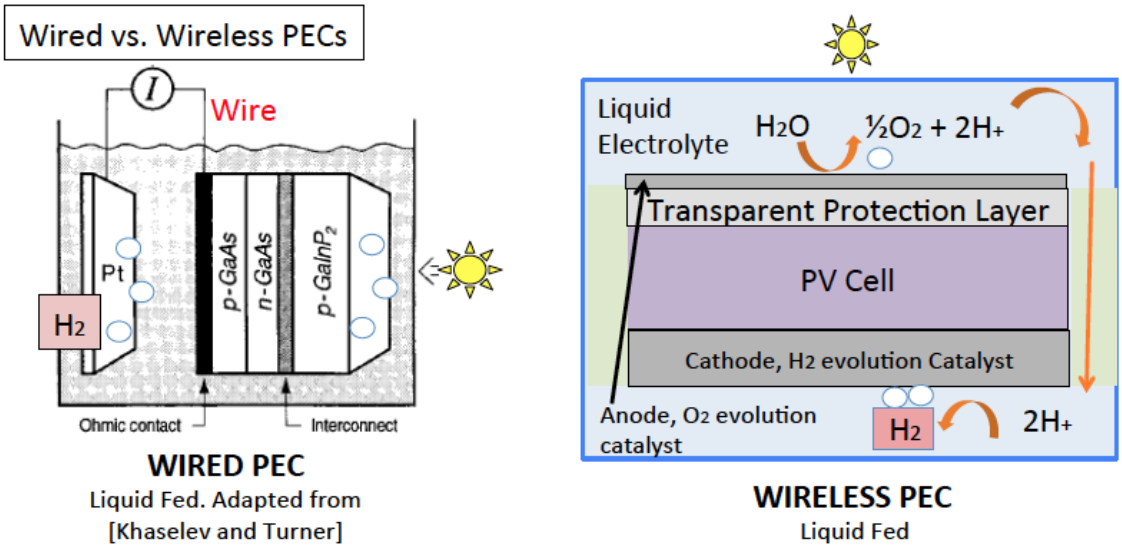

Figure 1.5: Wired vs. Wireless PECs in Liquid Electrolyte

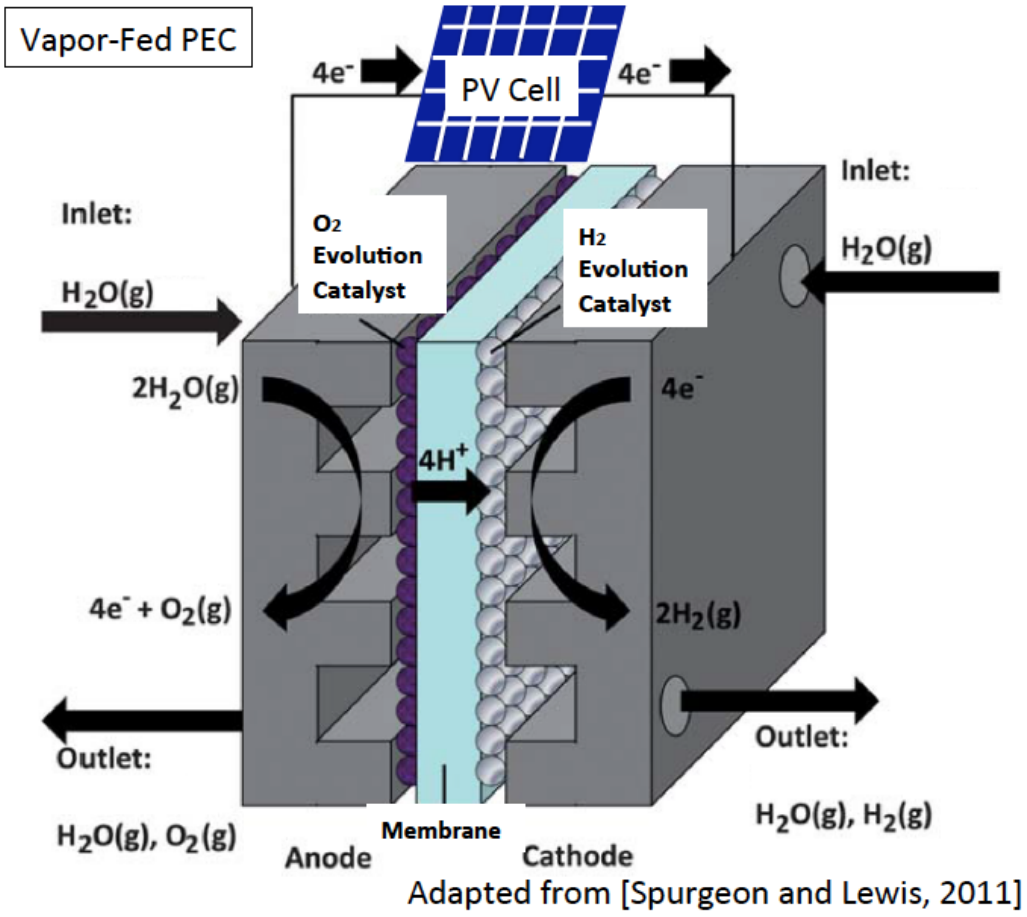

Figure 1.6: Vapor-Fed, Wired PEC

A final method for categorizing PECs is by what products are generated in the cell. All of the demonstrated devices cited above generate hydrogen from water splitting. Electrochemically speaking, this is easier to do than producing hydrocarbon fuels for reasons more fully discussed in[19]. Nevertheless, there exist demonstrated materials that are able to electrochemically reduce carbon dioxide[38]. The one-step reaction pathway for producing methanol is depicted in Figure 1.4.

1.3 Conclusions and Dissertation Organization

PECs have the potential ability to close the anthropogenic carbon emissions cycle associated with the transportation sector, and can potentially do so in a manner that uses an order of magnitude less land than biofuels to yield the same amount of energy stored in chemical fuel. PECs are, however, still essentially in their infancy as a technology. This dissertation aims to shed light on some potential ways in which the technology could be advanced towards deployment, namely by:

- Demonstrating how temperature management in field-deployed devices could be realized and modeled.
- By designing wireless photoelectrochemical devices that use optical concentration to while continuing to operate efficiently.
- By demonstrating novel methods for modeling transport phenomena in PECs, and their ability to predict operating temperatures in vapor-fed PECs and ohmic losses in liquid-fed PECs.

The remaining chapters of this work is organized as follows: in Chapter 2, some of the design challenges for PECs are outlined, and the design challenges associated with reducing PEC's energy payback time are discussed; in Chapter 3, the mathematical means of modeling photoelectrochemical processes as a function of temperature and other variables are elaborated upon; in Chapter 4, the different considerations for modeling the interaction of light with optically concentrating PECs are discussed; in Chapter 5, the mathematical means of constructing a heat transfer model of several different PEC systems are described; in Chapter 6, the results for simulating PECs that use optical concentration from an optical efficiency, operational temperature and hourly fuel yield perspective are shown; and finally, in Chapter 7, conclusions are drawn about this work, and the future prospects for deploying PECs on gigawatt scale are discussed.

Chapter 2: Challenges in Developing Photoelectrochemcial Cells from an Operational and Net Energy Standpoint

2.1 Introduction

In order for PECs to migrate from the laboratory bench top to field deployment, there are numerous design challenges that must be surmounted. Most of the operational challenges in wireless PECs arise from the corrosive operating environment to which a PEC's active materials are exposed. If those obstacles are surmounted, the next challenge will be producing fuels at cost-competitive rates compared to other fuel sources. Finally, in order to produce low-carbon fuel, PECs must be able to deliver significantly more energy than is required to harvest such energy. In this chapter, each of these problems will be touched upon, with the issues pertaining to the net energy harvest of PECs receiving the most attention. The latter issue serves as the motivation for the subsequent research laid forth in this dissertation.

2.2 Corrosion in PECs

2.2.1 Why do We Need Corrosive Electrolyte in a PEC?

If developed successfully as a technology, the production of solar fuels is a promising means of offsetting the use of fossil fuels for transportation. However, surveying the existing literature on lab-demonstrated PECs paints a discouraging picture of the field's commercial viability, for wireless devices in particular. Device lifetime is typically measured in hours, and, at most, days, due to the extremely corrosive environments inside PECs. This section will discuss why the cells must operate in a corrosive electrolyte, how PEC operation exacerbates these issues, and then will review some literature lab-demonstrated prototypes.

Generally speaking, efficient liquid-fed PECs must be operated in a corrosive electrolyte because this is needed to maintain electrical conductivity in the PEC. As explained in Chapter 1, PECs operate by first performing a water-splitting chemical reaction at one electrode, then transporting the product of that reaction, a charged ionic species, through the electrolyte and across a membrane to the opposite electrode, where the species is turned into another product. In order for the system to continue operating efficiently, the flux of the charged species across the membrane must equal the production/consumption rates at the electrodes, or there will be a build up of a net positive charge in the anolyte and a net negative charge in

the catholyte. This build up of charge eventually shuts down the PEC by opposing the polarity of the PV cell [39]. In order to facilitate the equal flux of charged species across the membrane and electrodes, the solution must be made as conductive as possible.

High solution conductivity can be achieved by having an electrolyte with large bulk concentrations of protons (extremely acidic media), or of hydroxyl ions (extremely basic media), or of some supporting electrolyte. In the case of the extremely acidic or basic media, the ions transported across the membrane are also consumed at one of the electrodes and produced at another, thus the total system charge remains neutral. In the case of adding a supporting electrolyte, i.e. an ionic species that is not involved in the water-splitting chemical reactions taking place, there will still be a net build up solution polarization as the anionic and cationic species in the supporting electrolyte gradually are shuttled across the membrane under the imposed potential from the PV cell, but not consumed at the electrode. This can be overcome by periodically mixing the anolyte and catholyte, though this approach has its own drawbacks[39]. Additionally, even in near-neutral solutions, the local pH deviates from that of the bulk electrolyte because of the respective consumption and production of hydroxyl ions at the anode and cathode (in alkaline solution) or the respective local consumption and production of protons at the cathode and anode (in basic solution)[40].

2.2.2 The Curious Case of the Self-Corroding PV Cell

While the extreme pH conditions in the PEC are sufficient to corrode its components when there is no potential applied by the PV cell, the oxidation and reduction processes in PECs are also intrinsically corrosive. PECs employ high electrode potentials (from an electrochemical standpoint) because of the high potential difference across the cell needed perform the water-splitting reaction. However, this same potential can oxidize the PV cell's, the protection layer's or the catalyst's components, rather than oxidizing water or hydroxyl ions.

These combined tendencies allow PECs to corrode themselves unless great care is taken to isolate conventional PV components from the electrochemical reactions. One such way to do this is through the use of an electrically-conducting, optically transparent protection layer[41]. This protection layer is thus employed in the modeling efforts herein. Alternatively, the PV material can be made of a photoactive oxide such as TiO_2, which will not be oxidized at the operational electrode potentials and solution pH. However, oxide semiconductors generally are inefficient at converting sunlight into electrons and holes at the surface of the catalysts due to their high band gaps and poor charge-transport characteristics[42]. Thus, efficient PECs generally have to employ some sort of means of separating the electrochemical reactions and photovoltaic processes. Unfortunately, such protection methods are still being perfected, and pinholes or other points of ingress of the electrolyte to the PV cell through these protection layers will quickly lead to device failure [43].

2.2.3 Demonstrated Examples of PECs

The literature on prototypical PECs shows how short of a lifetime PECs typically exhibit. For a long-lasting example of a wireless device, Reece et al.[44] operated a device in near-neutral electrolyte, employing a triple-junction a-Si cell to perform water wireless water splitting at 2.5% efficiency for 2 hours. High-efficiency systems that split water for long periods of time are invariably wired such that either the anode, cathode or both portions of the PV cell are chemically isolated from the electrolyte. For example, Kelly and Gibson[45] were able to design a 6.2% efficient device that operated in 5 M KOH for 31 days. As the field progresses, these numbers will continue to improve, with works such as Ager et al.[36] serving as useful references for the progress of the field. However, at present, the lifetime of such devices is rather dismal.

2.3 The High Cost of Solar Fuels

Though there are no demonstrated PECs that have produced hydrogen used for large-scale industrial processes, there have been several attempts to estimate the price of fuel that could be produced by PECs. A widely cited technoeconomic analysis[46] estimated for the price of this hydrogen ranging from \$1.60 to \$10.40/kg H_2 for different PEC systems, prior to taxes and other expenses. For reference, 1 kg of H_2 has roughly the same energy content as a US gallon of gasoline. These different devices are depicted in Figure 2.1.

The high cost device utilized a planar, rigid panel operating with no optical concentration. The lowest cost devices employed "baggies" full of suspended particulates that perform water-splitting reactions, either in the same or separated compartments (designs 1 and 2, respectively). The viability of such a baggie reactor solution from a demonstrated lifetime and efficiency[47], and system safety standpoints is dubious, however. The safety issues arise in part because of the coevolution of gaseous products in these reactors, which creates explosive mixtures. This could be overcome by, e.g., diluting the produced gas or by separating the H_2 and O_2 downstream from the reactor, but this would impart significant cost and energy penalties[47]. Another safety issue lies in the use of a flexible baggie. One need only think of what happens when a baggie full of strong electrolyte is pierced by animals, the elements or some other factor and allowed to flow into the environment to realize that this is not a particularly good idea.

The remaining option posited by Pinaud et al.[46] is to use optical concentration to perform water splitting, with an estimated cost of \$4.00/kg H_2. Still expensive, this option is that explored in the following chapters of this dissertation. Generally, the high costs arise from the expensive nature of the PEC's PV cells and catalysts. Reducing the price of PV cells is a general industry goal. Thus, the viability of this technology and others that use PV cells as a key component will potentially be enhanced over time.

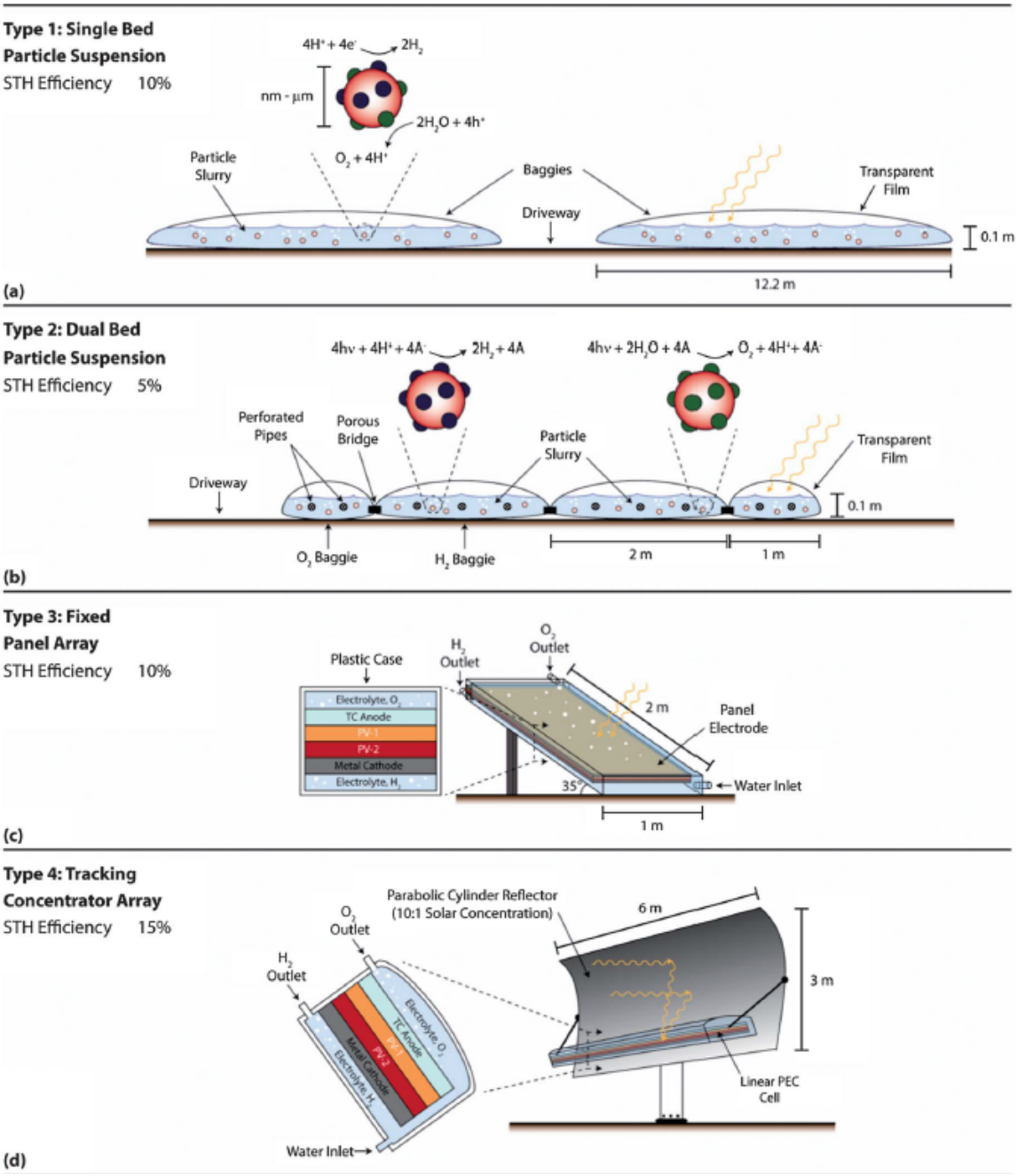

Figure 2.1: Different PEC Reactors Analyzed by Pinaud et al.[46]

2.4 Net Energy Analyses of PECs

To assess the viability of PECs as a source of renewable chemical fuel, several different studies have looked at the energy payback time associated with this technology[24,48,49], and Dumortier and Haussener[48] also analyzed such systems from GHG/kg harvested H_2 standpoint. This section elaborates on the findings in Sathre

et al.[24], wherein a net-energy analysis of a gigawatt-scale, H_2-producing plant was modeled to assess the technology's future viability.

Various metrics exist for quantifying the energy return from energy-producing devices. In such analyses, one quantifies the primary energy inputs and outputs that are needed over the device's lifecycle. The primary energy is the total amount of energy required as inputs before any energy conversion processes are employed to turn a source of free energy as it exists in nature into another form of energy. The primary energy output is, in this case, measured as the Gibb's Free Energy of the produced fuel, though metrics such as the lower heating value can also be used.

Beginning by quantifying the primary energy inputs for an energy-harvesting device, the energy required to produce a device, E_P, is defined as the amount of primary energy inputs required to mine, process and refine all materials into a state ready for manufacturing, transport them to a factory, assemble these materials into a functioning device and ship the device to its intended point of installation. The operational energy input, E_O, is defined as the energy that is expended in order to keep a device operating per unit time, e.g. pumping energy to operate an oil well. The decommissioning energy, E_D, is that required to deconstruct an energy-harvesting device and ship it to a disposal/recycling facility. Combined, these three metrics quantify the overall energy "payment" required to employ an energy harvesting technology. The desired output of such efforts is the harvested energy, E_H, which is the usable energy that can be extracted from an energy-harvesting device, per unit time. This represents the "return" on the energy payment. Having cast the energy flow in the system in economics terms, one can now apply a similar set of simple equations to quantify the performance of an energy-harvesting device so that facile comparisons can be made between various different technologies.

The energy payback time (EPBT), which quantifies how long it takes for an energy technology to recoup the energy payment to operate the device, is quantified as

$$\text{EPBT} = \frac{E_P+E_D}{E_H-E_O}. \tag{2.1}$$

Note that the EPBT only quantifies how long it takes for an implemented technology to become net-energy positive, and does not consider the performance of the device thereafter.

The energy return on energy investment (EROEI) is given as

$$\text{EROEI} = E_H T/(E_O T + E_D + E_P), \tag{2.2}$$

where T is the total lifetime of the device. The net energy balance of a system (EB), defined as the net return on energy payment, is given by

$$\text{EB} = (E_H - E_O)T - (E_D + E_P). \tag{2.3}$$

Clearly, one would like a technology that has the highest EB, EROEI and the

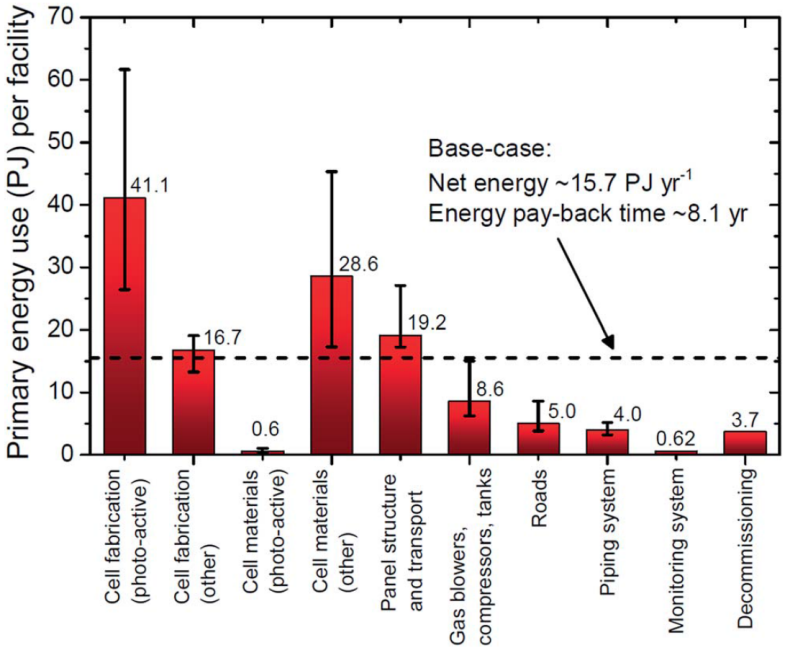

Figure 2.2: Primary Energy Inputs and Decommissioning Energy Required for Base-Case Gigawatt-Scale PEC Plant, in Petajoules[24]

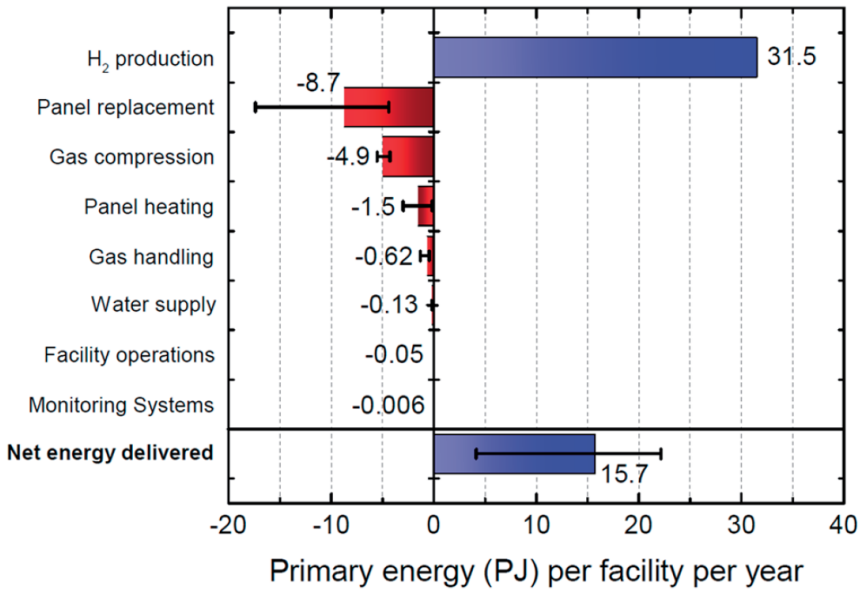

Figure 2.3: Operational Energy and Energy Harvested by Gigawatt-Scale PEC Plant, in Petajoules/Year[24]

smallest EPBT. The highest EROEI seen in nature for a combustible fuel is exhibited by conventional petroleum, as the solar and geothermal energy input required to produce oil is not typically assessed. Globally, the EROEI of oil is approximately 17, though this is falling as more difficult to access oil must be pursued[50]. The EROEI of conventional PV cells ranges, depending on the device architecture and installation location, from roughly 3-10[51]. As mentioned in Chapter 1, sugar cane-derived ethanol has good performance from an energy standpoint relative to other biofuels,

with a estimated EROEI of 3.7[52] for Brazilian ethanol.

As explained in Sathre et al.[24], the EROEI calculated for a base-case, gigawatt-scale PEC system was approximately 1.7. This was for a system with an annual average η_{STH} of 10%, a 10-year panel lifetime (i.e. 10% of panels are replaced per year, on average) and a 40-year facility lifetime. Though the efficiency target seems within reach, the panel lifetime is clearly far beyond what has currently been demonstrated. The values for E_P and E_D are shown in Figure 2.2, and the values for E_O and E_H are shown in Figure 2.3. The largest portion of input energy cost comes from fabricating the photoactive cell, including the PV layers, the protection layers and the catalysts, followed by the other materials such as the case, membrane and panel support structure.

Several things are evident about where one needs to focus research and development efforts to improve the EROEI, EB and EPBT of PECs. One possible avenue of increasing the these three figures of merit is to reduce the amount of photoactive cell per unit production of H_2, e.g. via the use of optical concentration to focus light from a large area onto the PV cell. If this is done, however, the system efficiency must be maintained as high as possible. This is shown in Figures 2.4-2.6, which gives a sensitivity analysis of the EROEI, the EB and the EPBT to the variation of the different model parameters, respectively. In this figure, the panel lifetime is varied from 5-20 years, the annual average η_{STH} is varied from 5-20%, the facility lifetime varied from 20 to 60 years and the cell fabrication energy varied within the error bars shown in Figure 2.3. Other parameter bounds are not given here for brevity.

It is seen that both the panel lifetime and efficiency are the top drivers in determining the overall system performance. Additionally, it can be seen from the analysis that allowing for the system to operate under high pressure is advantageous, as this allows for the removal of some of the gas compression energy necessary to deliver the H_2 to some end use. Finally, the panel-heating requirement, which was defined as the total amount of energy input required to keep the cell temperatures above the freezing point of the electrolyte per year, can play a significant role in reducing the EROEI. Issues pertaining to system temperature are further discussed in Chapters 3, 5 and 6.

2.5 Conclusions

Moving forward, this analysis will attempt to quantify the operation of PECs from a heat transfer, photoelectrochemical efficiency and optical efficiency standpoint. The point of such analyses is to determine what realistic performance could be realized from a PEC that employs optical concentration and is deployed in the working environment.

Clearly, PECs require much technological development before they can become commercially viable. Unless devices are capable of being built that operate at high efficiency for many years, it is difficult to make an energetic case for the viability of PECs as a large-scale source of transportation fuel.

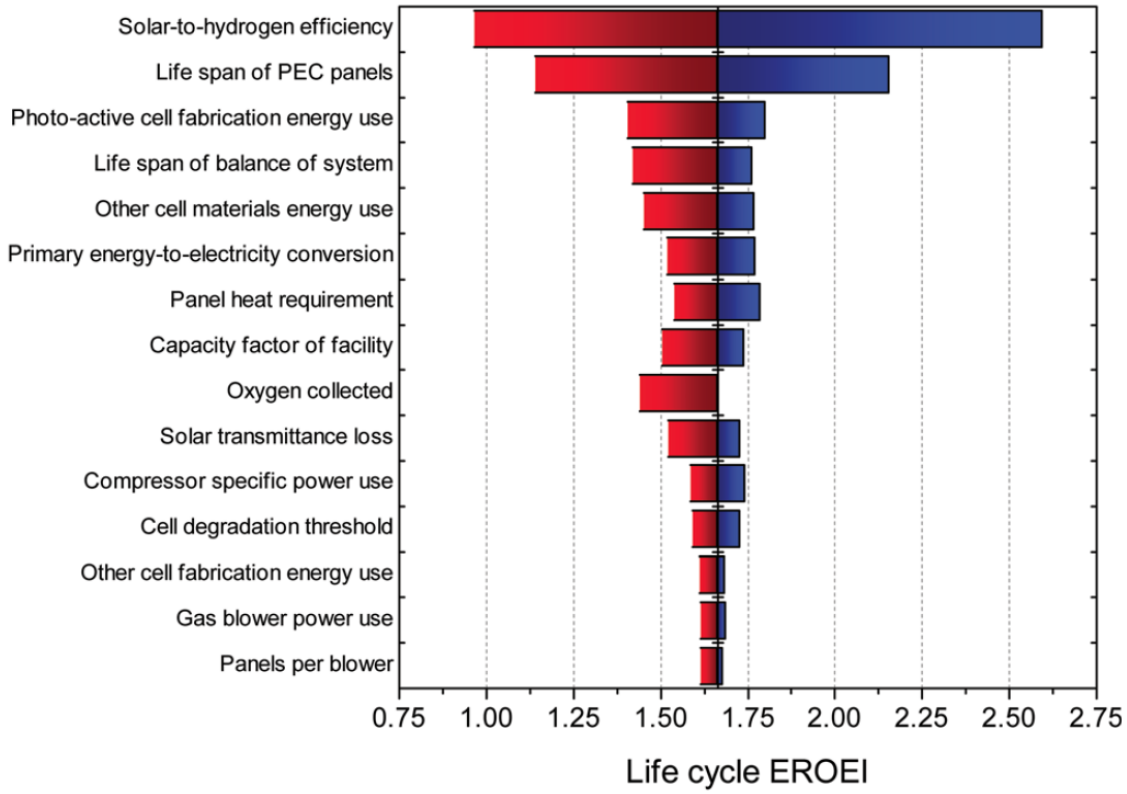

Figure 2.4: Sensitivity Analysis of the EROEI to the Variation of Various Model Parameters[24]

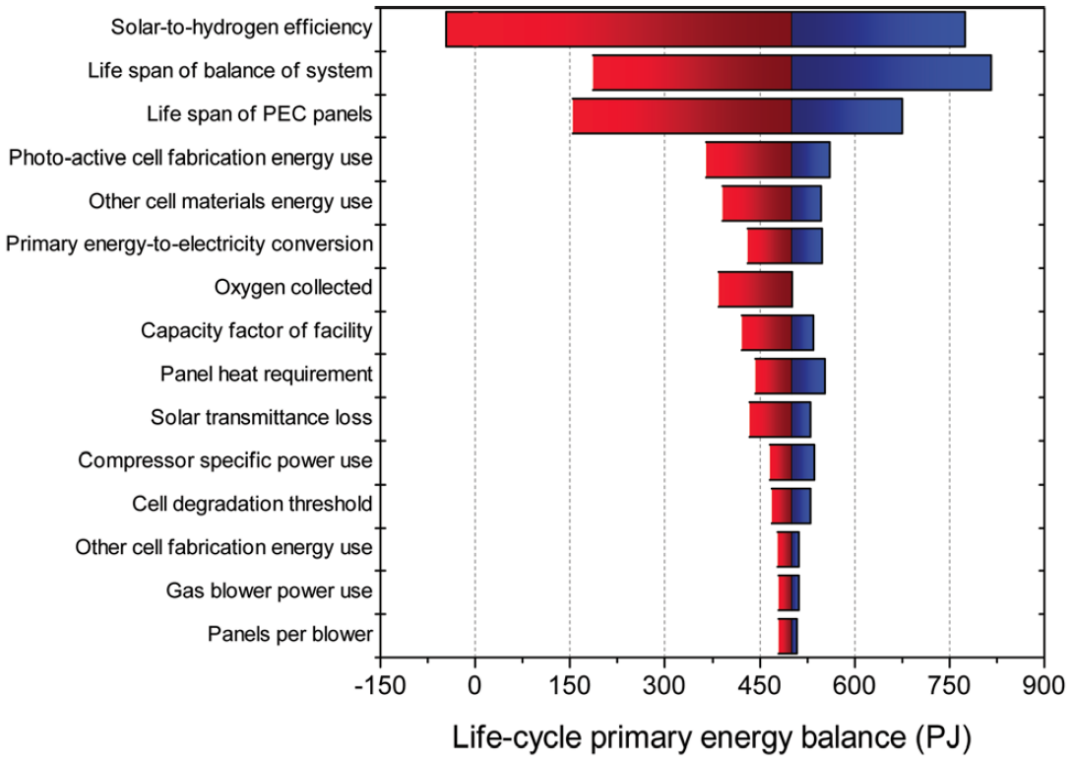

Figure 2.5: Sensitivity Analysis of the EB to the Variation of Various Model Parameters[24]

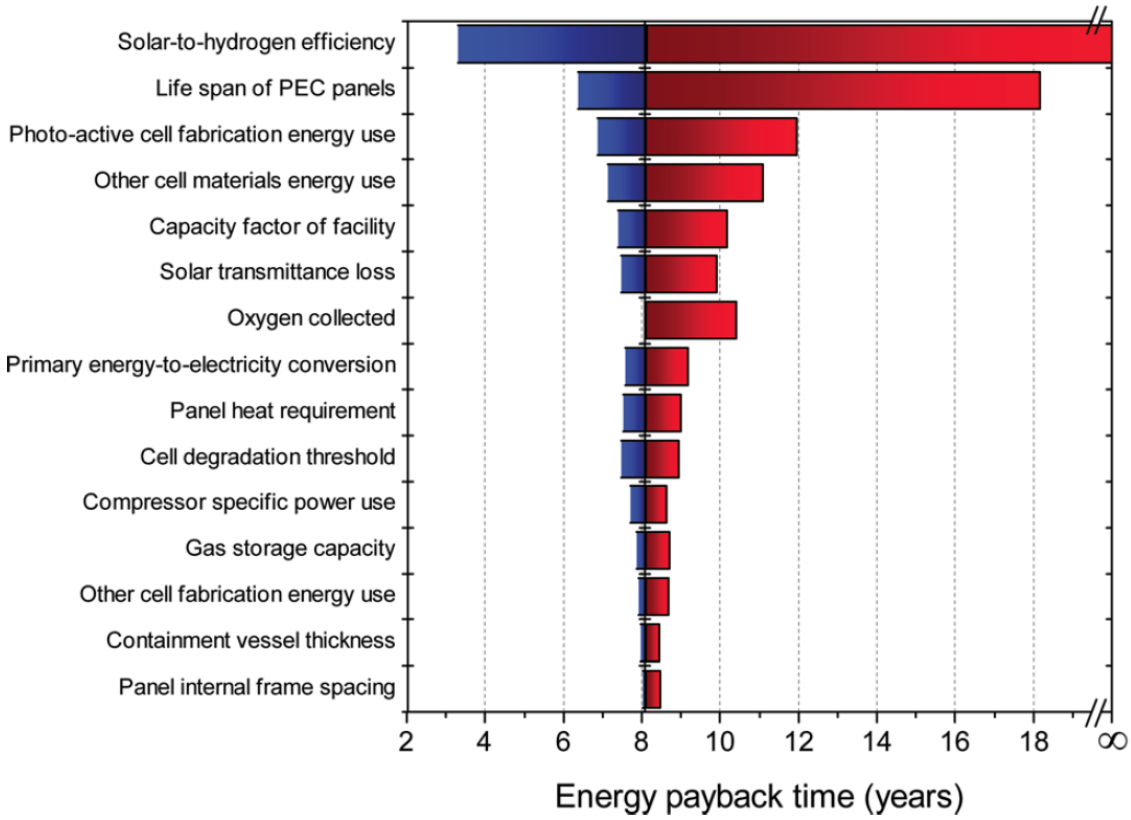

Figure 2.6: Sensitivity Analysis of the EPBT to the Variation of Various Model Parameters[24]

Chapter 3: A Deeper Look at the Temperature-Dependent Physical Phenomena in Photoelectrochemical Cells

3.1 Introduction

In order to build a model that allows for the quantification of PEC performance, we must gain a mathematical understanding of the various physical phenomena that occur within PECs. Additionally, we would like to cast our understanding of these phenomena in terms of their dependence on system temperature.

In this chapter, a review of the literature on the subject of the effects of temperature on photoelectrochemical phenomena within PECs is provided. The review then identifies the pertinent temperature-affected physical processes within a PEC. Following that, a discussion is given of different mathematical and modeling techniques that have been used to capture the behavior of these temperature-dependent processes in purely electrochemical and PV systems. Understanding these two systems, we can then extend our discussion to PECs, and finally lay the framework for Chapter 5, where we delve into more depth about how to construct a heat transfer model of the system.

3.2 Literature Review of Mathematical Models for Modeling PEC Behavior

3.2.1 Overview of Temperature Effects on PECs

Broadly speaking, there are two competing phenomena that occur in PECs that split water to form H_2 and O_2 as cell temperatures vary within a device's operational limits. As temperatures increase, the electrochemical processes involved in water splitting become more facile, but PV cell performance degrades. The increase in temperature causes transport processes in the electrolyte to become faster, the membrane conductivity to increase (if hydration is maintained), and the required electrode potential for water splitting to drop slightly[53]. The former two processes effect a reduced electrical resistance in the electrolyte and membrane, and, combined with the latter process, lead to enhanced electrochemical efficiency because of lower required potential difference between the anode and cathode to drive the water-splitting reaction at a given rate. This can be seen in Equations 3.1 (which was presented previously in Chapter 1) and 3.2,

$$Eff_{Echem} = \mu_{Th,To}/V_{OP} \quad (3.1)$$

$$V_{OP} = j_{Op}A_{El}(R_{Solution} + R_{Membrane)} + \mu_{Th,T} + \eta_{OER}(j_{OP}) + \eta_{HER}(j_{OP}), \quad (3.2)$$

which can be combined as

$$Eff_{Echem} = \mu_{Th,To}/(j_{OP}A_{El}(R_{Solution} + R_{Membrane}) + \mu_{Th,T} + \eta_{OER}(j_{OP}) + \eta_{HER}(j_{OP}). \quad (3.3)$$

As before, Eff_{Echem} is the electrochemical efficiency, $\mu_{Th,To}$ is the thermodynamic potential required for water splitting at 25 °C, i.e. 1.229 V, $\mu_{Th,T}$, is the thermodynamic potential required for water splitting at the cell temperature, V_{OP} is the net applied potential, j_{OP} is the operating current density, $R_{Solution}$ is the total solution resistance, $R_{Membrane}$ is the resistance across the PEM, and η_{HER} and η_{OER} are the overpotentials at cathode and anode, respectively. Although Equations 3.1-3.3, are for simplified, 0-D equivalent-circuits models (see, e.g. Winkler et al.[54]), they allow one to understand the basic relevant trends at a glance.

As PEC temperatures increase, however, the PV cell performance generally degrades, owing to losses in PV cell efficiency. This is caused by a reduction in the bandgap (p. 270, Nelson[55]), and an increase in charge carrier recombination within the cell, which reduce the cell's open circuit voltage and fill factor (FF) (p. 173**,** Nelson[55]). The reduction in bandgap for single-junction devices does, however, typically result in a slightly increased short circuit current density[56]. On the other hand, the short circuit current density often remains roughly constant as temperatures increase for multijunction cells[57]. The end result is a lower maximum PV cell power (and thus efficiency) at a given level of irradiance,

$$P_{Max} = j_{SC} * V_{OC} * FF \quad (3.4)$$
$$Eff_{PV,Max} = j_{SC} * V_{OC} * FF/I_{Sun}, \quad (3.5)$$

where P_{Max}, j_{SC}, V_{OC}, FF, $Eff_{PV,Max}$ and I_o are the maximum power density, the short-circuit current density, the open-circuit voltage, the FF of the cell, the maximum cell efficiency and the incident light intensity, respectively. These points are shown in Figure 3.1**,** which shows a j-V curve for the triple-junction cell discussed shortly.

The net effect of increasing temperatures on overall PEC efficiency is dependent on device geometry and other factors. Generally, PECs that are well designed (i.e. they have small ohmic resistance in the electrolyte and PEM) perform worse as temperatures increase[58], because PV performance degrades more than electrochemical performance improves, and vice versa.

The operation of PECs below 80-100°C is preferable if they utilize Nafion©, as evinced by issues pertaining to the polymer electrolyte membrane's (PEM) stability[59] and species crossover[60] at elevated temperatures. Species crossover can further lead to the formation of explosive mixtures of product gases if the wide flammability window of hydrogen is surpassed; at the very least, crossover leads to reduced device efficiency[61]. If the electrolyte within PECs drops below its freezing temperature (-4.4° C for 1 M H_2SO_4)[62] and solidifies, it may cause the PEC to rupture, or damage other components inside the PEC via the forces exerted by the expanding electrolyte. Even if cell rupture is avoided upon freezing, the formation of

ice prevents transport of water to the oxygen evolution catalyst, thus starving the device of reactants and shutting it down until the electrolyte melts.

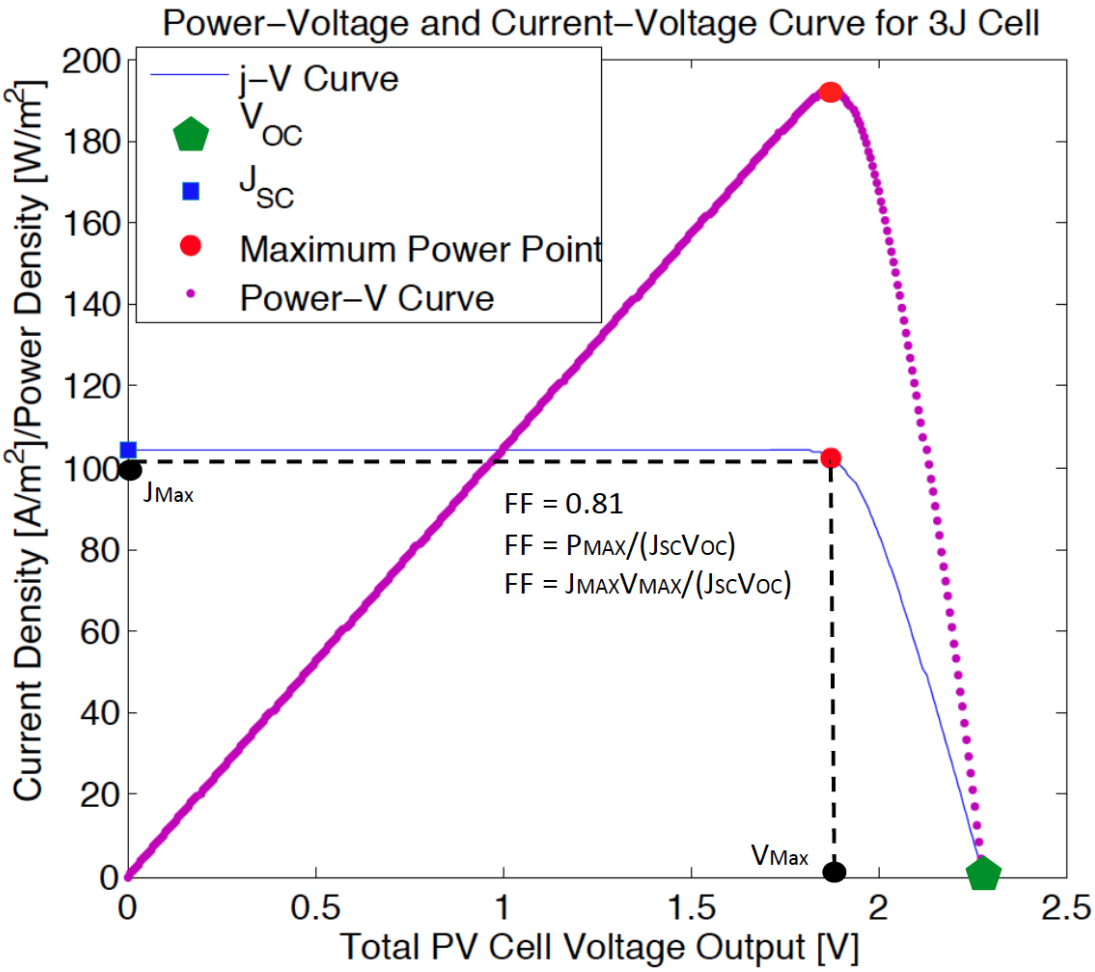

Figure 3.1: Typical j-V Curve of the 3 Junction Cell used in this Work

This description and the subsequent analysis of the effects of temperature on the device implicitly paints a simplified picture of the various chemical reactions in the PEC, assuming that the electrochemical reactions of water splitting to form H_2 and O_2 can be captured using a simple Arrhenius-type model, that no additional electrochemical reactions occur as temperature varies, and that the chemical and mechanical stability of the PEC is not affected by variations in temperatures. This is known to not be true for PECs that reduce CO_2, as Faradaic efficiency is affected by numerous factors[19]. Given the poor lifetime of PECs discussed in Chapter 2, there are clearly additional chemical reactions that occur in all PECs besides water splitting; these lead to the corrosion of the PEC components. Any side reactions besides water splitting will reduce the system's overall η_{STH}. However, this simplified approach is quite useful as a means to understand the thermal and photoelectrochemical performance of a PEC in the field.

3.2.2 Pertinent Mathematical Framework for Modeling PV Systems

Numerous efforts to measure, model and predict the temperature of field-deployed, conventional PV modules and to correlate module temperature to device efficiency have been driven by the interplay between module efficiency and temperature[63–65]. This phenomenon is of particular importance to grid-scale PV module plant installers, as accurately predicting the operating temperature of the modules is critical to estimating the levelized energy cost (LEC) (see, e.g., Norwood and Kammen[66]) produced by a plant, and hence to the plant's economic viability to investors.

There exist many correlations regarding how the efficiency of commercial PV modules decreases with increasing temperature. A review of empirical formulae can be found elsewhere[67]. Generally, temperature correlations of such nature show a linear decrease in module efficiency as temperature rises, having the general form of

$$Eff_{PV,T} = Eff_{PV,To}\big(1 - \beta(T_o - T)\big), \tag{3.6}$$

where $Eff_{PV,T}$ and $Eff_{PV,To}$ are the module efficiencies at a given and reference temperatures, T and T_o, respectively, and β is a module-specific empirical derating coefficient[67]. While Equation 3.6 is useful in predicting module efficiency of commercial, grid-tied PV modules, it does not shed light on how PV cells perform as part of an integrated PEC that does not use power electronics to maintain operation at the maximum power point of the PV cell's j-V curve. As the latter type of device is the central focus of this work, it is necessary to delve deeper into the appropriate modeling equations.

As a starting point to understand the effect of temperature on a PV cell's efficiency, one typically begins with the ideal diode equation. For brevity, a derivation of this is not given here, but a derivation can be found in, e.g., chapter 6 of Nelson[55]. The ideal diode equation gives the value of the operating current density at a given external cell bias (i.e. the voltage difference between the cell terminals) as

$$j\big(V_{Op}, T\big) = j_{SC}(T) - j_o\left(\exp\left(\frac{qV_{Op}}{k_B T}\right) - 1\right), \tag{3.7}$$

where j_O is a material constant resulting from a photovoltaic cell's index of refraction and its band gap[68], q is the elementary charge, T is the temperature in degrees Kelvin and k_B is the Boltzmann constant. The second term in Equation 3.7 is the "dark current", a current that flows opposite to the photon-induced current that provides power to an external circuit. The dark current is caused by recombination of minority charge carriers in the depletion region of the cell. This recombination is driven by the electric field induced by the resistive load through which current generated by the cell flows. At open circuit conditions, the voltage of the cell reaches the thermodynamic limit dictated by the detailed balance[68]; under such conditions, the dark current is equal and opposite to the current induced by the absorption of photons, resulting in no net current flow through the cell's exterior contacts. To

obtain the open-circuit voltage from this equation, we set the left-hand side to zero and solve for V, giving

$$V_{OC}(T) = \frac{k_B T}{q} \ln\left(\frac{j_{SC}(T)}{j_o} + 1\right), \tag{3.8}$$

which indicates that the open-circuit voltage increases logarithmically with the short circuit current density, or, in other words, with the above-bandgap photon flux on the cell. This assertion is not entirely accurate because, for example, the cell temperature tends to increase with concentration ratio. This is discussed in more detail later.

The ideal diode equation is an abstraction of the complex physics that take place inside a semiconductor. Its precision at reproducing the behavior of real systems can be enhanced by accounting for several important parameters that affect real PV cells. While the ideal diode equation does not take the electrical resistance of the cell into effect, this can be remedied by modeling the "series" and "shunt" ohmic resistance in the cell. The series resistance results from the finite resistance in the semiconductor and contacts layers, and causes a voltage drop across the cell as current flows around the circuit to which the cell is attached. The shunt resistance is brought about by the finite resistance between the top and bottom contacts of a cell. Because of this, some of the current generated by the cell can flow directly from the top to bottom contacts, in parallel to that flowing through the external circuit. Ideally, the series resistance would be equal to zero, and the shunt resistance would be equal to infinity. Accounting for these resistances in single-junction devices, we modify the ideal diode equation as,

$$j(V_{OP}, T) = j_{SC}(T) - j_o\left(\exp\left(\frac{q(V_{OP} + j(V_{OP},T)AR_S)}{k_B T}\right) - 1\right) - \frac{V_{Op} + j(V_{OP},T)AR_S}{R_{Sh}}, \tag{3.9}$$

where A is the cross-sectional area of the cell, R_S is the series resistance and R_{Sh} is the shunt resistance. Alternatively, the ideal diode equation can capture more realistic device behavior through the use of a cell bias-dependent "ideality factor," m. This factor typically falls between 1 and 2 (p. 15, Nelson[55]). Using the ideality factor, the ideal diode equation can be written as,

$$j(V_{Op}, T) = j_{SC}(T) - j_o(\exp\left(\frac{qV_{Op}}{mk_B T}\right) - 1). \tag{3.10}$$

Equations 3.9 and 3.10 are often used for creating simple models of PV devices, with parameters that are either measured or used to fit a curve to observed j-V curve data.

The ideal diode equation was derived for a single junction photovoltaic cell. However, if one builds a wireless PEC, the required potential for water splitting at even modest current densities is high enough (~1.7 V at 10 mA/cm^2, [21]) that efficient water splitting cannot be performed using existing single junction devices[42]. Tandem junction or multijunction cells, however, can provide sufficient voltage to perform unassisted, efficient, wireless water splitting[23]. Thus, we would

like to create a model capable of predicting the current-voltage behavior these cells. In multijunction PV cells, detailed modeling of the j-V curve for optically concentrated and unconcentrated PV cell performance is typically based on semi-empirical data[69]. Given that PEC appropriate PV material discovery is a goal of the greater solar fuels community, however, it is preferable to estimate maximum cell performance from first principles, thereby precluding the use of more detailed modeling multijunction cell techniques. Thus, the ideal diode equation incorporating series resistance (Equation 3.9) is the main tool used to model the j-V curve of multijunction cells in this work. Other researchers have employed this same simplified approach[23]. Conversely, complex mathematical models that solve the detailed, coupled semiconductor and electrochemical physics for integrated PECs can be found, e.g. in Berger and Newman[61].

Having settled on using the ideal diode equation, we must now outline a method to determine the temperature-dependent variables used in the equation. Developing a functional relationship between the fundamental properties of a semiconductor (e.g. its bandgap) and its temperature-dependent operational properties (e.g., its j-V curve) can be accomplished with the detailed balance method[68].

To model the multijunction system, we begin by assigning band gaps of the different layers, and choosing indices of refraction that are as close as possible to the chosen materials in the device. Such a multijunction system is depicted in Figure 3.2. We start by recognizing that, in an ideal system, each above-bandgap photon that enters the PV cell creates an exciton, which is then harvested as a free electron and hole (the latter of which constitutes what we denote as the current flow). Thus, if we know the total number of above-bandgap photons incident on a device, we know the maximum (short-circuit) current density possible in the system. This is given by

$$j_{Ph} = q n_{Ph}, \tag{3.11}$$

where j_{Ph} is the current density induced by the photon flux and n_{Ph} is the above-bandgap photon flux. However, even in an idealized system, the semiconductor can spontaneously reemit light that it absorbs. If the angle of incidence of this reemitted light on the interface between the PV cell and the surrounds is within the transmission cone of the material (i.e. it is not totally internally reflected, see Chapter 4), some of the light can leak out of the cell. This negative, radiative current density is given as j_{Rad}. Additionally, some excitons are created by promotion of electrons into the conduction band by thermal effects, which contributes the thermal current density, j_{Th}. Therefore, in total, we have the current density of a PV cell equal to

$$j = j_{Ph} + j_{Th} - j_{Rad}. \tag{3.12}$$

The expression for j_{Th} is

$$j_{Th} = A_{Rad} \exp\left(-\frac{E_g}{k_B T}\right), \tag{3.13}$$

where E_g is the cell bandgap and A_{Rad} is a parameter derived from calculating the escape cone of the semiconductor. It can be shown that this term is negligible for $E_g > 0.3\ eV$[68]. Turning our attention to the current lost to spontaneous reemission,

$$j_{Rad} = A_{Rad} \exp\left(\frac{qV - E_g}{k_B T}\right). \tag{3.14}$$

Combining Equations 3.11, 3.12 and 3.13 and ignoring j_{Th} because most PV devices have $E_g > 0.3\ eV$ gives

$$j = qn_{Ph} + A_{Rad} \exp\left(\frac{qV - E_g}{k_B T}\right). \tag{3.15}$$

Because this analysis ultimately will be using Equation 3.9, it is necessary to have an expression for $V(j)$. So, rearranging,

$$V(j) = \left(\frac{k_B T}{q}\right) \ln\left(\frac{qn_{Ph} - j}{A_{Rad}} + 1\right). \tag{3.16}$$

A_{Rad} is a function of the number of bandgaps in a PV cell. In Singh, Clark and Bell[70], the investigators derived a closed-form solution to the values given in Henry[68]. For the top layer in a multi-junction device, $A_{Rad,1}$ is given as

$$A_{Rad,1} = \frac{q\left(n_{Protection}{}^2 + n_{PV,2}{}^2\right)}{4\pi^2 h_{Bar}{}^3 c^2}\left(q^2 E_{g,1}{}^2 k_B T + 2qE_{g,1}(k_B T)^2 + 2(k_B T)^3\right)\exp\left(-\frac{qE_{g,1}}{k_B T}\right), \tag{3.17}$$

where E_g and n are the band gaps and indices of refraction as indicated in Figure 3.2, h_{Bar} is the reduced Planck's constant, and c is the speed of light in vacuum (see Chapter 4). For the second layer in a 2-junction system,

$$A_{Rad,2} = \frac{q\left(n_{PV,1}{}^2 + n_{Reflector}{}^2\right)}{4\pi^2 h_{Bar}{}^3 c^2}\left(\left(q^2 E_{g,2}{}^2 k_B T + 2qE_{g,2}(k_B T)^2 + 2(k_B T)^3\right)\exp\left(-\frac{qE_{g,2}}{k_B T}\right) - \left(q^2 E_{g,1}{}^2 k_B T + 2qE_{g,1}(k_B T)^2 + 2(k_B T)^3\right)\exp\left(-\frac{qE_{g,1}}{k_B T}\right)\right), \tag{3.18}$$

For a 3-junction system, the first radiative term is identical, but the second and third are slightly different on account of their being another photovoltaic layer beneath the second junction. Thus, one uses,

$$A_{Rad,2} = \frac{q\left(n_{PV,1}{}^2 + n_{PV,3}{}^2\right)}{4\pi^2 h_{Bar}{}^3 c^2}\left(\left(q^2 E_{g,2}{}^2 k_B T + 2qE_{g,2}(k_B T)^2 + 2(k_B T)^3\right)\exp\left(-\frac{qE_{g,2}}{k_B T}\right) - \left(q^2 E_{g,1}{}^2 k_B T + 2qE_{g,1}(k_B T)^2 + 2(k_B T)^3\right)\exp\left(-\frac{qE_{g,1}}{k_B T}\right)\right), \tag{3.19}$$

$$A_{Rad,3} = \frac{q({n_{PV,2}}^2+{n_{Reflector}}^2)}{4\pi^2 {h_{Bar}}^3 c^2}((q^2{E_{g,3}}^2 k_B T + 2qE_{g,3}(k_B T)^2 + 2(k_B T)^3)\exp\left(-\frac{qE_{g,3}}{k_B T}\right) - (q^2{E_{g,2}}^2 k_B T + 2qE_{g,2}(k_B T)^2 + 2(k_B T)^3)\exp\left(-\frac{qE_{g,2}}{k_B T}\right). \quad (3.20)$$

Using these values, one can calculate the voltage output from each layer, given its indices of refraction, the above-bandgap photon flux on the layer and the band gaps of the different layers. The open circuit voltage of the entire cell is then given as

$$V_{OC,Cell} = \sum_{Junc=1}^{\#\ Junctions} V_{OC,Junction}, \quad (3.21)$$

where $V_{OC,Junction}$ equals the open circuit voltage for the junction within the PV cell, and is given by Equation 3.16 when *j*=0. The short circuit current density of the entire cell is given by the minimum current density in each of the layers, or

$$j_{SC,Cell} = Min(qn_{Ph,Junc}). \quad (3.22)$$

Equation 3.22 is of particular use in Chapter 4, where the fact that the limiting junction's current density is the current density of the entire cell is put to use when designing the optical system that concentrates sunlight on the PV cell in the PEC. Using these values, one can then employ Equation 3.9 to construct a j-V curve with the desired FF.

As mentioned, the FF, $j_{SC,Cell}$ and $V_{OC,Cell}$ are temperature dependent, and so one uses values for typical cells as a function of temperature to determine these to serve as a reasonable guess in the absence of a simple analytical relation. This follows the general methodology laid out in Haussener et al.[53], though some treatment of optical concentration is different.

In order to model the temperature-dependent effects in 3-junction PV cells, the model uses values from Nishioka et al.[57] to adjust FF, $j_{SC,Cell}$ and $V_{OC,Cell}$. These data are for InGaP/InGaAs/Ge Spectrolabs© cells, as a function of concentration ratio and temperature. For the 2-junction PV cells modeled, the model uses the methodologies laid out elsewhere[71] to estimate FF, $j_{SC,Cell}$ and $V_{OC,Cell}$ for Si and GaAs cells. These values are listed in the supporting information in Haussener et al.[53].

In order to calculate the fill factor for 3-junction cells, the model employs the following set of equations:

$$V_{OC,Cell}(T, CR) = V_{OC,Cell}(T_0, CR)\frac{dV_{OC}(CR)}{dT}(T - 298.15) + V_{OC,Cell}(T_0, CR) \quad (3.23)$$

$$FF(T, CR) = FF(T_0, CR)\frac{dFF(CR)}{dT}(T - 298.15) + FF(T_0, CR) \quad (3.24)$$

$$j_{SC,Cell}(T, CR) = j_{SC,Cell}(T_0, CR)\frac{dj_{SC}(CR)}{dT}(T - 298.15) + j_{SC,Cell}(T_0, CR), \quad (3.25)$$

where CR is the concentration ratio of the cell, T_0 is 298.15 K, T is the actual PV temperature, and the values of $\frac{dFF(CR)}{dT}$, $\frac{dJ_{SC}(CR)}{dT}$ and $\frac{dV_{OC}(CR)}{dT}$ are the derate factors for the fill factor, short circuit current density and open circuit voltage with respect to temperature, respectively (interpolated between CR values of 1 and 17 as listed in Nishioka et al.[57]). The FF is derived from Nishioka et al.[57], whereas $j_{SC,Cell}$ and $V_{OC,Cell}$ are calculated using the detailed balance methodology.

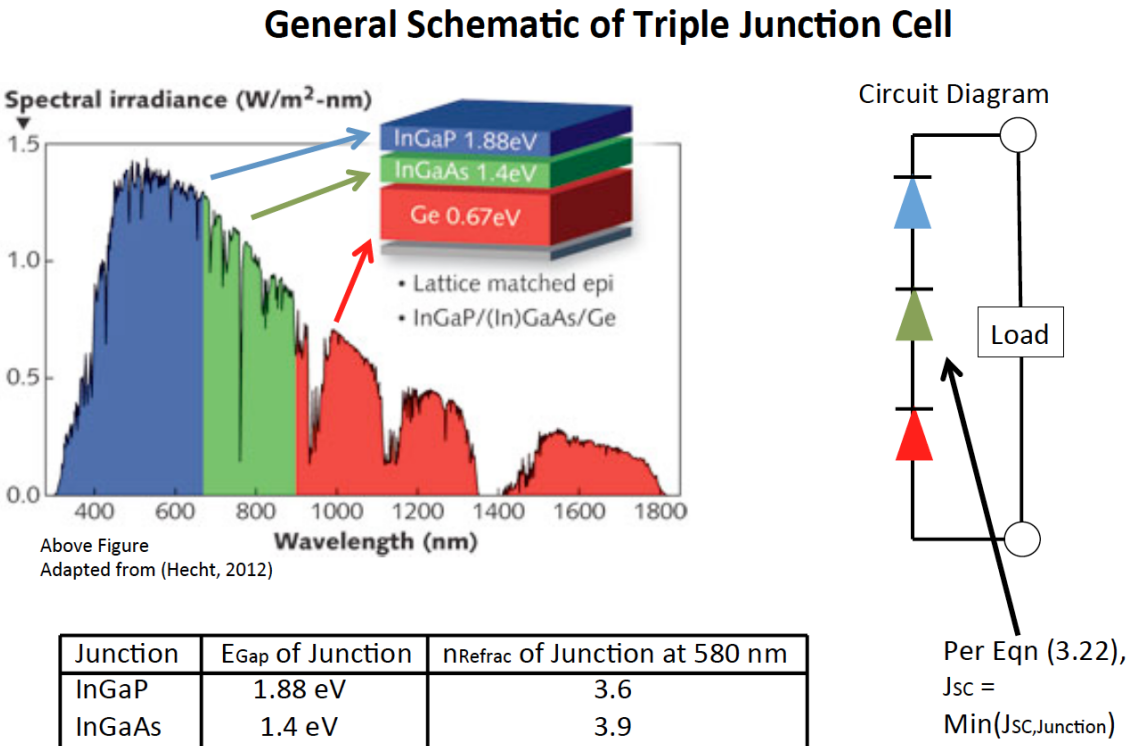

Junction	E_{Gap} of Junction	n_{Refrac} of Junction at 580 nm
InGaP	1.88 eV	3.6
InGaAs	1.4 eV	3.9
Ge	0.67 eV	5.6

Figure 3.2: Depiction of 3 Junction Cell Modeled Herein

In the case of the 2-junction device, the model derates the $V_{OC,Cell}$ and $J_{SC,Cell}$ by determining how the values of $E_g(T)$ for the cell materials change with temperature,

$$E_{g,1}(T) = E_{g,1}(T_0) - \frac{\alpha_{GaAs}T^2}{T+\beta_{GaAs}} \tag{3.26}$$

$$E_{g,2}(T) = E_{g,2}(T_0) - \frac{\alpha_{c-Si}T^2}{T+\beta_{c-Si}} \tag{3.27}$$

where α_{GaAs}, β_{GaAs}, α_{c-Si} and β_{c-Si} are sourced from [71], and the values of temperature follow the convention laid out for the 3-junction cell. These values are then fed into the detailed-balance equations (3.15-3.22) to generate $V_{OC,Cell}(T)$ and $j_{SC,Cell}(T)$. To calculate the change in FF as a function of temperature, the model employs the following relation[71,72],

$$FF(T,CR) = \left(\frac{qV_{OC,Cell}}{k_B T} - \ln\left(\frac{qV_{OC,Cell}}{k_B T} + 0.72\right)\right) / \left(\frac{qV_{OC,Cell}}{k_B T} + 1\right) \quad (3.28)$$

Different j-V curves for the triple junction cell at different temperatures are displayed in Figure 3.3. The takeaway from this analysis is that solar cell performance (as measured by its peak efficiency and voltage output) declines as temperature increases.

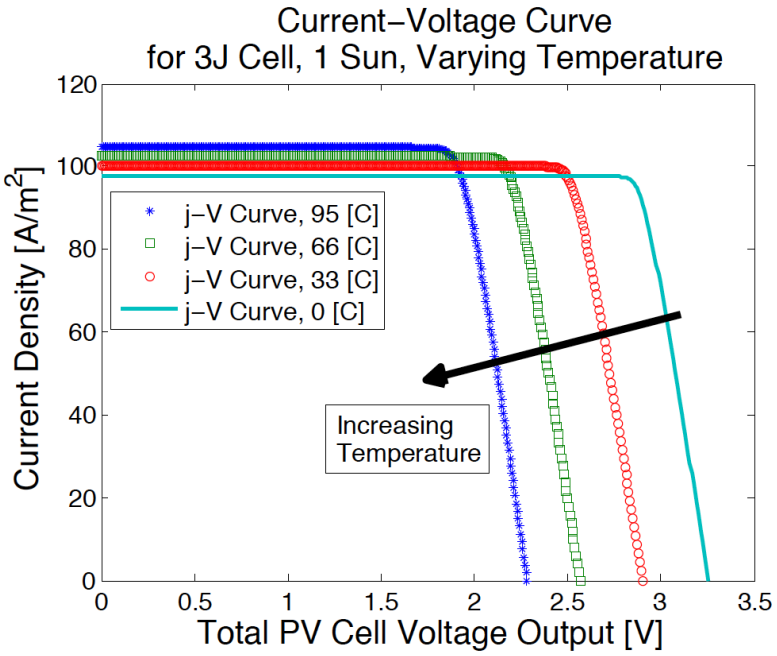

Figure 3.3: Effect of Temperature on Triple Junction Cell Modeled in this Work

3.2.3 Pertinent Mathematical Framework for Modeling Electrochemical Systems

In order to model the j-V behavior of the electrochemical reaction, one can use assorted semi-empirical equations. Though this section covers the relevant phenomena for this modeling effort, the reader is encouraged to read chapters 1 and 3 of Bard and Faulkner[20] for a more in-depth understanding of transport phenomena and electrode kinetics, respectively.

There are four primary factors affecting the j-V curve of the electrochemical cell in a PEC. These are 1) the electrode kinetics, 2) the transport kinetics in the electrolyte 3) the transport kinetics in the membrane and 4) the equilibrium potential of the chemical reaction at hand (in this case, water splitting). The goal of understanding these phenomena is to calculate the total voltage that must be applied to the system to elicit a certain current density, as shown in Equation 3.2. This equation is graphically represented in Figure 3.4, which combines electrochemical and PV physics models.

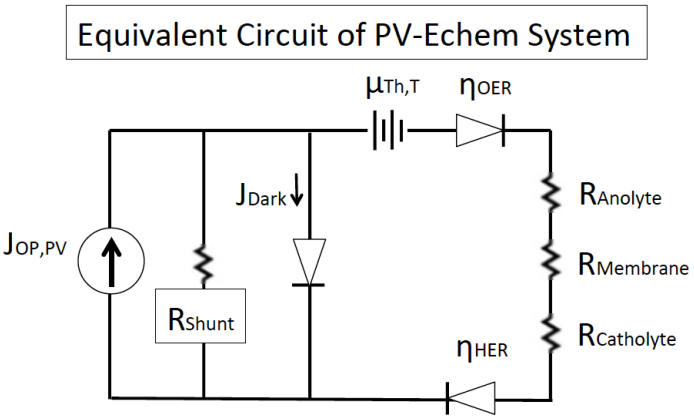

Figure 3.4: Equivalent Circuit of Modeled PEC

Beginning with the electrode kinetics, a typical electrochemical system is depicted in Figure 3.5. As introduced in Chapter 1, at the anode, chemical species are oxidized (electrons are transferred to the electrode from the chemical species), and at the cathode, chemical species are reduced (electrons are transferred from the electrode to the chemical species). The force causing this transfer of charge is the potential of the electrodes, which must be changed from the equilibrium potential dictated by the electrochemical system. The overpotential, η, at an electrode

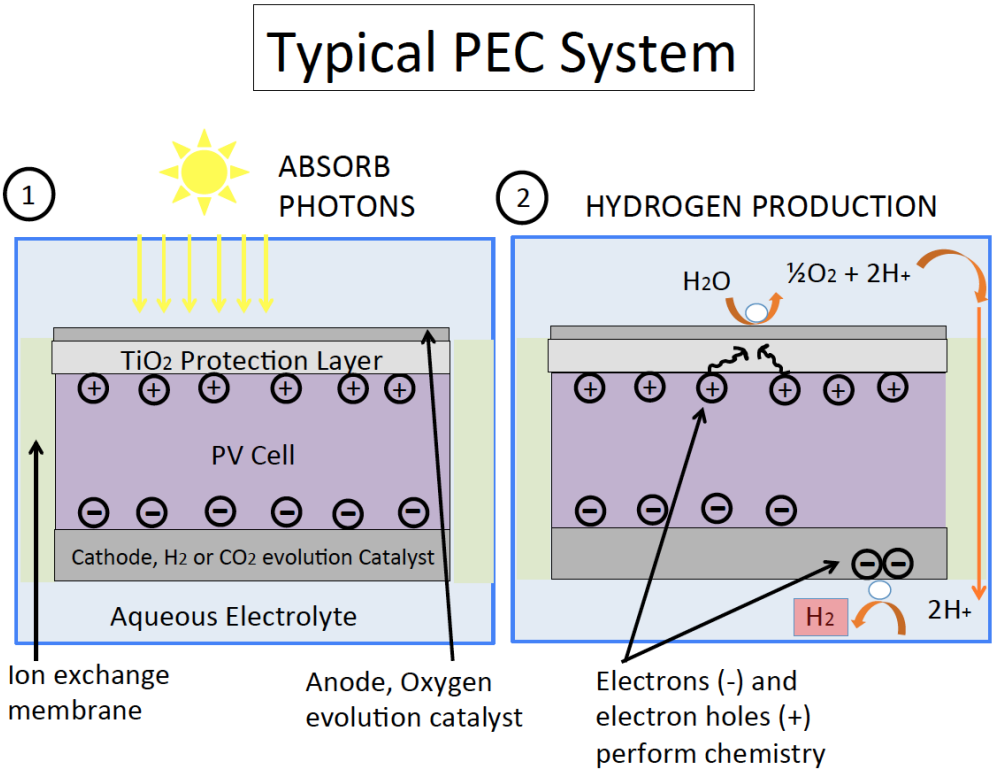

Figure 3.5: Typical Wireless PEC Modeled in this Work

quantifies the difference in potential between the equilibrium and actual values at the electrode. In order to relate η to the current density at the anode or cathode of a

water-splitting system, ($j_{OER/HER}$, respectively, where OER stands for the oxygen evolution reaction and HER stands for the hydrogen evolution reaction), the model uses the Butler-Volmer equation. This equation allows the model to fit the experimentally-observed behavior of an electrochemical system, so as to relate the applied electrode potential to the observed current density. The equation is given as

$$j_{OER/HER} = j_{O,OER/HER} * (\exp\left(\frac{\alpha_{a,OER/HER} F \eta_{OER/HER}}{RT}\right) - \exp\left(\frac{\alpha_{c,OER/HER} F \eta_{OER/HER}}{RT}\right)), \quad (3.29)$$

where $j_{O,OER/HER}$ is the OER or HER exchange current density, $\alpha_{a,OER/HER}$ is the OER or HER anodic transfer coefficient, $\alpha_{c,OER/HER}$ is the OER or HER cathodic transfer coefficient, F is Faraday's constant (96,485 C/mol), R is the universal gas constant, and T is the catalyst temperature in Kelvin. These parameters are given below. The exchange current density is a measure of the derivative of the overall current density as a function of the electrode potential, with larger values corresponding to greater current densities at a given electrode overpotential. In other words, better catalysts have a better exchange current density. The cathodic transfer coefficient is a measure of how the oxidation and reduction reactions proceed at a given potential, near the equilibrium potential. A higher value of $\alpha_{c,HER}$ and $\alpha_{a,OER}$ elicit better catalytic performance for a water-splitting system. The values of the transfer coefficients and exchange current densities are derived from experimental measurements.

While the Butler-Volmer equation is useful for predicting behavior of well-stirred reactors or reactions operating at low current densities, eventually an electrochemical system will achieve a state known as the "diffusion limited regime", wherein the transport of reactants to the electrodes from the bulk solution is not fast enough to keep up with the rate of reaction at the electrode surface. This behavior can be modeled by introducing extra terms into the Butler-Volmer equation, which gives the Current-Overpotential Equation,

$$j_{OER/HER} = j_{O,OER/HER} * ((\frac{\mathrm{C_O}(0,\mathrm{t})}{\mathrm{C_O^*}})\exp\left(\frac{\alpha_{a,OER/HER} F \eta_{OER/HER}}{RT}\right) - (\frac{\mathrm{C_R}(0,\mathrm{t})}{\mathrm{C_R^*}})\exp\left(\frac{\alpha_{c,OER/HER} F \eta_{OER/HER}}{RT}\right)), \quad (3.30)$$

where $((\mathrm{C_O}(0,\mathrm{t}))/(\mathrm{C_o^*}))$ is the ratio of the oxidized species at the electrode to the bulk concentration as a function of time, and $((\mathrm{C_R}(0,\mathrm{t}))/(\mathrm{C_R^*}))$ is the ratio of the reduced species at the electrode to the bulk concentration, as a function of time. This analysis will leave such further discussions aside for now, and proceed with the Butler-Volmer equation.

Progressing now to transport in the electrolyte, the model needs a means to calculate the 0-D resistance in the solution. One way to do this is to use the Nernst-Planck equation, which is given as, for one-dimensional systems,

$$F_i(x) = -D_i \frac{\partial C_i(x)}{\partial x} - \frac{z_i F}{RT} D_i C_i \frac{\partial \phi(x)}{\partial x} + C_i v(x), \quad (3.31)$$

where $F_i(x)$ is the flux $\left(\frac{mol}{cm^2 s}\right)$ of species *i*, D_i is the diffusivity of species *i*, C_i is the concentration of species *i*, $\phi(x)$ is the potential and $v(x)$ is the velocity of a volume element of solution. The terms in the equation account for the transport of species via diffusion, migration (the movement of charged species under an electrical field), and via convection, respectively. While this is the approach taken by numerous investigators in the field[35,58], solving this equation is computationally expensive, and thus it would be optimal have a simpler expression that exchanges some accuracy for computational speed. The reason for needing such speed is due to the desire to simulate the hourly operation of these devices over a typical year. Therefore, the model cannot solve the more accurate transport equations or the simulations will be too computationally expensive. The simpler equation employed to model the effect of kinetics in the electrolyte was derived in Singh, Stevens and Weber[21]. Though the equation was derived for a PEM, the equation can be extended to electrolyte if one assumes that it can be treated with average effective properties. The equation is given as

$$P = \frac{\alpha_{Geom}}{\frac{\beta_{Geom}{}^2}{2} + \frac{\beta_{Geom}}{\gamma_0 \tanh(\gamma_0(1-\beta_{Geom}))} + 2\sum_{n=1}^{\infty}\left(\frac{1}{\zeta_n{}^2} - \frac{\gamma_n \tanh(\gamma_n(1-\beta_{Geom}))}{\zeta_n{}^3 \sinh(\zeta_n \beta)\left(1 + \frac{\gamma_n \tanh(\gamma_n(1-\beta_{Geom}))}{\zeta_n \tanh(\zeta_n \beta_{Geom})}\right)}\right)}, \quad (3.32)$$

where, using values of system height and length shown in Figure 3.6, α is calculated as

$$\alpha_{Geom} = h_d/l_d - \beta_{Geom} h_a/l_a, \quad (3.33)$$

with $\beta_{Geom} = l_a/l_d$, the term $\gamma_n = (n + 0.5)\pi l_d/h_d$, the term $\zeta_n = n\pi/\alpha$, and P calculated as

$$P = \frac{j_{OER/HER} l_d}{K_{Electrolyte} \mu_{Anolyte/Catholyte}}, \quad (3.34)$$

where $K_{Electrolyte}$ is the electrolyte conductivity. Using Equations 3.32, 3.33 and 3.34, the equation for P is rearranged to solve for $\mu_{Anolyte/Catholyte}$. This methodology treats the voltage loss from the system by considering potential drop from the center point of the PV cell to the isopotential membrane, as depicted in Figure 3.6. This is conservative in its estimation of the total system losses at a given current density, as ions originating from the point, $(0, h_a)$ must travel the longest distance in the solution and undergo the greatest ohmic drop.

Turning to the potential losses in the membrane, and assuming a uniform current density in the membrane, the potential drop in the membrane, $\mu_{Membrane}$ is calculated as

$$\mu_{Membrane} = \frac{j_{OER/HER} l_a}{l_d - l_a} * h_m / K_{Membrane}, \tag{3.35}$$

where h_m is the height of the membrane and $K_{Membrane}$ is the membrane conductivity. This is derived from Ohm's law.

Finally, the derivation of $\mu_{Th,To}$ is given in Chapter 1. Thus, the model has accounted for all the terms in Equation 3.2, but now needs to account for variation of the properties of the electrochemical system as a function of temperature.

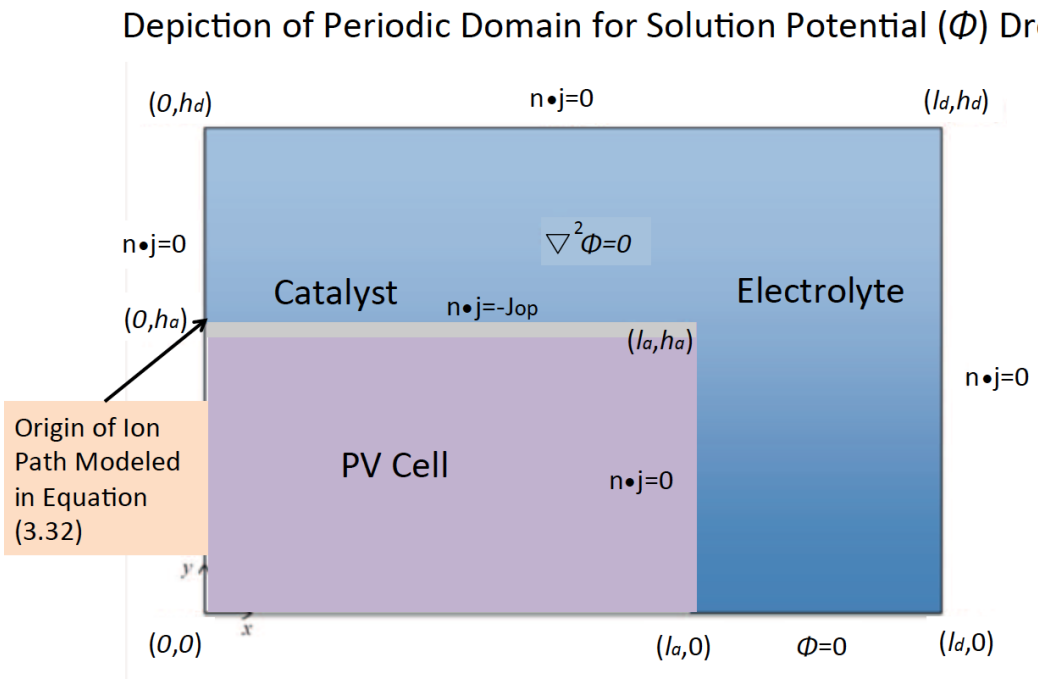

Figure 3.6: Domain Modeled in Equation 3.32

Turning to the work of Chen, et al.[73] allows the model to account for the variation of $K_{Membrane}$, $K_{Electrolyte}$, $\mu_{Th,T}$ and $j_{O,OER/HER}$. In all of the given expressions, T_0=300 K. The variation of $K_{Membrane}$ for Nafion is given by the equation,

$$K_{Membrane}(T) = K_{Membrane}(T_0)\exp\left(\frac{E_{a,Membrane}}{RT_0} - \frac{E_{a,Membrane}}{RT}\right), \tag{3.36}$$

where $K_{Membrane}(T_0)$=10 m/S and $E_{a,Membrane}$=2000, and is chosen to fit empirical data. While the PEC community ultimately would like to use a different PEM than Nafion, the material properties of Nafion are known and thus are used in this analysis[61]. The variation of $K_{Electrolyte}$ (in m/S) with temperature is given as

$$K_{Electrolyte}(T) = 40(1 + \tau_{Electrolyte}(T_{Electrolyte} - T_0), \quad (3.37)$$

where $\tau_{Electrolyte}$ is 0.019.

The variation of $\mu_{Th,T}$ is given as,

$$\mu_{Th,T} = \mu_{Th,To} + (T - T_0)/1000. \quad (3.38)$$

The variation of the exchange current densities with temperature is modeled as

$$j_{O,OER}(T) = j_{O,OER}(T_0)\exp\left(\frac{E_{a,OER}}{RT_0} - \frac{E_{a,OER}}{RT}\right) \quad (3.39)$$

and

$$j_{O,HER}(T) = j_{O,HER}(T_0)\exp\left(\frac{E_{a,HER}}{RT_0} - \frac{E_{a,HER}}{RT}\right) \quad (3.40)$$

where $j_{O,HER}(T_0) = 10\ (A/m^2)$m $j_{O,OER}(T_0) = 1.4\ (mA/m^2)$, $E_{a,HER}$=28,900 and $E_{a,OER} = 42{,}560$.

Typical j-V curves for the electrolyte as a function of system temperature are given in Figure 3.7. The general trend is that the transport processes become easier as the temperature of the system increases.

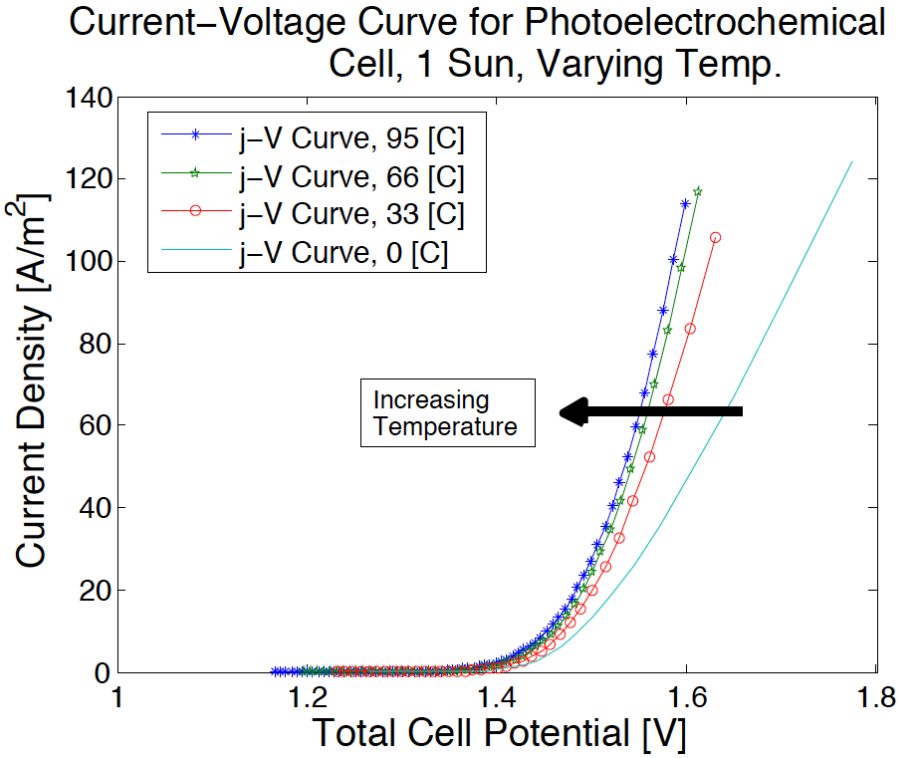

Figure 3.7: Positive Effect of Increasing Temperature on Electrochemical Behavior

3.3 Sample Outputs for Photoelectrochemical Model

Now that the model can predict both the electrochemical and photovoltaic systems in the PEC, it can calculate the operational current density for a given set of system dimensions, materials and temperatures. The actual operation point of the cell is, in this equivalent circuits analysis, given by the intersection of the j-V curves of the PV and electrochemical cells.

The point of this section of the manuscript is to show a sensitivity analysis of the PEC's η_{STH} to four different parameters: the concentration ratio, the temperature, the PEC cell dimensions and the membrane width. These four scenarios are illustrated in Figures 3.8 a)-d), respectively. Figure 3.9 gives a depiction of the modeled systems used to generate Figures 3.8 a)-d). Two different PEC cell sizes were used to generate Figure 3.8) c). These were a "small" PEC (3.9 a)) and a "large" PEC (3.9 b)). The simulations used to generate Figures 3.8) a) and d) were modeled using the "small" PEC. The simulations used to generate Figure 3.8) b) used the "large" PEC.

As shown in Figure 3.8 a), for triple-junction systems, one can afford to raise the concentration ratio significantly before moving out of operation on the "plateau" of the j-V curve of the PV cell, where $j_{OP} \approx j_{SC}$. One wishes to operate the cell in this region of high current density because the total output of fuel results from the system's current density. A triple-junction cell sacrifices J_{SC} relative to an optimally-designed 2-junction cell[23] and thus has a lower total attainable efficiency for wireless systems. On the other hand, because triple junction systems have more voltage that can be expended on the potential losses in the solution, membrane and catalysts, triple junction systems have the potential to operate with higher concentration ratios (whereby we can increase J_{SC} through higher photon flux)**.** Eventually, however, the system will move beyond the regime where it operates close to J_{SC} as the ohmic losses and overpotentials mount, as shown for the case where the concentration ratio equals 15.

In Figure 3.8 b), the effect of temperature on a "poorly" designed PEC is shown. The cell considered herein is 1 cm wide, and, as such, suffers considerable ohmic losses in the solution relative to a design with smaller internal dimensions. Thus, for very low temperatures, the decrease in solution conductivity outweighs the gain in the PV cell efficiency. This shows similar results to Chen et al[73].

Figure 3.8 c) shows a similar trend to Figure 3.8 b), in that the effect of the ohmic drop resulting from large cell sizes is demonstrated. Additionally, for the system, going to progressively smaller cell sizes for a given J_{SC} (in this case, for the triple junction system operating under 10 suns of illuminance with the AM 1.5 D spectrum) would have little benefit, as it would still be operating on the plateau of the j-V curve.

Figure 3.8 d) shows how the system behaves as the percent of the PEC's width taken up by the membrane is varied from 2.5%-7.5%. The point of varying this is to show how wide the membrane must be in order to not incur large voltage losses in the system. From an optical design standpoint, one would like to minimize the width of this membrane. This is because light that is incident on the membrane

Varying Different Design and Operational Parameters of the Photoelectrochemical Cell

3.8 a)

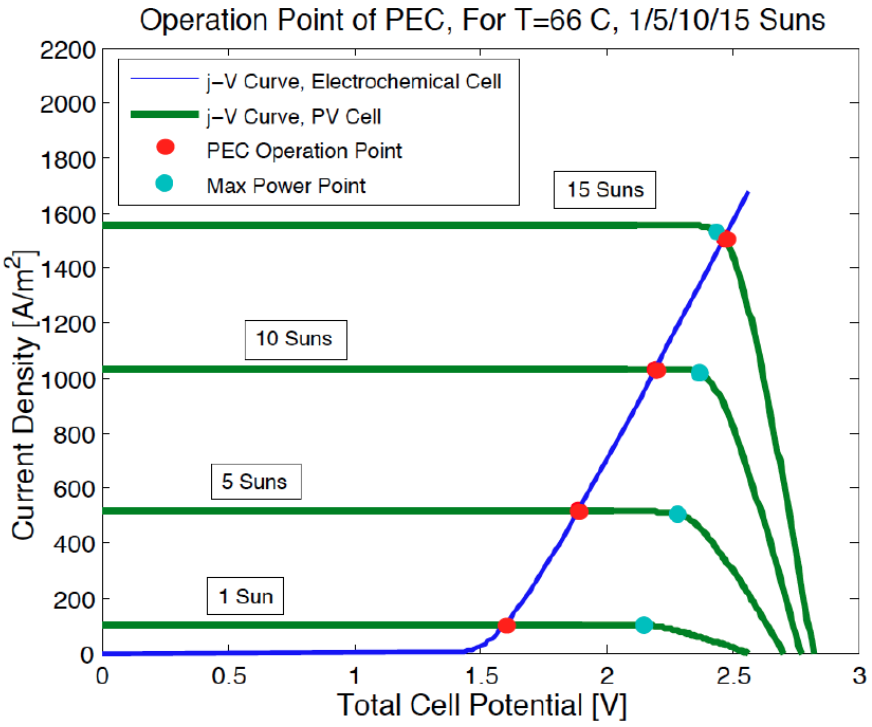

3.8 b)

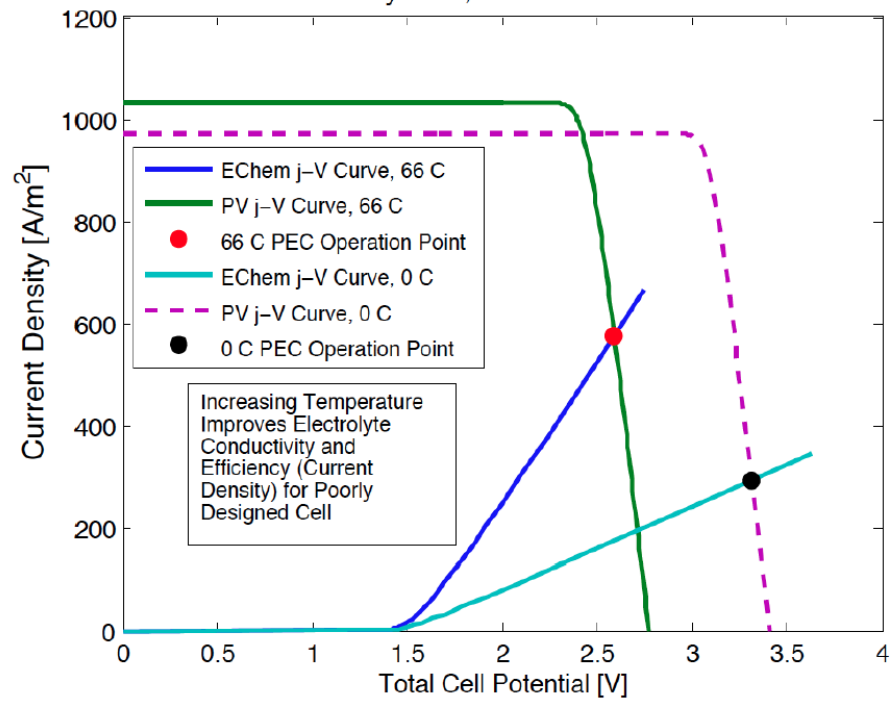

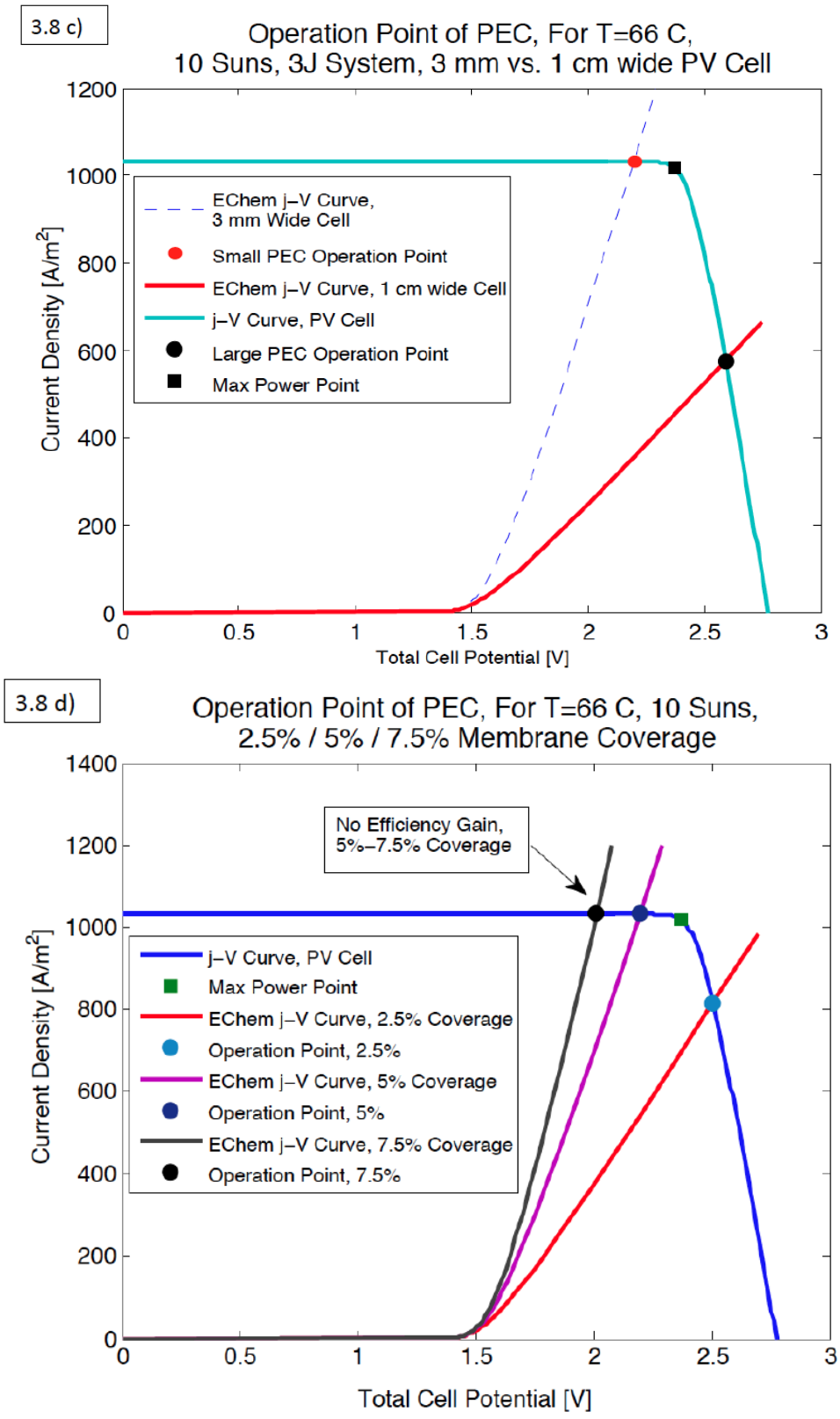

Figures 3.8 a)-d): Effects of Varying Design and Operational Parameters for PEC System

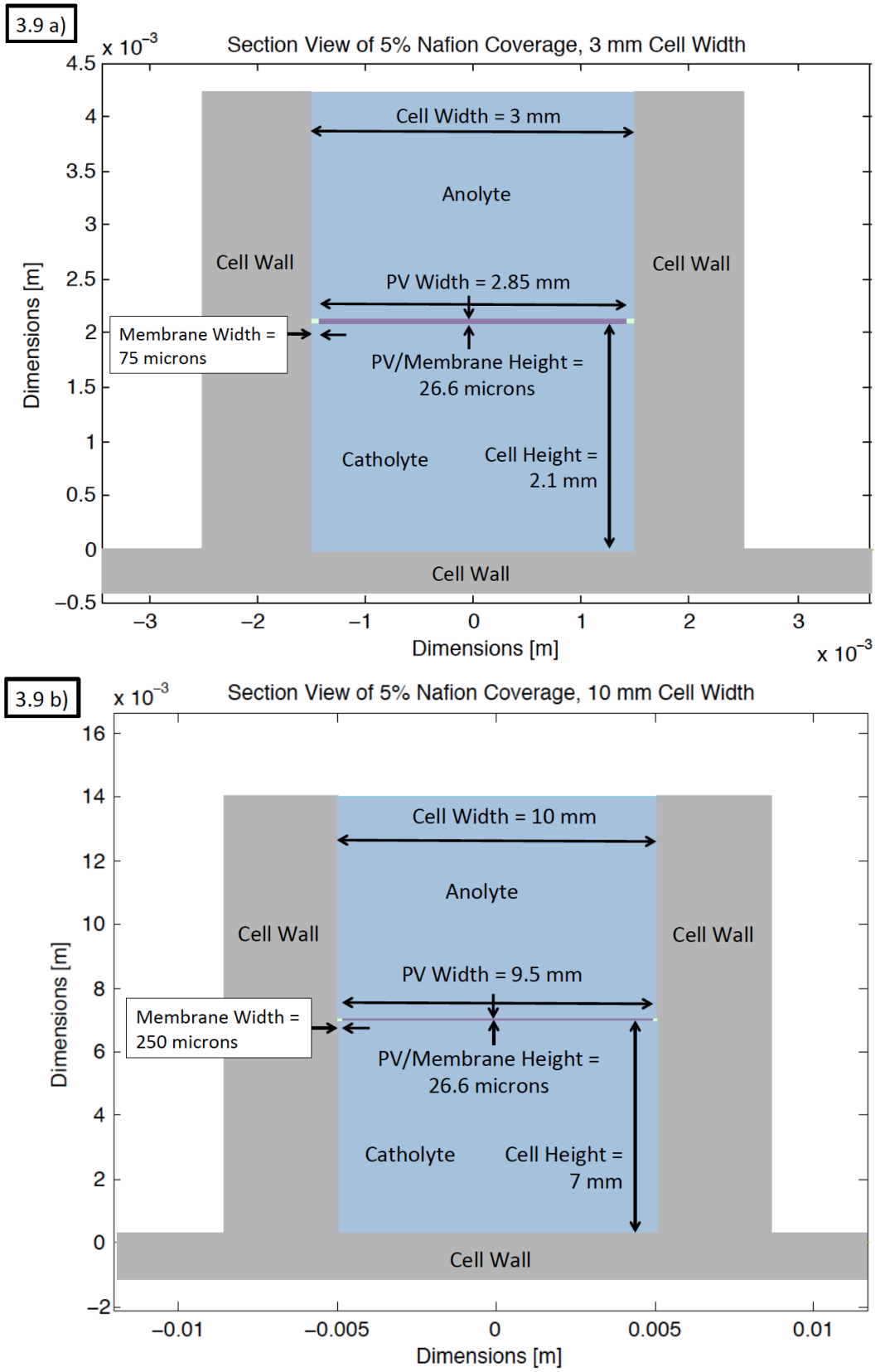

Figure 3.9: Depiction of General Domain Simulated to Produce Figure 3.8 a)-d)

is lost to optical absorption, and the wider the membrane, the greater the portion of light flux will be lost. As the membrane width becomes very small, however the ohmic transport losses increase because a greater current density is forced through the membrane of set resistivity. This can be seen in Equation 3.35. There is, however, a point after which further increases in the membrane width do not deliver appreciably higher J_{OP} because the system is again operating on the plateau of the j-V curve. Thus there is a limit to the desired width of the membrane for a given PV cell, the overall cell dimensions and the concentration ratio. This is also supported by the results from other investigators[73].

3.4 Conclusions

Having outlined the temperature dependent photoelectrochemical phenomena in more detail, one can now describe the physics dictating the behavior of the optical system and the PEC's heat transfer with the surrounds. With these, the foundation of the computational model will be complete in order to allow one to predict the PEC's operating temperatures and fuel production efficiency.

Chapter 4: Methods for Optically Modeling an Integrated, Optically Concentrating Photoelectrochemical Cell

4.1 Introduction

The simulation of the propagation of light through the PEC system is required to determine the overall fuel yield from a PEC deployed at a certain location. This is because the throughput efficiency of photons from the atmosphere, through the PEC system, to the PV cell in the PEC is what determines the maximum possible rate of fuel generation.

Different methods for simulating light's propagation in these systems are discussed in Sections 4.2-4.6. These are provided as a background for the interested reader, but are not necessary to understand the author's work. The primary difference in methods is their mathematical treatment of light, and the length scales at which their use is valid. This analysis will touch on physical optics, and then give a much more in-depth look at how to model the optically concentrating PEC using geometric optics and thin-film optics. Then, some salient considerations pertaining to lens design are discussed.

The methodology for combining these elements into one computational scheme that allows for the modeling of the propagation of light through the PEC is given, starting in Section 4.7. Then, finally, some initial testing of the photon throughput efficiency for different lens/PEC designs allows for the down-selection of possible PEC configurations. This scheme sets the stage for modeling the entire system from a heat- and light-transfer, and fuel production standpoint in Chapter 6.

4.2 Physical Optics and Maxwell's Equations

Physical optics treats light as a wave, and is applicable for reflecting media of all size regimes. The primary advantage of solving Maxwell's equations is that the solutions they provide are highly accurate, even in complex, microscale and nanoscale systems. The disadvantage is that the solution of these equations is not trivial, and becomes computationally demanding for any large-scale, high frequency system.

Physical optics solves for the amount of energy through a domain containing varied media using Maxwell's equations, which can be written as, for continuous media,

$$\nabla\times\mathbf{E}+\frac{1}{\mathrm{c}}\frac{\partial\mathbf{B}}{\partial\mathrm{t}}=0 \tag{4.1}$$

$$\nabla\times\mathbf{H}-\frac{1}{\mathrm{c}}\frac{\partial\mathbf{D}}{\partial\mathrm{t}}=\frac{4\pi}{c}\boldsymbol{j} \tag{4.2}$$

$$\nabla \cdot \mathbf{D} = 4\pi\rho \tag{4.3}$$

$$\nabla \cdot \mathbf{B} = 0. \tag{4.4}$$

In this system of equations, **E** is the electric field, **H** is the magnetic field, **B** is the magnetic field flux, **D** is the electric field flux, ρ is the charge density, c is the speed of light in vacuum (299,792,456.2 ±1.1 m/s), and **j** is the electric current density. These equations can be derived in several ways, one being from the conservation of magnetic and electric fields emanating from within an enclosed body of arbitrary shape. The first and second equations imply that any time-varying change in the magnetic or electric fields passing through the body induces a proportional electric or magnetic field, respectively. The third equation states that the total amount of electric field flux moving through a closed surface is equal to the total net charge enclosed within the surface. The final equation, Gauss' law of magnetism, implies that the net magnetic flux through any closed surface must be zero, as there are no free magnetic poles. The other useful relations that relate these equations to the magnetic permeability, specific conductivity and electric permittivity in isotropic media are

$$\mathbf{B} = \mu \cdot \mathbf{H}, \tag{4.5}$$
$$\mathbf{j} = \sigma \cdot \mathbf{E}, \tag{4.6}$$
$$\mathbf{D} = \epsilon \cdot \mathbf{E}. \tag{4.7}$$

Here, μ is the magnetic permeability, σ is the specific conductivity, and ϵ is the electric permittivity of the medium.

In non-electrically-conducting isotropic media (dielectrics), these equations simplify to

$$\nabla \times \mathbf{E} = -\frac{\partial \mathbf{B}}{\partial t} \tag{4.8}$$

$$\nabla \times \mathbf{H} = \frac{\partial \mathbf{D}}{\partial t} \tag{4.9}$$

$$\nabla \cdot \mathbf{D} = 0 \tag{4.10}$$

$$\nabla \cdot \mathbf{B} = 0. \tag{4.11}$$

and

$$\mathbf{B} = \mu \cdot \mathbf{H}, \tag{4.12}$$
$$\mathbf{D} = \epsilon \cdot \mathbf{E}. \tag{4.13}$$

A full discussion of the various methods for numerically solving these equations is not given here, but some useful methods can be found elsewhere[74]. The solution of these equations for the boundary conditions present at the surfaces of the two media involved in a reflection yields E and H for the incident, reflected and

transmitted light waves. These values then allow the computation of S, the Poynting vector. S is defined as the energy flux traveling in an electromagnetic wave, through a surface perpendicular to the direction of travel, and is calculated as

$$\mathbf{S} = \mathbf{E}\times\mathbf{H}. \tag{4.14}$$

S is a rapidly varying function of time, but its norm is the energy within a ray of light. The direction of travel of the light wave is given as S divided by the norm of S,

$$\text{Direction of Ray Propagation} = \frac{\mathbf{E}\times\mathbf{H}}{\|\mathbf{E}\times\mathbf{H}\|}. \tag{4.15}$$

Solving for the norm of **S** in the incident ray, reflected ray and the transmitted ray will indicate how much energy is absorbed, transmitted and reflected at an interface between two media, and will also indicate the direction the ray travels through a system.

4.3 Geometric Optics and the Fresnel Equations

Geometric optics, or ray tracing, treats light as a particle rather than a wave. As such, various effects such as diffraction, plasmonic effects and other phenomena are ignored. The advantage of using geometric optics is that the solutions to the propagation of light through a system are computationally facile, allowing for quick computation of results that are accurate when the simulated domain contains sufficiently large elements relative to the simulated wavelength of light. This allows one to simulate very large domains that are out of the reach of easy treatment using physical optics. The disadvantage of using geometric optics is that a relatively limited set of computational scenarios can be simulated with high accuracy.

Geometric optics is derived from Maxwell's equations by making the assumption that the wavelength of light, λ, is very small. This approach is generally considered valid when $\lambda << d$, where d is the smallest dimension of a reflecting or scattering body in a simulation domain.

Following the derivation given in Zohdi, Li and Qian[75], and beginning with a generic equation of a wave, one can write,

$$\nabla^2\psi = \frac{1}{c^2(x)}\frac{\partial^2\psi}{\partial t^2}, \tag{4.16}$$

where $c(x)$ is the spatially-varying speed of wave propagation in an inhomogeneous medium, which is related to the speed of wave propagation, c_o in some reference medium by the refractive index, n, by the relationship

$$n = c_o(x)/c(x). \tag{4.17}$$

Suppose that a trial solution for Equation 4.16 exists in the form,

$$\psi(x,t) = A(x)e^{j(k_o S(X)-\omega t)}, \tag{4.18}$$

where $A(x)$ is the wave amplitude, $k_o = 2\pi/\lambda$, or the wavenumber in the reference medium, $S(x)$ is the Eikonal (dimensions of length), t is the time, and ω is the angular frequency of the wave. By substituting equation 4.18 into the generic wave equation, one gets

$$k_o{}^2 A(n^2 - \nabla S \cdot \nabla S) + jk_o(2\nabla A \cdot \nabla S + A\nabla^2 S) + \nabla^2 A = 0. \tag{4.19}$$

As $\lambda \to 0$, the different terms containing k_o must equal zero in order for the equality to hold true. Using this, and by expanding the second-order k_o term, one obtains

$$n^2 = \nabla S \cdot \nabla S = \|\nabla S\|^2. \tag{4.20}$$

If the propagation medium is isotropic, n is constant, $\nabla^2 A = 0$, and the initial plane wave surface, S, is constant, then one can infer that, using Equation 4.19 where $n \neq 0$,

$$\nabla S(x) = n(x)\hat{s}(x), \tag{4.21}$$

where $\hat{s}(x)$ is the unit vector giving the direction of propagation of S(x), and $\nabla S(x)$ is perpendicular to S=constant. This allows one to represent light as a plane wave of collimated, coherent rays that are time marched in position via the explicit scheme,

$$\boldsymbol{r}(t + \Delta t) = \boldsymbol{r}(t) + \boldsymbol{V}(t)\Delta t, \tag{4.22}$$

where $\boldsymbol{r}(t)$ is a vector of the position of the ray, $\boldsymbol{V}(t)$ is the ray's velocity, and Δt is a time step chosen to be small enough to allow for accurate simulation of elements in the computational domain with size d and larger. If the medium through which the ray propagates is uniform, then $\boldsymbol{r}(t)$ is a straight line until a ray encounters an inhomogeneity in the index of refraction (i.e. an interface between two media).

Ray tracing uses a number of equations to predict the trajectory of and net energy loss from rays of light as they propagate through a system. To model the change in trajectory of a ray as encounters an interface between two media, one first makes the approximation that the reflection from the surface is specular, that is, the surface is locally infinitely smooth. Upon encountering such a surface, an incident ray that makes an angle θ_i with the surface's normal will reflect such that

$$\theta_r = \theta_i, \tag{4.23}$$

where θ_r is the angle that the reflected ray makes with the surface normal. The reflected ray's velocity is given by

$$\boldsymbol{V}' = \boldsymbol{V} - 2(\boldsymbol{V} \cdot \hat{\boldsymbol{n}})\hat{\boldsymbol{n}}, \tag{4.24}$$

where $\boldsymbol{V'}$ is the reflected velocity, $\boldsymbol{V}$ is the incident velocity vector and $\hat{n}$ is the surface normal. The normal of any surface that can be represented mathematically as $f_{Surf}(x, y, z)$ is, in Cartesian coordinates,

$$\hat{\boldsymbol{n}} = \frac{\nabla f_{Surf}(x,y,z)}{||\nabla f_{Surf}(x,y,z)||}. \tag{4.25}$$

The total distance traveled by a ray from one time step to another is given by

$$L = |\boldsymbol{r}(t_1) - \boldsymbol{r}(t_2)|, \tag{4.26}$$

where L has the units of distance and $\boldsymbol{r}(t)$ is the ray position at some time, t. If $\boldsymbol{r}(t)$ is known, and the time for a ray to collide with a plane with a certain normal needs to be calculated, this can be determined as

$$t_{Collision} = (\hat{n} \cdot \boldsymbol{p} - \hat{n} \cdot \boldsymbol{r}(t))/(\hat{n} \cdot \boldsymbol{V}(t)), \tag{4.27}$$

where $\boldsymbol{p}$ is a point on the wall, and $\hat{n}$ is the normal of the plane.

When a ray reflects, some of the ray's energy may transmit into the reflecting surface. In order to calculate this, one first needs to calculate the trajectory of the transmitted ray. For non-attenuating media, the angle that this transmitted ray makes with the surface normal, θ_t, is calculated using Snell's law,

$$n_t * sin(\theta_t) = n_o * sin(\theta_i), \tag{4.28}$$

which can be rearranged as

$$\theta_t = sin^{-1}(n_i * sin(\theta_i)/n_t) \tag{4.29}$$

where n_t is the refractive index of the reflecting surface and n_i is the refractive index of the medium from which the ray is incident. The relationship between $\hat{n}$, θ_i, θ_r, and θ_t is illustrated in Figure 4.1 a).

The definition of the refractive index of a material is given in Equation 4.17. In optics, there are two classes of materials: dielectrics, which are perfect electrical insulators that are transparent to light, and absorbing media, which absorb light that transmits through them. Dielectric media have an index of refraction that is entirely real, while the index of refraction of an absorbing medium has an imaginary component,

$$n_{Absorbing\ Medium}(\omega) = (n_{Real,\ medium} + i * k_{medium}), \tag{4.30}$$

where $i=\sqrt{-1}$. Most substances exhibit dielectric behavior for some wavelengths of electromagnetic radiation and absorbing behavior for others, hence the index of refraction is a function of the incident electromagnetic radiation's (EMR) frequency (known as a dispersion relation), as well as other variables, such as temperature.

The use of equation 4.29 to model the transmitted ray trajectory becomes problematic when any of the media involved are absorbing, because θ_t becomes a non-physical quantity with imaginary terms. However, transmission of a ray in an absorbing media back into a dielectric restores a real propagation trajectory. Methodologies for modeling the transmission of light through interfaces between dielectric and attenuating media will be discussed in Section 4.4.1 below.

When light impinges on a non-absorbing material interface, the conservation of energy holds such that

$$1 - R - T = 0, \tag{4.31}$$

where R is the fraction of energy reflected at the interface and T is the fraction transmitted through the interface. In other words, the sum of the resulting ray energies after a reflection process equals that of the incident ray.

Light occurs naturally in various states of polarization, that is, the orientation of the orthogonal electronic and magnetic components of the EMR waveform relative to the plane that contains the incident, reflected and transmitted light rays. Because light with any state of polarization can be represented as the summation of two orthogonal, linearly polarized waves, this derivation will consider the parallel and perpendicular polarizations, which refer to the orientation of the electronic component of the EMR to the plane of incidence and reflection. This is illustrated in Figure 4.1 b).

It is desirable to be able to calculate the reflectivity and transmission at a surface without explicitly solving Maxwell's equations using numerical methods. To do so, one begins by following the derivation in Hecht[76], considering a ray impinging on a flat surface, as shown in Figure 4.1 b). In this figure, the ray travels with a unit propagation vector, $\widehat{\boldsymbol{k}}$, and with phase velocity v. The plane wave can be described by the equation,

$$E_i = E_{oi}\cos\left(\boldsymbol{k_i}\cdot\boldsymbol{r} - \omega_i t\right), \tag{4.32}$$

where the wavevector of the incident plane wave is given by $\boldsymbol{k_i}$ and $\boldsymbol{r}$ is the position of the wavefront. The temporal and locational origin of the wave is arbitrary in space, such that one can write, for the reflected ray,

$$E_r = E_{or}\cos\left(\boldsymbol{k_r}\cdot\boldsymbol{r} - \omega_r t + \varepsilon_r\right), \tag{4.33}$$

and, for the transmitted ray,

$$E_t = E_{ot}\cos\left(\boldsymbol{k_t}\cdot\boldsymbol{r} - \omega_t t + \varepsilon_t\right), \tag{4.34}$$

where ε_r and ε_t are phase constants relative to E_i.

The EMR is perpendicularly polarized, and both the electric and magnetic fields are conserved. As a result, the component of the incident electric field that is tangential to the reflecting interface is continuous in the incident and transmitted

medium, and the component of the magnetic field that's perpendicular to the reflecting interface is continuous across the interface. The relation for the electric field can be expressed mathematically as

$$\boldsymbol{E_{oi}} + \boldsymbol{E_{or}} = \boldsymbol{E_{ot}} \tag{4.35}$$

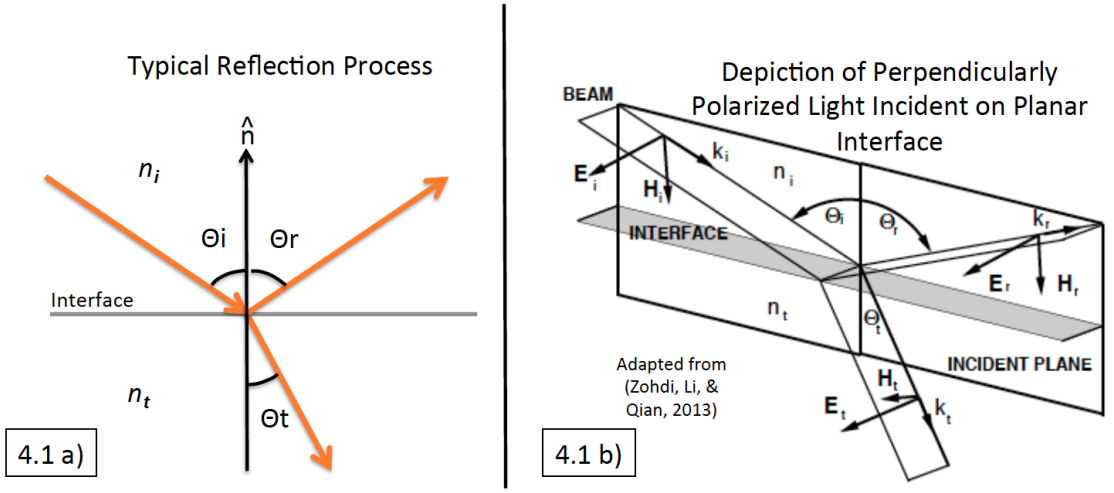

Figure 4.1: Depiction of Reflection-Related Nomenclature

The magnetic field of the EMR provides a useful starting point for this derivation. Using the conservation of this field across to materials with non-specified magnetic permeability, one can write,

$$-\frac{\mathbf{B_i}}{\mu_i}\cos(\theta_i) + \frac{\mathbf{B_r}}{\mu_i}\cos(\theta_r) = \frac{\mathbf{B_t}}{\mu_t}\cos(\theta_t). \tag{4.36}$$

From [76], one has

$$\hat{\boldsymbol{k}}\times\boldsymbol{E} = v\boldsymbol{B}, \tag{4.37}$$

which gives,

$$\boldsymbol{B_i} = \boldsymbol{E_i}/v_i, \tag{4.38}$$
$$\boldsymbol{B_r} = \boldsymbol{E_r}/v_r, \tag{4.39}$$

and

$$\boldsymbol{B_t} = \boldsymbol{E_t}/v_t. \tag{4.40}$$

Because $\theta_i = \theta_r$, and $v_i = v_r$, one can rewrite equation 4.36 as

$$\frac{1}{\mu_i v_i}(E_i - E_r)\cos(\theta_i) = \frac{1}{\mu_t v_t}E_t\cos(\theta_t) \tag{4.41}$$

Using equations 4.32-4.34, and recognizing that their cosine terms are equal at the point of reflection, one calculates

$$\frac{n_i}{\mu_i}(E_{oi} - E_{or})\cos(\theta_i) = \frac{n_t}{\mu_t}E_{ot}\cos(\theta_t). \quad (4.42)$$

Now, using the fact that the component of the electric field tangential to the reflecting interface is continuous, one derives

$$(\frac{E_{or}}{E_{oi}})_\perp = r_\perp = \frac{\frac{n_i}{\mu_i}cos(\theta_i) - \frac{n_t}{\mu_t}cos(\theta_t)}{\frac{n_i}{\mu_i}cos(\theta_i) + \frac{n_t}{\mu_t}cos(\theta_t)}, \quad (4.43)$$

and

$$(\frac{E_{ot}}{E_{oi}})_\perp = t_\perp = \frac{2\frac{n_i}{\mu_i}cos(\theta_i)}{\frac{n_i}{\mu_i}cos(\theta_i) + \frac{n_t}{\mu_t}cos(\theta_t)}. \quad (4.44)$$

Extending the derivation to the parallel polarization of light, and recognizing the continuity of the electric field across the boundary, one can show that

$$E_{oi}\cos(\theta_i) - E_{or}\cos(\theta_r) = E_{ot}\cos(\theta_t) \quad (4.45)$$

Continuity of the tangential components of $\boldsymbol{B}/\mu$ gives

$$\frac{1}{\mu_i v_i}E_{oi} + \frac{1}{\mu_r v_r}E_{or} = \frac{1}{\mu_t v_t}E_{ot} \quad (4.46)$$

By recognizing that $\theta_i = \theta_r$, and $\mu_i = \mu_r$, one can combine equations 4.45 and 4.46 as

$$(\frac{E_{or}}{E_{oi}})_\parallel = r_\parallel = \frac{\frac{n_t}{\mu_t}cos(\theta_i) - \frac{n_i}{\mu_i}cos(\theta_t)}{\frac{n_i}{\mu_i}cos(\theta_i) + \frac{n_t}{\mu_t}cos(\theta_t)}, \quad (4.47)$$

and

$$(\frac{E_{ot}}{E_{oi}})_\parallel = t_\parallel = \frac{2\frac{n_i}{\mu_i}cos(\theta_i)}{\frac{n_i}{\mu_i}cos(\theta_t) + \frac{n_t}{\mu_t}cos(\theta_i)}. \quad (4.48)$$

For unpolarized (natural) sunlight, one can then calculate the total reflectance as

$$R = \frac{1}{2}(r_\perp^2 + r_\parallel^2), \quad (4.49)$$

and the total transmittance as

$$T = \frac{1}{2}(t_\perp^2 + t_\parallel^2). \quad (4.50)$$

For most materials, the magnetic permeability is equal to the free space magnetic permeability, i.e. $\mu_o = \mu_t = \mu_f$, and $\mu_f = 4\pi 10^{-7}$ Wb/A-m. This allows the terms containing the magnetic permeability to drop out.

Returning to the earlier discussion of Snell's law, If the incident angle of light is such that $n_i \, sin(\theta_i) \, / n_t$ is greater than one, then one has a condition known as total reflection, such that, practically speaking, none of the energy of the incident ray is transmitted into the media upon which it impinges. In these instances, T = 0. In actuality, a rapidly decaying wave is propagated into the adjacent medium, which decays in a distance on the order of $\lambda/(2\pi)$ (p. 50, [77]). The principle of total internal reflection is harnessed in such devices as fiber optics, and is also harnessed in some of the lenses discussed in Section 4.5.

4.4 Methods for Characterizing Reflections from Thin Films and Metals

4.4.1 The Transfer Matrix Method

Ultimately, the Fresnel relations are useful for analyzing any planar, isotropic optical media. Extending their use to attenuating media, however, requires a bit of extra computation given the non-physical propagation angle of light in such media. Additionally, as discussed in Section 4.4.4, one would like to model the interaction of light with thin films used on the surface of the PV cell and elsewhere. Thus the Transfer Matrix Method (TMM) is outlined here, which follows the outline given by Byrnes[78]. A full derivation of the TMM is given in chapter 4 of Heavens[79], but is left out for brevity.

To begin the derivation of the TMM, one can imagine a stack of $N - 2$ thin films whose thicknesses are below the criterion for ray tracing (since λ is on or greater than the order of the film thickness), since one cannot treat the EMR as a particle. This is depicted in Figure 4.2. These thin films are bounded at the bottom and top by semi-infinite layers, at positions $n = 0$ and $n = N - 1$, respectively. The incident wave begins at the bottom of the figure (layer 0) and travels progressively up through the layers. At each interface, there is a finite reflected and transmitted component of the light, and the reflected component of light from each of the N layers contributes to the overall reflectance of the stack.

At the first stack, one assumes the amplitude of the ray is unity. At the interface between the arbitrarily defined $(n-1)^{th}$ and n^{th} layer, one lets the amplitude of the light heading upwards from the interface, (towards layer $n = N - 1$) be a_n, and one lets the amplitude of light heading downwards (towards layer $n = 0$) be b_n. $a_{N-1} = t$ and $b_{N-1} = 0$, where t is the fraction of energy that is transmitted through the thin film stack. One can then write

$$\begin{pmatrix} a_n \\ b_n \end{pmatrix} = \boldsymbol{M_n} \begin{pmatrix} a_{n+1} \\ b_{n+1} \end{pmatrix}, \tag{4.51}$$

where

$$\boldsymbol{M_n} = \begin{pmatrix} e^{-i\delta_n} & 0 \\ 0 & e^{i\delta_n} \end{pmatrix} \begin{pmatrix} 1 & r_{n,n+1} \\ r_{n,n+1} & 1 \end{pmatrix} \frac{1}{t_{n,n+1}} \tag{4.52}$$

for $n = 1, \ldots, N-2$, and where δ is given as

$$\delta_n = 2\pi(n_{Real,n} + ik_{Complex,n}) \cos(\theta_{i,n})\, d_n/\lambda_0. \tag{4.53}$$

Here, r_n and t_n are the (potentially complex) reflectivity and transmissivity of the interface between layers n and n+1 as calculated with Equations 4.43 and 4.44 or 4.47 and 4.48 (depending on the polarization), $(n_{Real,n} + ik_{Complex,n})$ is the complex index of refraction of layer n, λ_0 is the wavelength in vacuum, $\theta_{i,n}$ is the (potentially complex) angle that the ray makes with the normal to the interface in layer n and d_n is the thickness of layer n.

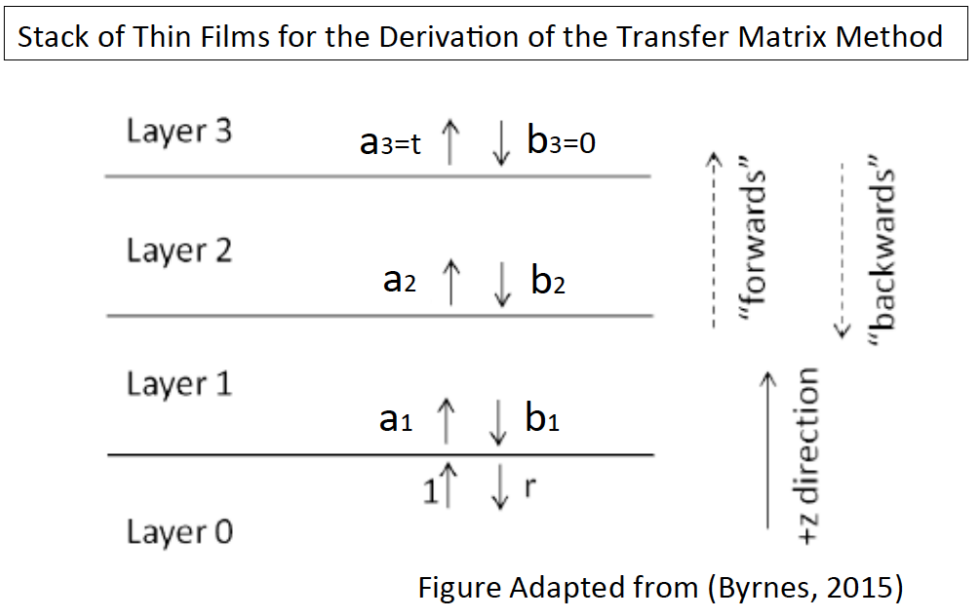

Figure 4.2: Depiction of Thin Film Stack

To combine the effect of multiple layers, one performs the operation,

$$\tilde{\boldsymbol{M}} = \frac{1}{t_{0,1}} \begin{pmatrix} 1 & r_{0,1} \\ r_{0,1} & 1 \end{pmatrix} \boldsymbol{M_1 M_2 \ldots M_{N-1}} \tag{4.54}$$

and, combining Equation 4.54 with the following,

$$\begin{pmatrix} 1 \\ r \end{pmatrix} = \tilde{\boldsymbol{M}} \begin{pmatrix} t \\ 0 \end{pmatrix} \tag{4.55}$$

allows one to write r and t, the reflection and transmission from a particular stack at a certain polarization, in terms of $\widetilde{\boldsymbol{M}}$ as

$$\begin{pmatrix}1\\ r\end{pmatrix} = \begin{pmatrix}\widetilde{\boldsymbol{M}}_{\boldsymbol{00}} & \widetilde{\boldsymbol{M}}_{\boldsymbol{01}}\\ \widetilde{\boldsymbol{M}}_{\boldsymbol{10}} & \widetilde{\boldsymbol{M}}_{\boldsymbol{11}}\end{pmatrix}\begin{pmatrix}t\\ 0\end{pmatrix}, \tag{4.56}$$

or

$$t = 1/\widetilde{\boldsymbol{M}}_{\boldsymbol{00}}, \tag{4.57}$$

and

$$r = \widetilde{\boldsymbol{M}}_{\boldsymbol{10}}/\widetilde{\boldsymbol{M}}_{\boldsymbol{00}}, \tag{4.58}$$

where the subscripts are the indices of the term $\widetilde{\boldsymbol{M}}$.

4.4.2 Reflections from Metallic Surfaces

Simpler relations are used to calculate the reflectivity of light incident from a dielectric to an optically thick metal (i.e. a substance where $|n_t| \gg 1$ and $d \gg \lambda$). These are adapted from p. 197 of Nalwa[80], and are given here without derivation. Other such relations can be found in, e.g. [81].

$$r_{\perp,Comp} = \frac{(n_{Real,i}\cos(\theta_i) - ((n_{Real,t}+ik_{Complex,t})^2 - {n_{Real,i}}^2\sin(\theta_i))^{\frac{1}{2}}}{(n_{Real,i}\cos(\theta_i) + ((n_{Real,t}+ik_{Complex,t})^2 - {n_{Real,i}}^2\sin(\theta_i))^{\frac{1}{2}}} \tag{4.59}$$

$$r_{\parallel,Comp} = \frac{(n_{Real,t}+ik_{Complex,t})^2\cos(\theta_i) - n_{Real,i}((n_{Real,t}+ik_{Complex,t})^2 - {n_{Real,n}}^2 * \sin(\theta_i))^{\frac{1}{2}}}{(n_{Real,t}+ik_{Complex,t})^2\cos(\theta_i) + n_{Real,i}((n_{Real,t}+ik_{Complex,t})^2 - {n_{Real,n}}^2 * \sin(\theta_i))^{\frac{1}{2}}} \tag{4.60}$$

where the indices of *i* and *t* denote the incident (dielectric) and transmitted (metallic) media, respectively.

To extract the overall reflectance, one must take the complex conjugate of these values above, such that

$$R_\perp = r_{\perp,Comp}{r_{\perp,Comp}}^* \tag{4.61}$$

$$R_\parallel = r_{\parallel,Comp}{r_{\parallel,Comp}}^* \tag{4.62}$$

4.4.3 Light Attenuation and Scattering in Non-Dielectric Media

As light propagates through a medium that is not a dielectric, it will be absorbed during its passage. Dielectric media will also potentially scatter light. One would like to be able to model this effect in this analysis in order to determine the transmission efficiency of the PEC.

Following the derivation in Siegel, Howell and Mengüç[81], as spectral radiation propagates through a volume of absorbing and scattering medium of length dS, the intensity of the radiation will be reduced. The relation describing this process is

$$dI_\lambda(\boldsymbol{r},\Omega) = -\beta_\lambda(\boldsymbol{r})I_\lambda(\boldsymbol{r},\Omega)d\boldsymbol{r}, \tag{4.63}$$

where $I_\lambda(\boldsymbol{r},\Omega)$ is the spectral intensity at vacuum wavelength λ, position **r** and of solid angle Ω, and $\beta_\lambda(\boldsymbol{r})$ is the attenuation coefficient of the medium. The attenuation coefficient can be broken into components related to scattering and absorption,

$$\beta_\lambda = \kappa_\lambda + \sigma_{s\lambda}, \tag{4.64}$$

where $\sigma_{s\lambda}$ is the scattering coefficient at wavelength λ and κ_λ is the attenuation coefficient. Absorption converts optical energy into thermal energy, whereas scattering is an elastic process that changes the direction of the incident radiation but does not convert the optical energy into heat. Integrating Equation 4.63 over a differential optical path length, one can derive an analytical relationship for the attenuation of light as it moves through the medium. One first obtains, for the direction Ω,

$$\int_{I_\lambda=I_\lambda(0)}^{I_\lambda(\boldsymbol{r})} \frac{dI_\lambda}{I_\lambda} = -\int_{\boldsymbol{r}^*=0}^{\boldsymbol{r}} \beta_\lambda(\boldsymbol{r}^*)d\boldsymbol{r}^*, \tag{4.65}$$

where $I_\lambda(0)$ is the intensity incident on the control volume at $\boldsymbol{r}=0$ and $\boldsymbol{r}^*$ is a dummy variable of integration. In this analysis, scattering is ignored, and thus, performing the integration, one has,

$$I_\lambda(\boldsymbol{r}) = I_\lambda(0)\exp\left(-\boldsymbol{r}\kappa_{\lambda,Medium}\right). \tag{4.66}$$

To calculate κ_λ of the medium, one uses the imaginary component of the index of refraction of the medium,

$$\kappa_{\lambda,Medium} = 4\pi k_{Medium}/\lambda_0. \tag{4.67}$$

4.4.4 Reflection Management at Thin Films and Reflective Surfaces

In any PV-containing system, the use of reflection management is crucial to ensure high efficiency light throughput to the active layers of the PV cell. Per Equations 4.43 and 4.47, as well as Equations 4.59-4.62, the higher the disparity between the index of refraction of two media, the greater the reflection at that surface. Typical

semiconductors used in PV materials (e.g. Si) have would exhibit reflectance on the order of 30% at normal incidence if directly exposed to air. Thus, real systems have a variety of means for reducing surface reflectivity, to enhance optical throughput.

There are multiple methods to achieve reductions in reflections. Generally, these methods either make the transition in index of refraction smooth, or they employ thin film layers in order to use destructive interference to reduce the amplitude of the reflected light waves. The transition in the index of refraction between two materials can be made smooth by employing porous or composite media whose features are significantly smaller than the wavelength of the incoming light. For further discussion, the reader is referred elsewhere[82]. This work will focus on the use of antireflection coatings (ARCs).

The simplest type of ARC is depicted in Figure 4.3. In such a system, the coating is designed to be ¼ of λ_{ARC}, the wavelength of light in the ARC, and to have an index of refraction equal to $n_{ARC} = (n_o n_1)^{0.5}$. As such, when light impinges on the surface, the ARC creates two reflected waves that are 180° out of phase with one another. These waves will cancel one another, and the total reflection will be zero at the particular wavelength for which the system is optimized. By equation 4.31, this implies that the total transmitted energy, if the film is negligibly absorbing, is equal to the incident energy. For wavelengths away from that for which the system is optimized, however, the reflectivity is higher, as is the case for light incident from oblique angles though at the optimized wavelength, since the effective path length of light in the ARC layer varies from $\lambda_{ARC}/4$. Creating multiplayer periodic systems can enhance the wavelength range over which reflectivity between the ambient and the PV cell is reduced[83], though this is left for future work.

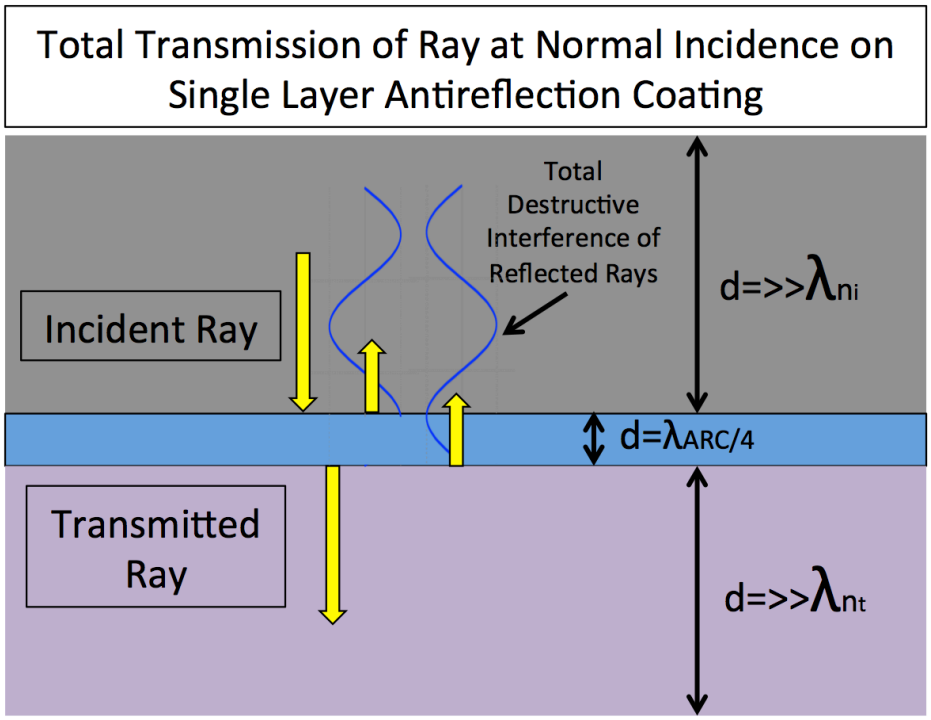

Figure 4.3: Depiction of 1-Layer Antireflection Coating

Conversely, for any reflective lens, one would like to enhance the reflectivity of the surface as much as possible in order to maximize light throughput by the system. Options to achieve such reflectivity include the use of metalized surfaces, or of multilayer periodic systems such as a Bragg reflector. For simplicity, the systems modeled in this work will employ thick metallized surfaces. Metals are reflective because of having extremely high attenuation coefficients, such that the light penetration within the metal is typically several orders of magnitude smaller than the incident wavelength itself. Relatively few electrons in the metal are able to interact with the light, and thus, while those are strongly attenuating, the majority of the incident optical energy is reflected (p. 110, Hecht[76]).

4.5 Nonimaging Optically Concentrating Lenses

The use of nonimaging optically concentrating lenses is one of the primary focal points of this analysis (that is a pun), for its ability to reduce the size of PV and electrochemical componentry in a PEC is an avenue for the reduction of the EROEI of the device. All elastic concentrators follow some basic principles, which are outlined here, followed by discussion of several specific device architectures.

A basic principle in all elastic concentrators (i.e., one that does not change the frequency of the photons delivered from the aperture to the lens' receiver) is a concentration ratio-, and material-dependent acceptance and receiver angles. This is depicted in Figure 4.4. This results from the need for a conservation of radiance (analogous to the conservation of energy). The Étendue for a solid angle of light is calculated as, for a 2D system

$$G_s = \pi dA_s n_s sin(\theta_s), \tag{4.68}$$

where G_s is the Étendue, dA_s is the area subtended by the solid angle of light, n_s is the index of refraction of the medium in which the light travels, and θ_s is the angle subtended by the solid angle of light. For a 3D system, the Étendue is given by

$$G_s = \pi dA_s n_s^2 \sin^2(\theta_s). \tag{4.69}$$

Using the conservation of Étendue, it can be shown[84] that, for any concentrator geometry, the relation between maximum possible concentration ratio, acceptance angle, receiver angle, index of refraction of the receiver and index of refraction of the aperture can be characterized as, for 2D (trough-like) geometries,

$$CR_{Max,2D} = \frac{A_A}{A_R} = \frac{G_R}{G_A} = \frac{n_R \sin(\theta_R)}{n_A \sin(\theta_A)}, \tag{4.70}$$

where $CR_{Max,2D}$ is the maximum concentration ratio A_A is the area of the aperture, A_R is the area of the receiver (where the light is focused), n_R is the index of refraction of the receiver, n_A is the index of refraction of the aperture (air, or nearly

unity), θ_R is the receiver angle, or the maximum angle at which light that is incident on the aperture can exit the concentrator, and θ_A is the acceptance angle, or the maximum angle that light can make with the normal to the plane of the concentrator's aperture and still be delivered to the receiver. For 3D systems (cone-like devices),

$$CR_{Max,3D} = \frac{A_A}{A_R} = \frac{G_R}{G_A} = \frac{n_R^2 \sin^2(\theta_R)}{n_A^2 \sin^2(\theta_A)}. \quad (4.71)$$

As the concentration ratio increases, the acceptance angle decreases for a fixed receiver angle and indices of refraction in the system. Radiation that falls beyond the acceptance angle is generally rejected back out of the aperture of a concentrator after multiple internal reflections, though real-world transmission profiles exhibit some transmission beyond the acceptance angle due to manufacturing errors and other effects[85].

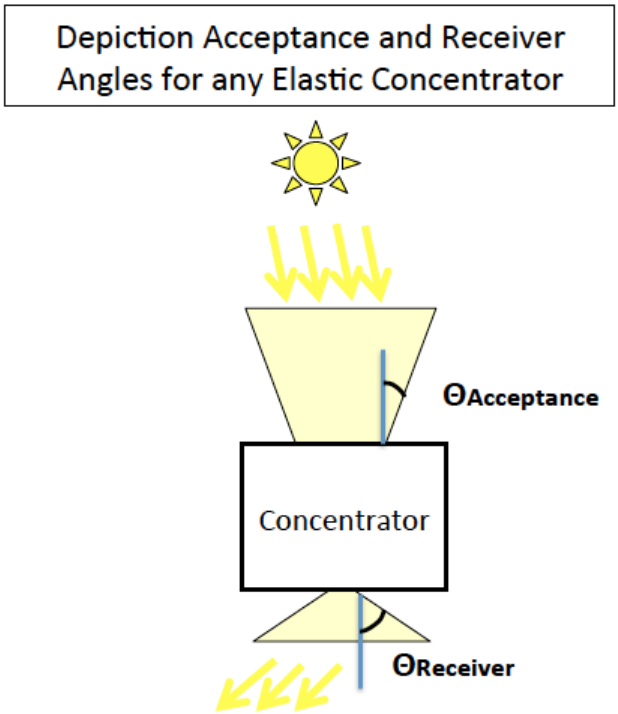

Figure 4.4: Depiction of Elastic Concentrator Nomenclature

As a result, any high-concentration system only accepts light from a narrow beam of incident light, which leads to the necessity to track the sun's position throughout the year for concentration ratios above about 2.5[86]. In some systems, such as Fresnel lenses, the need for tracking is compounded by a change in the focal length for light that does not fall within the plane perpendicular to a lens' primary axis[87]. Despite the need for tracking, it is not necessarily desirable. In the initial phase of PV deployment, success was found in remote applications where grid connections would have been prohibitively expensive[88]. If PECs are developed commercially, they will likely first be deployed in similar applications where the

cost of fossil fuel is higher than in locations with better access to fuel distribution infrastructure. In these markets, simplicity and reliability, or absence altogether of tracking mechanisms may be of considerable importance.

Due to scattering in the atmosphere, a significant portion of the annual global horizontal solar resource in any geographical location is in the form of diffuse light, such that it is incident from across the hemisphere subtended by the earth's atmosphere. In the U.S., at minimum, about 15% of the incident light is diffuse (NREL, 2015) in regions of high direct insolation resource. Any optically concentrating system will transmit less energy to an intended receiver than a system with no optical concentration. Therefore, the necessity for tracking, as well as the effect on device performance of how much of a site's annual solar resource falls in the form of diffuse radiation are explored in Chapter 6.

Many different types of concentrators exist, generally falling into the categories of imaging (those that create an image of the source) and nonimaging optics. This analysis will focus on the latter class of devices. Within the general class of nonimaging optics, there exist both refractive and reflective optical systems. Refractive optics relies on the change in trajectory of light as it moves between materials of differing refractive index to focus light on a receiver. Typical lenses of this type include Fresnel lenses. Reflective optical systems rely on reflections from their surfaces to redirect light towards a receiver. Examples of this class of concentrator are parabolic concentrators, systems that employ power towers and heliostats, and certain classes of Fresnel lens. The reader is directed elsewhere[89] for further information. This work will focus on compound parabolic concentrators (CPCs) and dielectric, totally internally reflecting concentrators (DTIRCs).

A profile of a typical CPC is given in Figure 4.5 a). As first shown by Winston[84], the CPC is highly efficient and delivers close to the theoretical maximum concentration ratio given above in Equations 4.70 and 4.71. In order to model these systems, a series of design equations that give the surface of the CPC are necessary. To model the system, one uses the equation for the surface of the concentrator. For a Cartesian coordinate system, the equation of the CPC surface is

$$\begin{aligned}((x^2+y^2)^{0.5}\cos(\theta_{Inside})+zsin(\theta_{Inside}))^2 \\ +2r_{Receiver}(1+\sin(\theta_{Inside}))^2(x^2+y^2)^{0.5} \\ -2r_{Receiver}\cos(\theta_{Inside})\,(2+\sin(\theta_{Inside}))z-{r_{Receiver}}^2(1 \\ +\sin(\theta_{Inside})\,(3+\sin(\theta_{Inside}))-1=0,\end{aligned} \tag{4.72}$$

where θ_{Inside} is the angle displayed in Figure 4.5 a), and $r_{Receiver}$ is the radius of the receiver. The equation for the normal of a CPC is given by combining equations 4.25 and 4.72, though is not explicitly given here for brevity. Using Equation 4.72, it is possible to determine that a ray at position ***r(t)*** is on the surface of the CPC when the equality is satisfied. Once it is determined that this is so, the normal at that point on the CPC can be found, and so can the trajectory of a reflected ray be determined, using equation 4.24.

The uppermost portion of a CPC can be truncated without appreciable loss in concentration ratio (as given by equations 4.71 and 4.72)[90]. Ultimately, this

truncation also allows for the reduction in optical loss in both refractive and reflective CPCs, and the use of truncation is employed in the results shown in this chapter and Chapter 6.

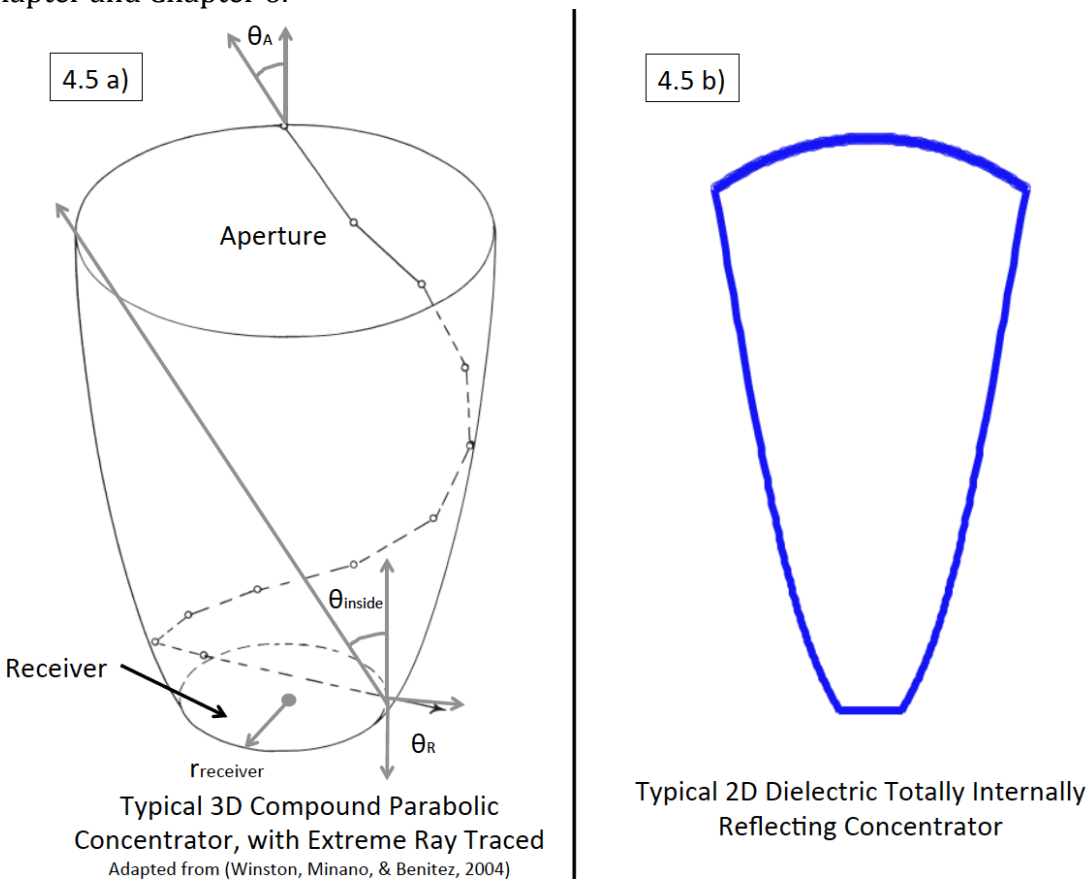

Figure 4.5: Profiles of Typical Compound Parabolic Concentrator and Dielectric Totally Internally Reflecting Concentrator

DTIRCs represent another methodology for concentrating light on a receiver explored in this work. By using a curved top surface a solid dielectric material as the internal light transmitting media, they have similar theoretical efficiencies as CPCs, but with truncated height. Additionally, their design allows for a restriction of the exit angle, at the expense of acceptance angle ratio for a given concentration ratio. Their design was first presented by Ning, Winston and O'Gallgher[85], and their design is again outlined in pp. 51-52 of Chaves[89]. The method employed in this work follows the design strategy whereby rays that incident at the acceptance angle and on the extrema of the aperture are traced, given the known concentration ratio and desired radius of curvature of the aperture surface. Then, one can design the side profile of the lens by enforcing constant optical length (Fermat's theorem) for all rays in the system, such that the sum of the products of the ray path lengths and the index of refraction of the media through which the rays travel is identical for all rays incident at the acceptance angle, or in other words,

$$C = \sum_{l=1}^{3\ or\ 4} n_l L_l \quad \forall\ Rays, \tag{4.73}$$

where the subscript, *l* gives the number of line segments a ray makes in its travel through a 2-D cross section of a DTIRC. A profile of a typical DTIRC is provided in Figure 4.5 b). If the aperture of the lens is flat, then one can use the same process to design lenses that are reflective but have a finite exit angle.

Ultimately, once the outlines of the DTIRC are traced out using the scheme detailed above, one is left with a series of points on the absorber walls. This means that the program must store these data, and approximate the profile of the DTIRC as a series of truncated cones with known bounding radii and positions. Then, for each cone, the program uses the equation for an ellipse,

$$\left(\frac{(x-x_c)^2}{a^2} + \frac{(y-y_c)^2}{b^2}\right)^{0.5} - 1 = 0, \tag{4.74}$$

where x_c and y_c are the locations of the center of the ellipse, and a and b are the major and minor radii of the ellipse, to determine if points x and y are on the surface of the ellipse.

Fresnel lenses can also be utilized as efficient means of concentrating energy on PEC systems[91]. However, because of the necessity of 2-axis tracking in Fresnel lenses[87], and lower theoretical efficiency of Fresnel lenses than CPCs and DTIRCs[92], they were not investigated in this work. The emphasis on high transmission efficiency and system lifetime also precluded the study of luminescent concentrators[93]. However, luminescent systems represent an interesting alternative owing to the lack of need for tracking because such systems are not bound by the conservation of Étendue, as are elastic concentrators.

4.6 Optics of the Atmosphere

In order to simulate how a deployed PEC works, the program must be able to model the incident solar resource. To do this, annual weather data of hourly direct and diffuse solar radiation resource were sourced from the typical meteorological year (TMY) database (NREL, 2015). This data gives hourly direct and diffuse light resources, the ambient temperature, humidity and cloud cover, and the wind speed and direction for a typical meteorological year for over 200 locations across the United States. A tracking code was then created to calculate the position of the sun relative to the CPEC aperture[94] and the desired tracking methodology (fixed, or 1- or 2-axis tracking). The AM 1.5 D spectrum was utilized to estimate the direct photon flux's spectral profile, whilst the difference between the AM 1.5 G and the AM 1.5 D spectrum was used to model the diffuse radiation's spectral profile. Both of these spectrums provide a standard model of the irradiation spectra incident on earth, after the irradiation from the sun is attenuated by absorption and scattering in the Earth's atmosphere. In reality, no one fixed model can capture this spectra, as it is time varying. More precise estimates of the solar resource's variations that take into consideration atmospheric phenomena such as water and aerosol content can be

found in, e.g. (NREL, 2010). This was deemed to not be the focus of the work, and thus is left out of the model. The distribution of diffuse radiation in the sky is assumed to be uniform, which is a conservative estimate given the fact that a large portion of the diffuse radiation is incident from a disc surrounding the sun, and thus would be more likely to be within the acceptance angle of the concentrator. A more accurate estimate of the directional component of the diffuse radiation is given in other works[95].

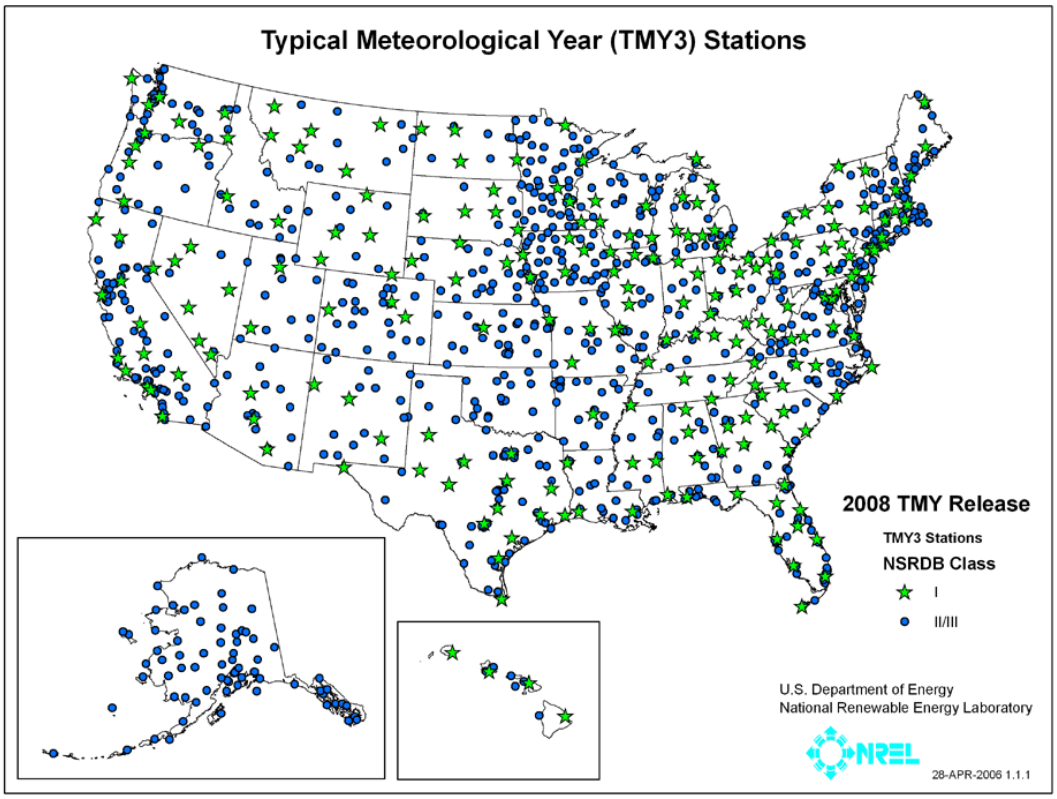

Figure 4.6: Map of Available Datasets for Simulation (NREL, 2015)

4.7 Overall Computational Scheme

The overall computational scheme employed in this work to calculate the hourly photon flux to the PV cell in the CPEC is presented as Figure 4.7 in a flow diagram below. A schematic of a prototypical wireless integrated lens-PEC unit is shown in Figure 4.8. Results from some trial computations are shown in Figure 4.9 and 4.10.

To calculate the hourly photon flux on the PV cell, one first needs to determine the photon throughput efficacy as a function of incident angle and light frequency. To calculate the throughput efficiency, first the concentrator type, concentration ratio, receiver angle, antireflection coating types and materials, the internal system dimensions, the number of rays, the λ_0 for which the system is

optimized, the range of incident light λ_0 and its trajectories are input to the program. Following that, for a given value of λ_0, the indices of refraction for the various materials in the system are interpolated from the reference data tabulated in Table 4.1. Then, each ray is traced through the lens system using Equation 4.22, with dt (units of s) chosen such that.

$$dt = \frac{d}{100V}, \tag{4.75}$$

where d is the receiver radius (the smallest dimension in the lens system). The unitless constant in the denominator was found by trial and error, as smaller values resulted in computational errors in calculating the rays' trajectories, and larger values resulted in unnecessarily long computation time. At each time step, Equation 4.72 or 4.74 is queried to determine if the ray is inside or outside of the reflective lens walls for systems using CPCs or DTIRCs, respectively. When a ray encounters an interface between two media at the lens walls, or the aperture or receiver of the lens, the point of reflection is calculated. The total path length, L, traveled by that segment of the ray in a particular media is calculated, and Equations 4.66 and 4.67 are used to calculate the energy dissipated by optical absorption in the media, if applicable. Then, the appropriate values of $R_\perp$, $R_\parallel$, $\alpha_\perp$, $\alpha_\parallel$, $T_\perp$and $T_\parallel$ are calculated, based upon the type of interface that the ray reflects from, where α is the amount of light absorbed via Beer-Lambert absorption. The amount of ray energy remaining in both parallel and perpendicular polarizations is then calculated, as is the amount of energy transmitted into the surface upon which light is incident. When the ray energy is below a certain threshold, the simulation moves to the next ray, until all simulated rays have below the minimum energy threshold. This is shown in Figure 4.7.

Having simulated the initial passage of light through the lens system, a similar process begins within the PEC. The initial trajectories and energies of the rays in the PEC are fed from the ray tracing simulation in the lens. Instead of using the iterative ray-tracing scheme given in Equation 4.22, however, Equation 4.27 is used to calculate the time to collision for each of the bounding surfaces of the PEC (the chamber walls, the PV cell, the membrane and the window to the lens). Because of the planar nature of the walls enclosing the PEC, this greatly speeds computation time. The minimum time to collision that is greater than 0 s is found, and then it is determined if the point is indeed within the bounds of the wall. If not, the process cycles back to using Equation 4.27, with the previously found wall removed from the candidate list. If the wall is correctly identified, the total distance traveled in the electrolyte, L, from the last reflection is calculated. This distance is input into Equations 4.66 and 4.67 to calculate the absorption of light in the electrolyte. Then, as before, the appropriate values of $R_\perp$, $R_\parallel$, $\alpha_\perp$, $\alpha_\parallel$, $T_\perp$and $T_\parallel$ are calculated, based upon the type of interface that the ray reflects from. If a ray is incident on the PV cell/catalyst stack, the TMM is used to simulate the transmitted energy's progress from electrolyte through a catalyst, protection layer and infinitely thick layer of the top semiconductor junction of the light absorber. This system (minus the infinite thickness of the semiconductor layer) is depicted in Figure 4.8. The ray is simulated

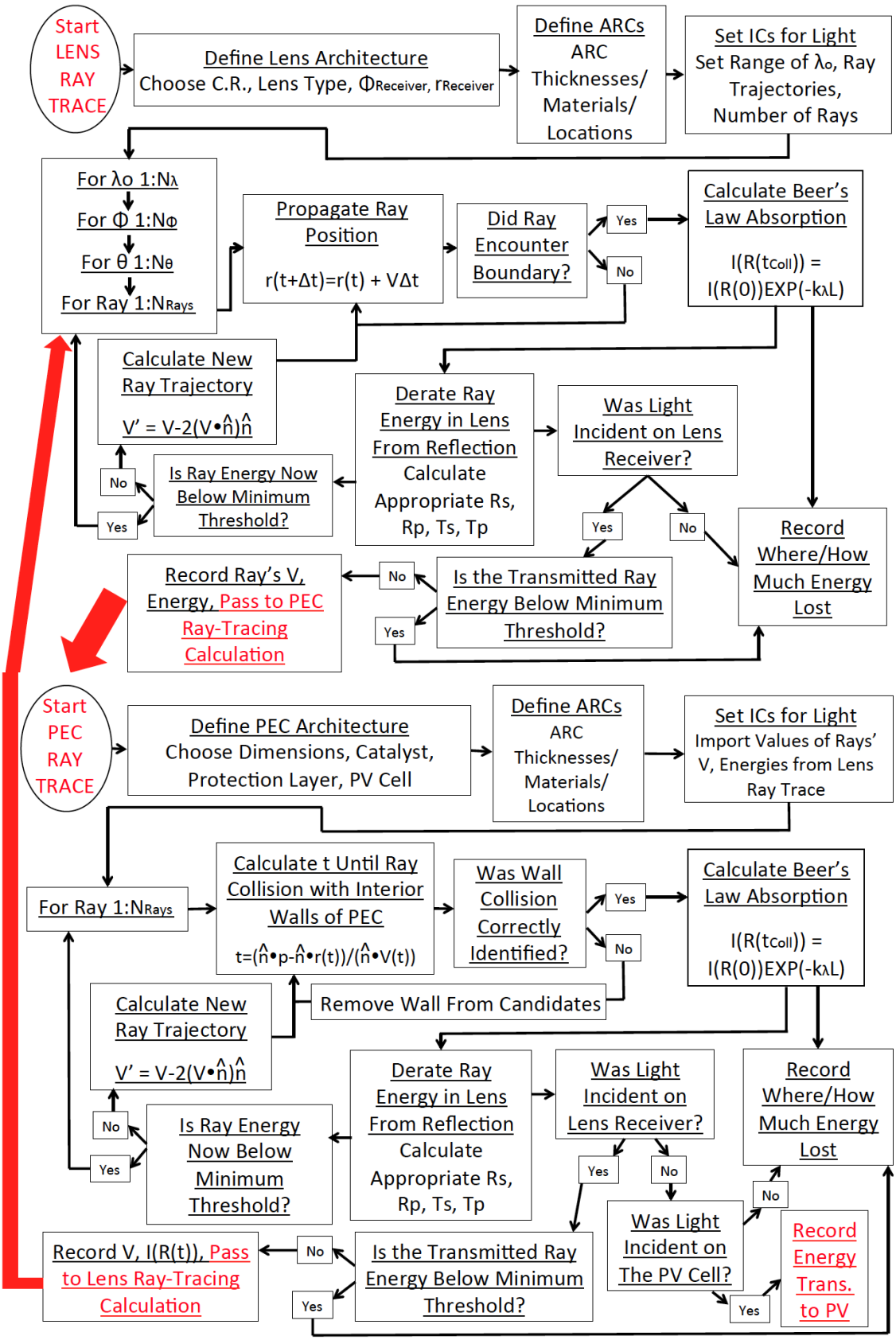

Figure 4.7: Overall Ray Tracing Scheme Program Flow

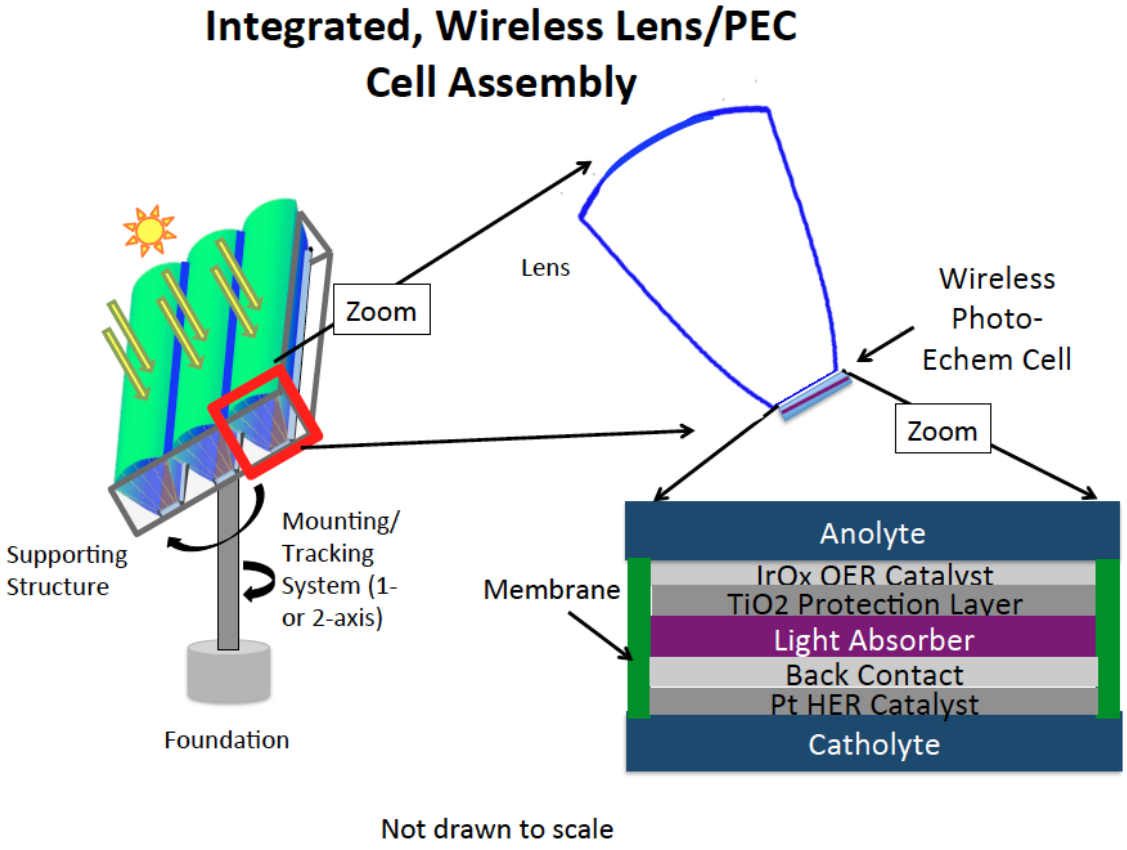

Figure 4.8: Depiction of Simulated Device, with Emphasis on Lens/PEC Combination

until the total energy is below a certain threshold, and then the next ray is simulated. This too is shown in Figure 4.7.

This overall process is repeated, cycling from the lens to the PEC, and back, until the total energy in the simulation (both the lens and the PEC) is below a threshold. Then, the next value of trajectory is chosen for a given λ_0, and, once all trajectories are calculated, the simulation moves on to the next value of λ_0, and so on, until all trajectories and values of λ_0 are simulated. Once the simulation has finished, the total energy transmitted to the PV cell's active layers is recorded, as is where energy is "lost" in the system if it does not end up in the active layers of the PV cell.

The next step for utilizing such data is to calculate, hour by hour, the directional and spectral profile, and the intensity of light incident on the lens surface using the computational scheme discussed in Section 4.6. Using the optical transmission profile and the PV-Electrochemical model developed in Chapter 3, the program can calculate the hourly operational current density of the system for a particular hour.

4.8 Some Results from the Optical Computational Scheme

Having assembled the necessary components to produce a code that can simulate the passage of light through the system, some pertinent conclusions can be made. This section will examine three lens designs in order to demonstrate the reasoning behind some broader design decisions that will guide the whole-device simulations in Chapter 6. For the following design tests, 5,000 randomly-placed rays at normal incidence are simulated, from 300-1800 nm, in order to model the important above-bandgap portion of the insolation spectrum. A depiction that is helpful for the reader to identify points of loss in the system is given as Figure 4.11.

The overall design goal for the optical components in the PEC is to send as many above-bandgap photons as possible into the PV cell's active layers, in order to produce the highest possible value of J_{SC} for the entire cell. However, for PV systems considered in this work, under the AM 1.5 D spectrum, one junction is starved of above-bandgap photon flux relative to the others, as shown in the perfect transmission case in Figure 4.10. This under-driven junction will limit the total cell's J_{SC} (as given in Equation 3.22), thus limiting the maximum possible fuel production rate. For the triple junction cell introduced in Chapter 3, the middle junction is under-driven, which gives us design space to optimize the device by allowing both high- and low-energy photons to be lost while capturing as many as possible within the spectral spread accepted by the middle junction. Similarly, for the dual-junction system, the bottom bandgap is under driven, meaning we can sacrifice some blue light transmission while maintaining high J_{SC}.

In the first design shown in Figure 4.9 a), the transmission efficacy results are presented for a DTIRC made of acrylic plastic with a 2 cm wide and 2 cm tall electrochemical cell with 5% membrane coverage, 100 nm of TiO2 protection layer and 2 nm of IrO_2 OER catalyst. From this figure, it is clear that designing a DTIRC out of acrylic plastic is a poor decision. Acrylic absorbs so many of the higher-energy photons that the current limiting cell switches to the top junction (see Figure 4.10, lens-PEC combination 1). This assertion is supported by, other investigators[96]. If a narrower spectral band could be utilized without sacrificing J_{SC}, then employing a DTIRC might make sense. The rest of this dissertation therefore considers only CPCs that use reflective optics. Another thing that is revealed is that larger PEC chamber designs fare poorly from an optical throughput standpoint because the electrolyte absorbs a significant portion of the infrared radiation. This is shown by looking at the first design shown in Figure 4.9 c). This conclusion is validated by Döscher et al.[97].

In the second design shown in Figure 4.9 a), the transmission efficacy results are shown for a CPC with optically-thick Ag reflective surfaces, MgF_2-coated single layer ARCs optimized for 670 nm light on the air-interfacing portions of the 1 mm thick quartz glass aperture and receivers, a 3 mm wide, 2.1 mm tall electrochemical cell, 5% membrane coverage, 65 nm of TiO2 protection layer and 1 nm of IrO_2 OER catalyst. The design parameters were chosen after trial and error optimization performed by the author. The design of the PEC chamber is identical to the designs shown in Figure 3.9 a). A significantly larger portion of the optical spectrum is transmitted to the cell, and, per Figure 4.10 (see lens-PEC combination 2), now the middle junction limits J_{SC}, though only by a small margin. As with the first design, the electrolyte still absorbs a significant portion of the infrared light, though this is

reduced. What emerges as a remaining problem is that the catalyst and protective layers absorb and reflect a significant portion of the light. This is shown in the second design in Figure 4.9 d). Additionally, reflectivity from the quartz glass window layers becomes problematic outside of the wavelength range accepted by the middle junction, for which the system was optimized, as shown in Figure 4.9 e), design 2. This is due to employing single-layer ARCs; a more complex multilayer ARC could enhance throughput of photons, but was not considered in this analysis.

The third design in Figure 4.9 a) is identical to design 4.9 b), but the imaginary portions of the indices of refraction of the catalyst and protection layers were set to zero, i.e. the catalyst and protection layers do not absorb light. This represents an optimal, if unrealistic scenario to strive towards for those involved in PEC-compatible materials discovery. There still is some reflection from the catalyst/protection layer surface, though it is reduced to the point where less than 6% of the light within the spectral band absorbed by the middle junction of the triple junction cell is lost in transit from the receiver of the lens to the active layers of the PV cell. This can be seen by comparing the third design in Figure 4.9 a) and Figure 4.9 b).

The remaining significant losses for the third design are due to optical absorption in the electrolyte, in Ag lens coating in the CPC, and from the reflections at the electrolyte-facing side of the quartz window at the lens receiver. This is demonstrated by the losses in Figure 4.9 b). The loss in the Ag layers results from the CPC design employing multiple reflections from the lens walls for most rays that pass through the system. Thus, the finite reflectivity of the Ag film absorbs some of this light, especially in the UV/blue portion of the EMR spectrum, where the index of refraction of Ag is low compared to its refractive indices in the infrared spectrum. More complex multilayer coatings could potentially enhance the reflectivity for certain wavelengths and incident angles, but these were not investigated because of the required high broadband reflectivity of the lens walls. Implementing an antireflection coating at the underside of the receiver's quartz glass window was not employed owing to concerns about chemical stability of such a coating when in contact with the anolyte. Polymer coatings would potentially be stable and have the appropriate index of refraction.

4.9 Better Treatment of Gas Bubbles in the Design

As with other studies[48,53,61,73,98], the effects of gas bubbles on the system are neglected in this analysis. Bubbles will scatter light within the electrolyte[99], away from the PV cell. The regime of light scattering in the cell depends on the size of bubbles in the device, which would need to be assessed experimentally. If the ARCs or other surfaces in the PEC chamber are hydrophobic, bubbles will tend to accumulate in the cell over time. Alternatively, the bubbles could be removed using flowed electrolyte[38].

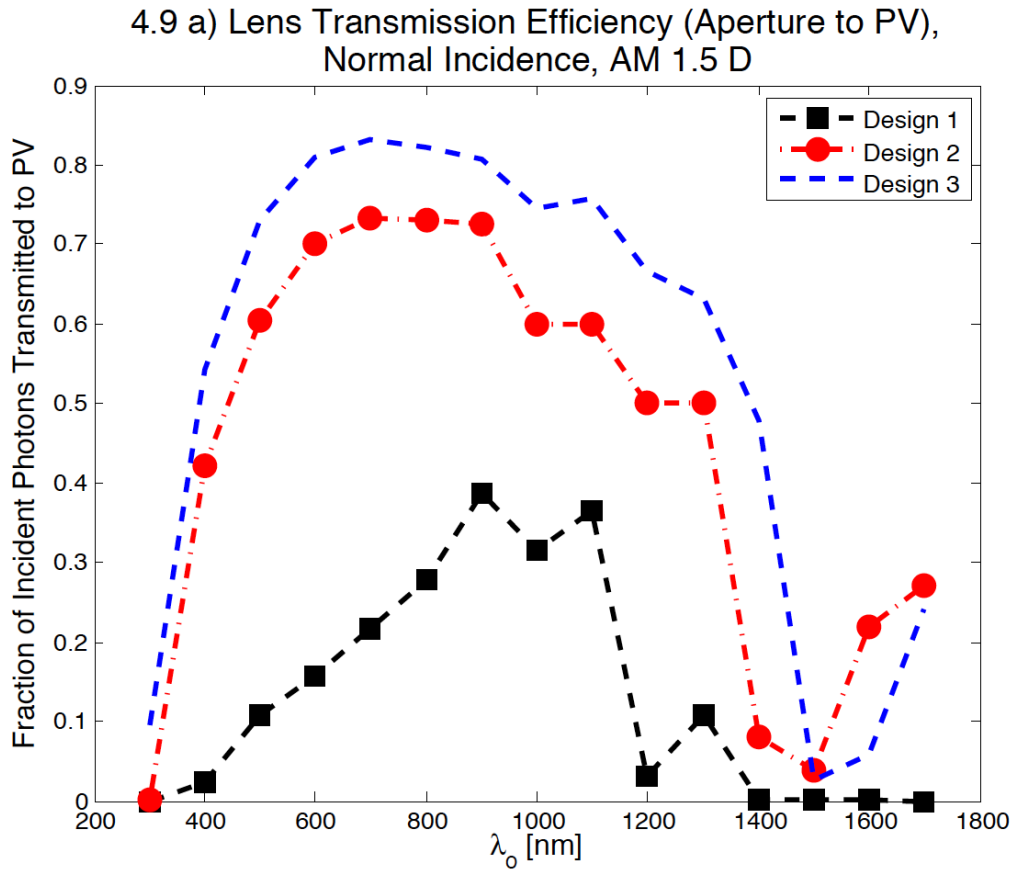
4.9 a) Lens Transmission Efficiency (Aperture to PV), Normal Incidence, AM 1.5 D
Fraction of Incident Photons Transmitted to PV
λo [nm]
Design 1
Design 2
Design 3
0
0.1
0.2
0.3
0.4
0.5
0.6
0.7
0.8
0.9
200
400
600
800
1000
1200
1400
1600
1800

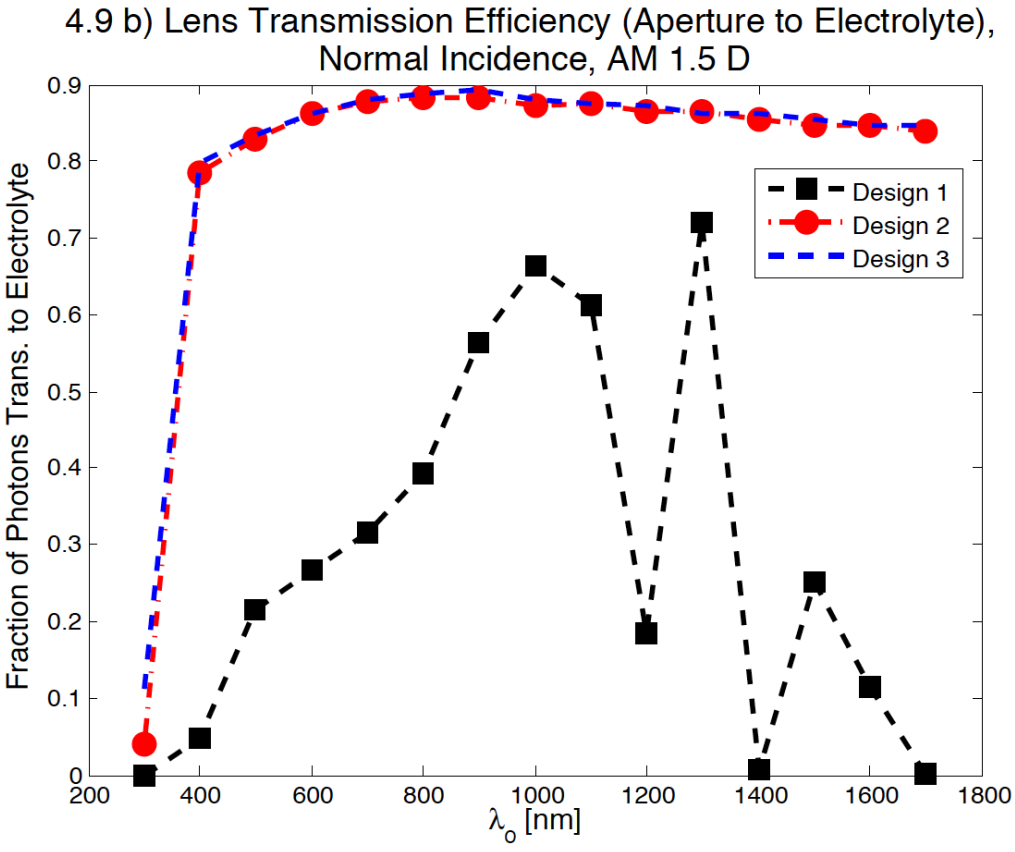
4.9 b) Lens Transmission Efficiency (Aperture to Electrolyte), Normal Incidence, AM 1.5 D
Fraction of Photons Trans. to Electrolyte
λo [nm]
Design 1
Design 2
Design 3
0
0.1
0.2
0.3
0.4
0.5
0.6
0.7
0.8
0.9
200
400
600
800
1000
1200
1400
1600
1800

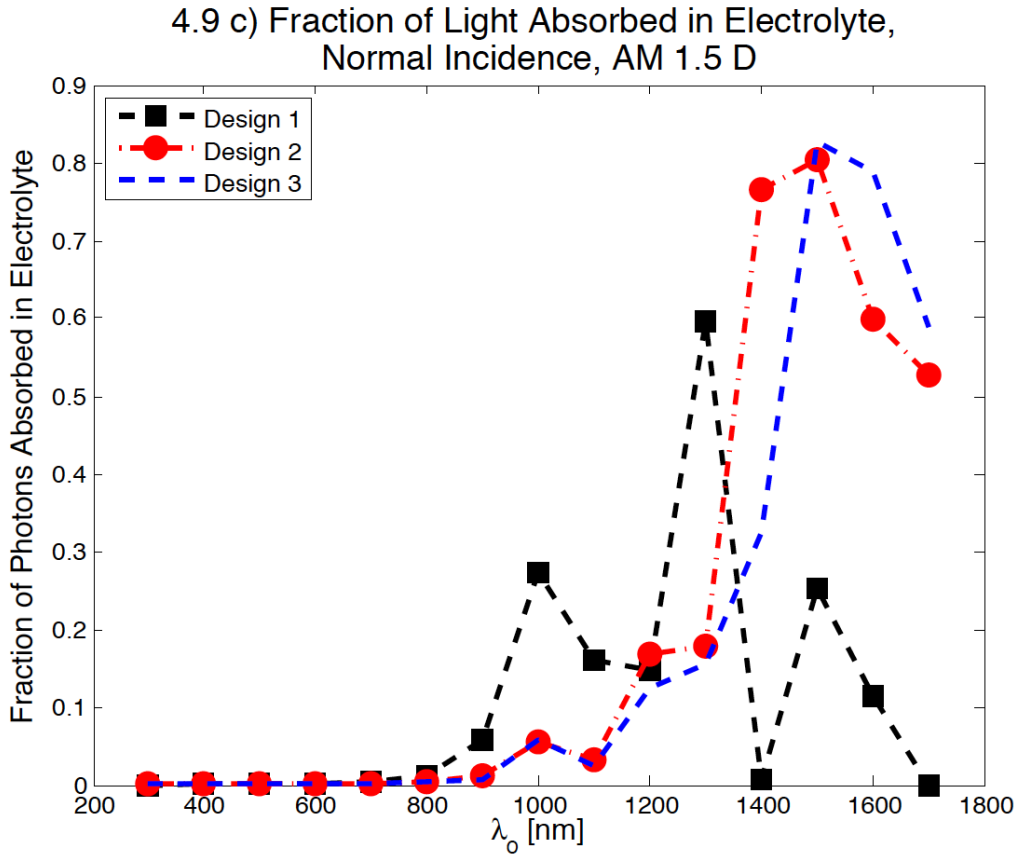
4.9 c) Fraction of Light Absorbed in Electrolyte, Normal Incidence, AM 1.5 D
Design 1
Design 2
Design 3
Fraction of Photons Absorbed in Electrolyte
0
0.1
0.2
0.3
0.4
0.5
0.6
0.7
0.8
0.9
200
400
600
800
1000
1200
1400
1600
1800
λo [nm]

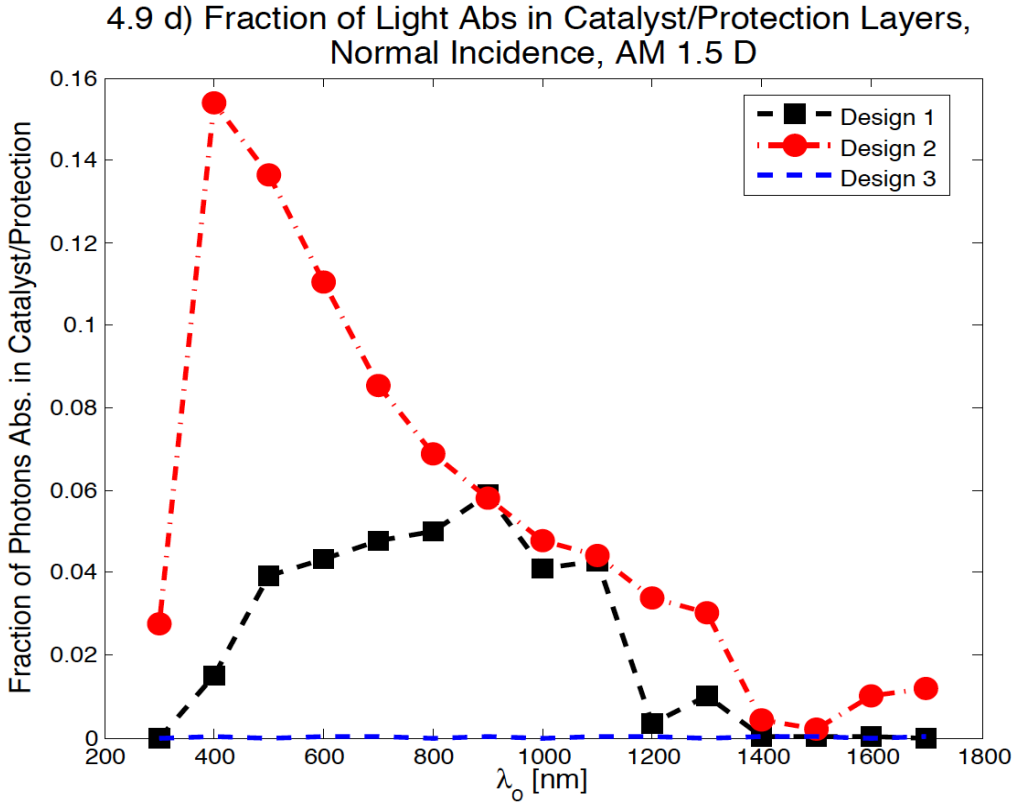
4.9 d) Fraction of Light Abs in Catalyst/Protection Layers, Normal Incidence, AM 1.5 D
Design 1
Design 2
Design 3
Fraction of Photons Abs. in Catalyst/Protection
0
0.02
0.04
0.06
0.08
0.1
0.12
0.14
0.16
200
400
600
800
1000
1200
1400
1600
1800
λo [nm]

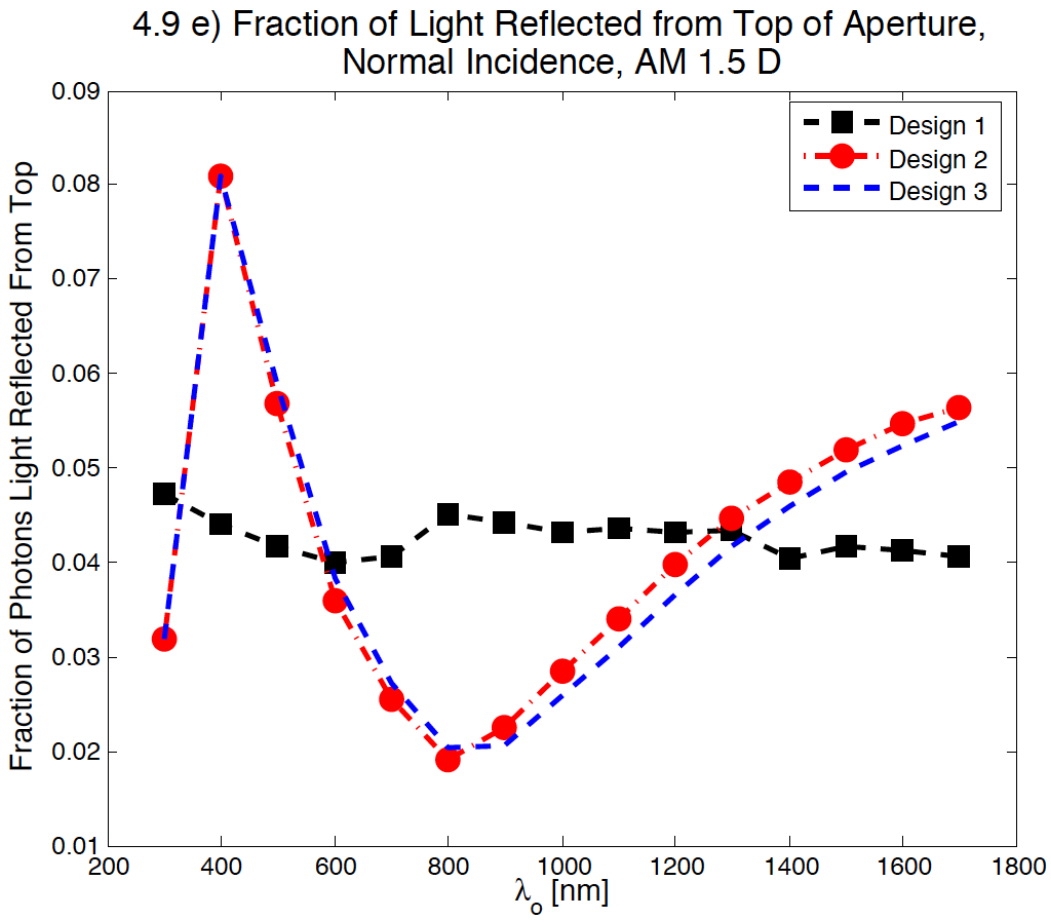

Figure 4.9 a)-d): Lens Transmission and Loss Profiles for Sample Designs

MgF_2	Dodge[100]
Electrolyte (modeled as Water)	pp. 1059-1077, Palik[101]
Ge	pp. 465-478, Palik[102]
GaAs	pp. 429-443, Palik[102]
$Ga_{0.51}InP_{0.49}$	Schubert, Gottschalch and Herzinger[103]
IrO_x	Backholm and Nikhalasson[104]
Pt	Rakic et al.,[106]
TiO_2	Measured by W. Tong (**see Fig. 4.12**)
Membrane (modeled as Nafion)	Zudans, Heineman and Seliskar[107]
Ag	Rakic et al.,[106]
Quartz Glass	Khashan and Nassif[108]
PMMA (Acrylic)	Khashan and Nassif[108]

Table 4.1: Data Sources for Indices of Refraction

For perfrect transmission, AM 1.5 D Spectrum, Normal Incidence

	Jsc, Junction 1	Jsc, Junction 2	Jsc, Junction 3	Jsc, Device	
3 Junction	1,741	1,266	2,544	1,266	A/m^2
2 Junction	2,578	1,303	N/A	1,303	A/m^2

For Lens-PEC Combination 1, AM 1.5 D Spectrum, Normal Incidence

	Jsc, Junction 1	Jsc, Junction 2	Jsc, Junction 3	Jsc, Device	
3 Junction	211	348	433	211	A/m^2
2 Junction	416	444	N/A	416	A/m^2

Percent of Possible Transmission/Jsc Device, Lens 1

	Jsc, Junction 1	Jsc, Junction 2	Jsc, Junction 3	Jsc, Device
3 Junction	12%	27%	17%	17%
2 Junction	16%	34%	N/A	32%

For Lens-PEC Combination 2, AM 1.5 D Spectrum, Normal Incidence

	Jsc, Junction 1	Jsc, Junction 2	Jsc, Junction 3	Jsc, Device	
3 Junction	1,059	925	1,181	925	A/m^2
2 Junction	1,672	870	N/A	870	A/m^2

Percent of Possible Transmission/Jsc Device, Lens 2

	Jsc, Junction 1	Jsc, Junction 2	Jsc, Junction 3	Jsc, Device
3 Junction	61%	73%	46%	73%
2 Junction	65%	67%	N/A	67%

For Lens-PEC Combination 3, AM 1.5 D Spectrum, Normal Incidence

	Jsc, Junction 1	Jsc, Junction 2	Jsc, Junction 3	Jsc, Device	
3 Junction	1,258	1,043	1,385	1,043	A/m^2
2 Junction	1,951	1,018	N/A	1,018	A/m^2

Percent of Possible Transmission/Jsc Device, Lens 3

	Jsc, Junction 1	Jsc, Junction 2	Jsc, Junction 3	Jsc, Device
3 Junction	72%	82%	54%	82%
2 Junction	76%	78%	N/A	78%

Figure 4.10: Effect of Different Designs on Device and Junction jsc, for 10 X Concentration Ratio, AM 1.5 D Spectrum, Normal Incidence

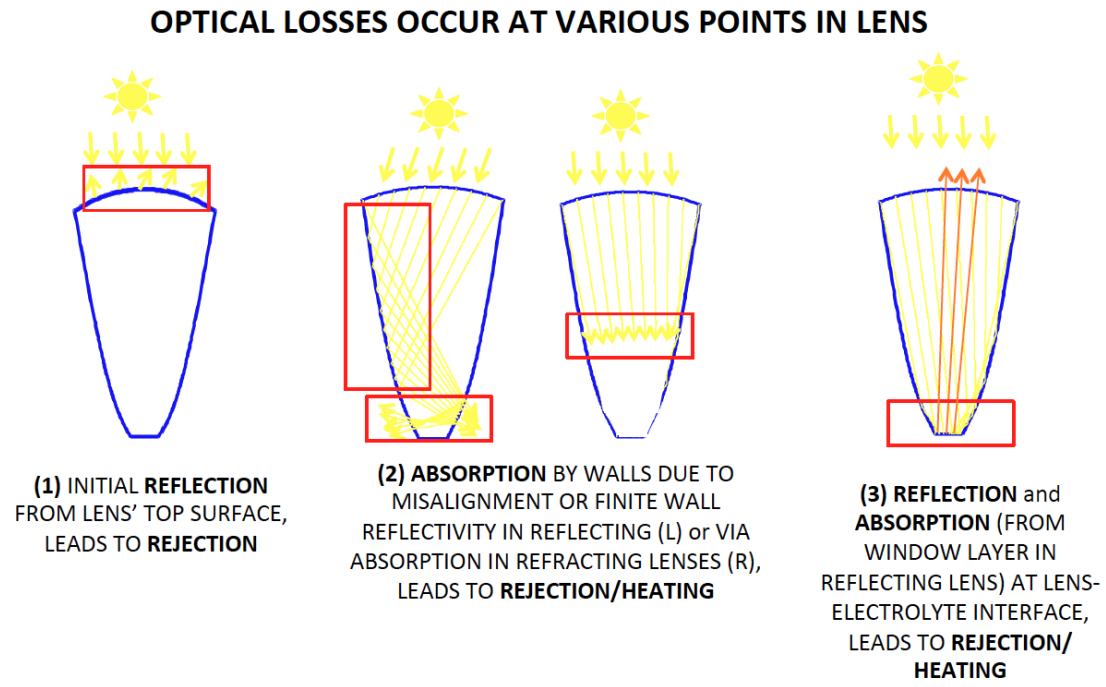

Figure 4.11: Schematic for Point of Optical Loss in Lens and PEC Chamber

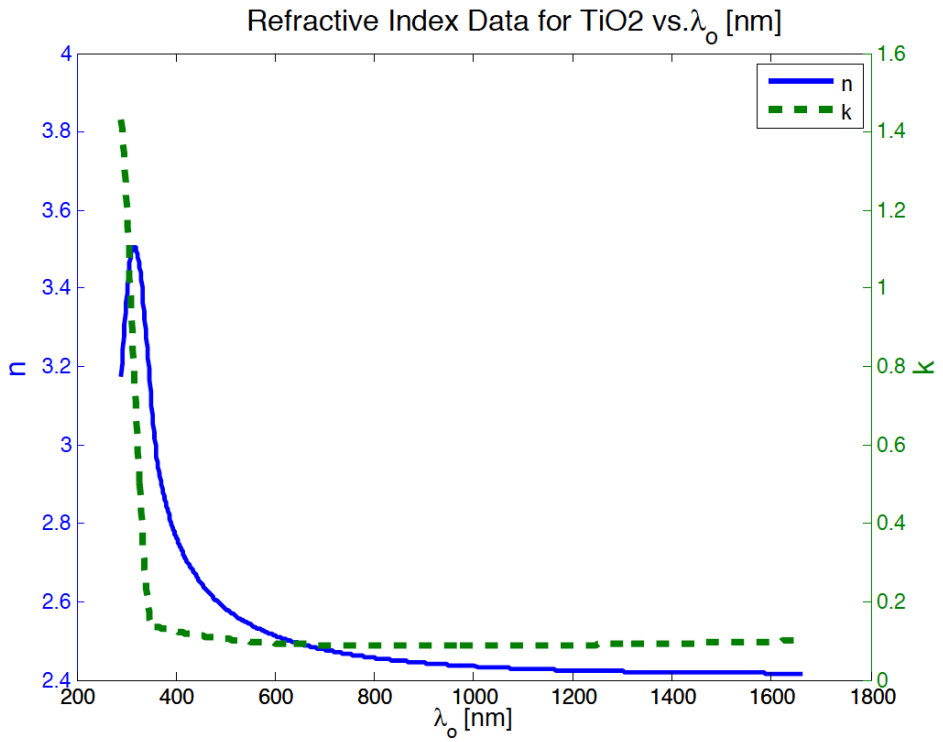

Figure 4.12: Index of Refraction for Protection Layer Measured by Ellispometry. The protection layer was a 30 nm thick TiO_2 sample grown by atomic layer deposition at 250 °C for 300 cycles on Si wafers.

4.10 Conclusions

Moving forward, this analysis will consider the 2nd design presented in Figure 4.9, because it represents a reasonable point from which to make the total assessment of system efficiency and heat transfer. The 3rd design is non-physical, and represents an analysis to determine the remaining sources for optical loss in the system after losses in the catalyst and protection layer are removed, rather than an achievable design. There are improvements that need to be further made in order to improve optical throughput of a wireless, optically concentrating PEC; these will be discussed in more detail in Chapter 7. More detailed transmission data for design 2 is shown in Chapter 6.

Chapter 5: Constructing a Heat Transfer Model for PECs

5.1 Introduction

The primary reason for studying heat transfer in PECs is that design for proper temperature management is necessary to ensure device longevity. As shown in Figure 5.1, the majority of energy that enters a PEC is ultimately converted into heat. Insolation is converted into heat in PECs by absorption of optical energy in the electrolyte and other non-photoactive components of the cell, from the finite efficiency of the PV cell, and from the catalytic overpotential and ohmic losses required to drive the electrochemical fuel-producing reactions at some appreciable rate. This waste heat is ultimately rejected to the surrounds, but the finite rates of heat transfer within the PEC and from the PEC's outer surfaces drive the temperature of the device above the ambient temperature. The different heat generation processes are shown schematically as Figure 5.2.

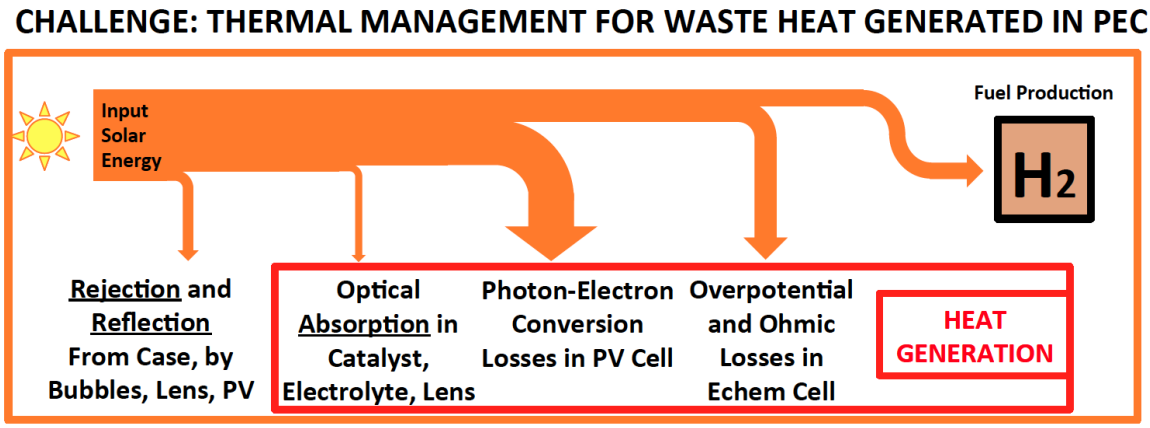

Figure 5.1: Energy Flow in PEC Devices

Constructing the thermal model thus requires a means to quantify the internal, spatially varying heat generation rate in the PEC; the internal and external rates of convective heat transfer in the electrolyte and to the atmosphere, respectively; the external rate of radiative heat transfer; and the ambient temperature; the thermal conductivity, density and heat capacity of the different solid components in the PEC. Ultimately, we must solve a coupled problem wherein the CPEC's η_{STH} is a function of the system temperatures, and the heat generation rates (and, by extension, the system temperatures) are a function of the CPEC's η_{STH}.

In addition to the above considerations, the point of these efforts is to try to develop a model that can predict annual hourly operating profiles of temperature in an arbitrary location. Doing so will require simplifying assumptions in order to engender

OPTICAL LOSSES THAT LEAD TO HEATING OCCUR AT VARIOUS POINTS IN LENS

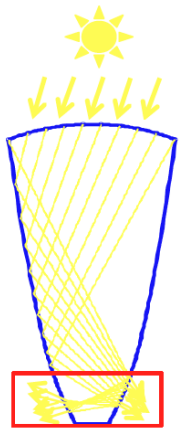

(1) ABSORPTION BY WALLS DUE TO MISALIGNMENT OR FINITE WALL REFLECTIVITY IN REFLECTING LENSES, LEADS TO **REJECTION/HEATING**

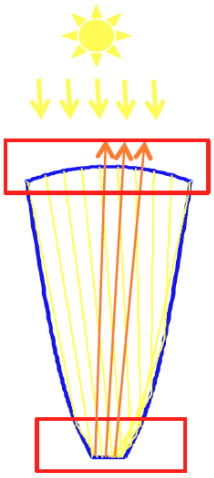

(2) REFLECTION and **ABSORPTION** (FROM WINDOW LAYER IN REFLECTING LENS) AT LENS-ELECTROLYTE INTERFACE, LEADS TO **REJECTION/HEATING**

Q'''OPTICAL: OPTICAL LOSSES OCCUR AT VARIOUS POINTS IN PHOTOELECTROCHEMICAL CELL THAT CAUSE HEATING

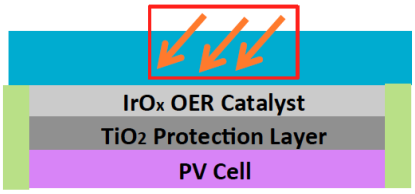

(1) ABSORPTION BY ELECTROLYTE **(HEATING)**

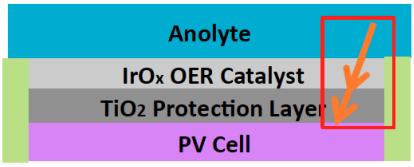

(2) ABSORPTION BY CATALYST AND PROTECTION LAYERS **(HEATING)**

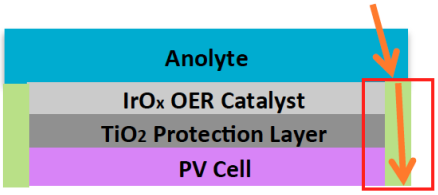

(3) ABSORPTION BY MEMBRANE/ CATHOLYTE **(HEATING)**

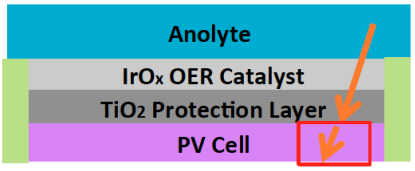

(4) HEATING BY ABSORPTION OF BELOW BANDGAP LIGHT

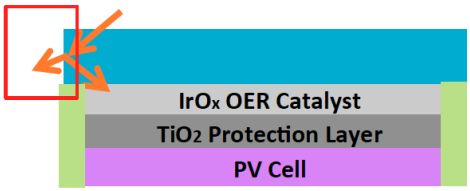

(5) HEATING BY **ABSORPTION** IN PEC CHAMBER WALLS

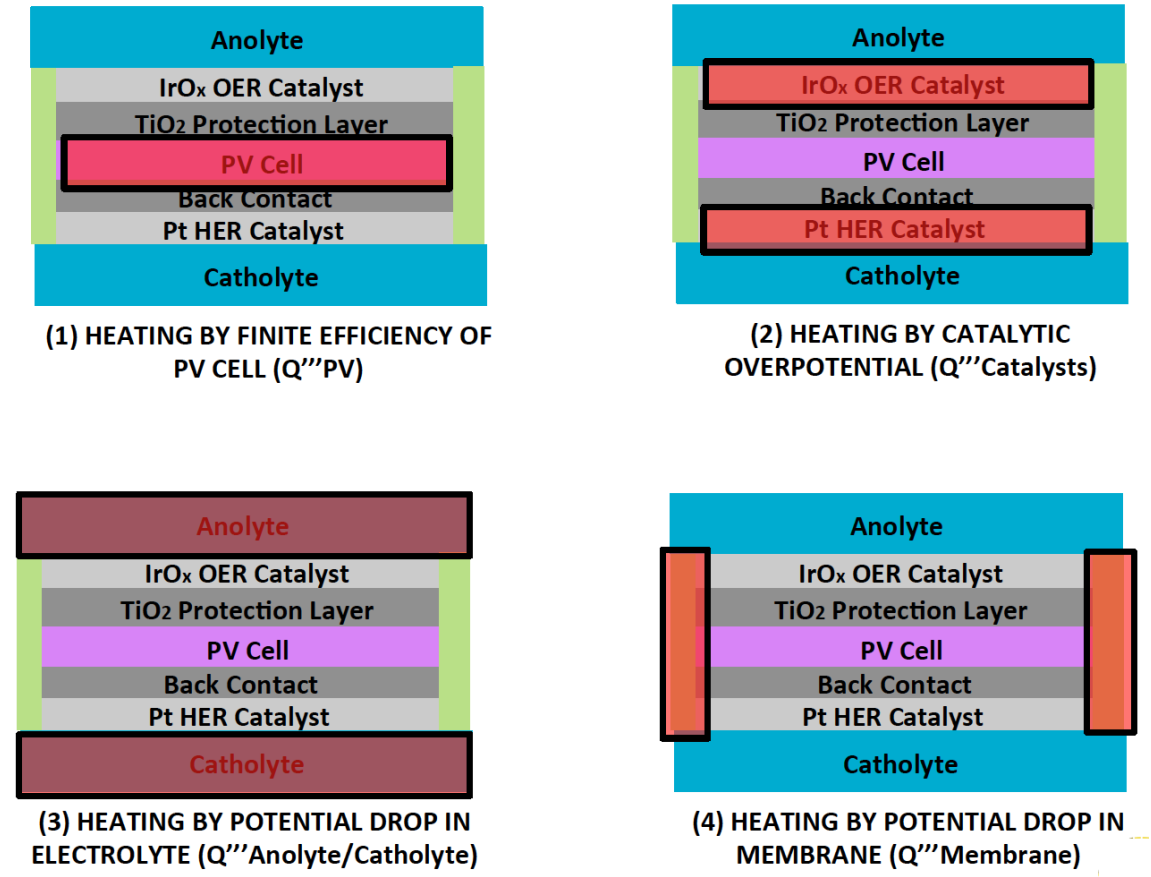

Figure 5.2: Depiction of Heat Generation Locations within PEC/Lens Assembly via Optical and Photoelectrochemical Processes (Not Drawn to Scale)

the model with sufficiently small computational time. These simplifying assumptions, and their drawbacks, are discussed in more detail below.

The study of heat transfer in PECs begins by reviewing some of the relevant literature on the subject of heat transfer in solar energy-harvesting devices. Then, this analysis elaborates on the material contained within this body of literature to provide a mathematical means to quantify sources of heat generation in PECs, quantify the rate of heat transfer to the surrounds, and, finally, to calculate the rate of internal and external transient heat transfer.

5.2 Literature Review of Similar Systems

In Chapter 3, literature that predicted operational PV module temperatures was introduced. Typical non-concentrating solar PV modules operate at 45 - 65 °C, though the ambient conditions and module materials make this a rough estimate (Alonso, García, & Balenzategui, 2004). In Notton et al.(Notton et al., 2005), and Armstrong and Hurley(Armstrong & Hurley, 2010), simple 1-D thermal resistance

network models were constructed to predict the transient operating temperatures of various components in PV cells as a function of insolation, and convective and radiative heat transfer rates to the surrounds. These studies also validated their model results using measured data. The relative computational simplicity of such studies is useful in that it allows for predictions of PV temperatures over long time scales, and thus allows one to estimate typical deployed system performance over its operational lifetime. The work of Rosell et al.(Rosell et al., 2005), extends this type of analysis to a combined PV/thermal collector system with a CR of 11. The simple 1-D transient thermal model allowed for prediction of the fluid temperature exiting the device that was in good agreement with data from an experimental set up that served as the basis for the explored model.

Several studies investigated coupled light, heat transfer and electrochemical phenomena in wired PECs that use solar concentration(Tembhurne, Dumortier, & Haussener 2014; Dumortier & Haussener 2015), and predicted operational temperatures. These use a cooling circuit of electrolyte that also served as the water feed to the integrated electrolyzing cell. The analysis of Dumortier and Haussener (Dumortier & Haussener, 2015) does not account for optical absorption that leads to heating in the electrolyte, however, and the interaction between the device and the ambient temperature is not explored.

5.3 Heat Generation in the PEC

For heat transfer in the solid components in the CPEC, we must solve the heat equation,

$$\frac{dT_i}{dt}\rho_i Cp_i = \nabla \cdot (k_i \nabla \mathrm{T}_i) + \ Q'''_i, \tag{5.1}$$

where $\frac{dT_i}{dt}$ is the rate of change of the temperature of component *i* in the CPEC with respect to time, ρ_i is that component's density, Cp_i is its heat capacity, k_i is its thermal conductivity and Q'''_i is its the volumetric rate of heat generation.

The first term on the right hand side (RHS) of Equation 5.1 can be rewritten by invoking the approximation that we can treat the CPEC elements with a thermal resistance network, as in other works[64]. Thus, we write,

$$\nabla \cdot (k_i \nabla \mathrm{T}_i) = \sum_{j=1}^{n_C} \frac{T_j - T_i}{V_i R_{j\ to\ i}}, \tag{5.2}$$

where the subscript, *j*, gives the coordinate of a component in thermal contact with that of component *i*, n_C is the number of components in thermal contact with component *i*, V_i is the volume of component *i*, and $R_{j\ to\ i}$ is the thermal resistance between each set of components *j* and *i*. Writing Equation 5.1 for each domain, substituting Equation 5.2 in place of the first term on the RHS, and rearranging, we have

$$\frac{dT_i}{dt} = \frac{\sum_{j=1}^{n} \frac{T_j - T_i}{V_i R_{j\,to\,i}} + Q'''_i}{\rho_i C p_i}, \tag{5.3}$$

where the LHS is the rate of change of the temperature of the domain, and the RHS contains the thermal mass of the domain and all the terms relating to the heat transfer in and out of the domain via heat generation, radiation, conduction and convection. Then, to determine the rate of change of temperature for that domain, we can employ an explicit forward Euler scheme. Thus, we solve the equation,

$$T_{i,t+1} = \frac{dT_{i,t}}{dt}\Delta t + T_{i,t}, \tag{5.4}$$

where Δt is the time step, chosen for solution stability and convergence. In the simulations presented herein, Δt =1e-4 s. The next two sections will account for the heat generation term in the various components in the PEC and in the lens material. These terms are depicted in Figure 5.2. Following that, the methodology to calculate the thermal resistances will be discussed.

5.3.1 Heat Generation in the PEC

In order to apply the heat equation to the components of the PEC, one begins by calculating the photoelectrochemically-generated heat sources. The heat generation rate within the PV cell is given by

$$Q'''_{PV} = (1 - Eff_{PV}) I_{PV} A_{Cell} / V_{Cell}, \tag{5.5}$$

where Q'''_{PV} is the volumetric rate of heat generation in the PV cell, I_{PV} is the flux of solar energy incident on the PV cell after it is transmitted through the the catalyst and protection layers, A_{Cell} is the area of the cell that has light incident on it and V_{Cell} is the volume of the PV cell. To determine the PV efficiency, one employs the equation,

$$Eff_{PV} = \frac{j_{OP} V_{OP}}{I_{PV}}, \tag{5.6}$$

where j_{OP} and V_{OP} are determined by the intersection of the j-V curves of the electrochemical and photovoltaic systems, as described in Chapter 3.

The total rate of heat generation in the catalysts layers, $Q'''_{Catalysts}$, due to the kinetic overpotentials is the lumped in with the heat generation in the PV cell. $Q'''_{Catalysts}$ is calculated as

$$Q'''_{Catalysts} = \left(V_{Op} - \mu_{Thermoneutral}\right) j_{OP} A_{Cell} / V_{Cell}. \tag{5.7}$$

The average volumetric heat generation rate in the anolyte/catholyte is given as

$$Q'''_{Anolyte/Catholyte} = \mu_{Anolyte/Catholyte} j_{OP} A_{Cell} / V_{Anolyte/Catholyte}, \quad (5.8)$$

where $\mu_{Anolyte/Catholyte}$ is the potential drop from solution resistance in the anolyte or catholyte (as calculated in Chapter 3 with Equations 3.32-3.34) and $V_{Anolyte/Catholyte}$ is the volume of anolyte or catholyte. Similarly, the heat generation rate in the membrane is

$$Q'''_{Membrane} = \mu_{Membrane} j_{OP} A_{Cell} / V_{Membrane}, \quad (5.9)$$

where $V_{membrane}$ is the volume of the membrane, and $\mu_{Membrane}$ is calculated as shown in Equation 3.35.

5.3.2 Heat Generation due to Optical Absorption

The rate of heat generation in the lens due to the absorption of light is determined using the computational scheme set forth in Chapter 4. Heat generation occurs whenever there is absorption of optical energy in the reflective layers, electrolyte, catalyst, protection layers, chassis and, if present, lens of the PEC. These are shown in Figure 5.2. In particular, significant portions of the infrared and ultraviolet spectrums are absorbed by the electrolyte, chassis and lens, as shown in Chapter 4. Additionally, there is parasitic absorption by the catalyst and protection layers on the PV cell. Generally, the equation for heat generation within a certain element of the cell is given as

$$Q'''_{Optical,i} = 1/V_L \sum_{\lambda_0=0\ nm}^{\lambda_0=\infty\ nm} \alpha(\lambda_0) I(\lambda_0) A_L, \quad (5.10)$$

where $\alpha(\lambda_0)$ is the absorption coefficient of the incident flux within that element, (the calculation methodology of which is described in Chapter 4), $I(\lambda_0)$ is the incident flux intensity (W/m^2), A_L is the area exposed to insolation of that element and V_L is the volume of element. The bounds of the summation are placed by the radiation flux spectrum; in the case of the incident solar spectrum, there is radiation within the bounds of 280 to 4000 nm, whereas that of thermal radiation heat transfer is given by the temperature and emissivity of the involved radiating surfaces.

5.4 Estimating the Thermal Resistances in the CPEC

We need a method for calculating the external and internal heat transfer resistances. This section will go over how to do that in more detail, and will also show how these results compare with more detailed multiphysics models.

5.4.1: Modeling Thermal Radiation Resistance

In order to calculate the sky temperature, combining the work of several investigators[111,112] gives

$$T_{Sky} = (1.24 P_{Vapor}^{\frac{1}{7}} T_{Amb}^{\frac{27}{7}} \left(1 + 0.22 {C_{Frac}}^2\right))^{0.25}, \quad (5.11)$$

where P_{Vapor} is the vapor pressure of water in the ambient air in millibars, T_{Amb} is the ambient dry bulb temperature in degrees Kelvin, and C_{Frac} is the fraction of the sky that is obscured by clouds. Other empirical relations for estimating the sky temperature exist; this was chosen for its ability to capture the effect of cloud cover without knowing the cloud type.

For the PEC depicted in Figure 5.3, given the sky temperature and ambient temperature, the thermal radiative resistance from the top surface of the device to the sky can be calculated approximately as

$$R_{Rad,Top-Sky} = (\varepsilon_{Top} F_{Top-Sky} A_{Top} \sigma_{SB} (T_{Top} + T_{Sky})(T_{Top}^2 + T_{Sky}^2))^{-1}, \quad (5.12)$$

and the thermal radiative resistance from the top surface of the device to the ground is given as

$$R_{Rad,Top-Ground} = (\varepsilon_{Top} F_{Top-Ground} A_{Top} \sigma_{SB} (T_{Top} + T_{Amb})(T_{Top}^2 + T_{Amb}^2))^{-1}, \quad (5.13)$$

where ε is the emissivity of the respective surface, A is the area of the respective surface, σ_{SB} is the Stefan-Boltzmann constant, and $F_{Top-Ground}$ and $F_{Top-Sky}$ are the view factors from the top to the ground and from the top to the sky, respectively. Expressions to calculate the view factors can be found elsewhere[64].

One can construct a similar analysis for the bottom of the CPEC,

$$R_{Rad,Bot-Sky} = (\varepsilon_{Bot} F_{Bot-Sky} A_{Bot} \sigma_{SB} (T_{Bot} + T_{Sky})(T_{Bot}^2 + T_{Sky}^2))^{-1}, \quad (5.14)$$

$$R_{Rad,Bot-Ground} = (\varepsilon_{Bot} F_{Bot-Ground} A_{Bot} \sigma_{SB} (T_{Bot} + T_{Amb})(T_{Bot}^2 + T_{Amb}^2))^{-1}. \quad (5.15)$$

This analysis assumes the top and bottom surfaces are diffuse and gray, and that T_{Top} and T_{Bot} are uniform. The values of emissivity for these surfaces are given as Table 5.1.

There is thermal exchange between the top (aperture) and bottom (receiver) windows in the lens. We ignore conduction through the lens (see below). This internal thermal resistance is given as

$$R_{Receiver\ to\ Aperture} = \left(\frac{1-\varepsilon_{Receiver}}{\varepsilon_{Receiver} A_{Receiver}} + 1/\left(A_{Receiver} F_{Receiver\ to\ Aperture} + \left(\left(\frac{1}{A_{Aperture} F_{Aperture\ to\ Lens}}\right) + \left(\frac{1}{A_{Receiver} F_{Receiver\ to\ Lens}}\right)\right)^{-1} + \frac{1}{A_{Aperture} F_{Aperture\ to\ Receiver}} + \frac{1-\varepsilon_{Aperture}}{\varepsilon_{Aperture} A_{Aperture}}\right) / \left(\sigma_{SB} (T_{Aperture} + T_{Receiver})(T_{Aperture}^2 + T_{Receiver}^2)\right). \quad (5.16)$$

The values for the view factors from the aperture to the receiver and receiver to the aperture can be found in standard heat transfer texts[113]. We assume the lens walls re-radiating surfaces, thus forming a 3-body enclosure with the aperture and receiver. We implicitly assume that there is no additional radiative heat transfer within the CPEC's electrolyte chambers. This is a standard, simplifying treatment in these analyses[64].

[Material]/**(Domain)**	k (W/m-K)	ρ (kg/m^3)	C_p (J/kg-K)	ε	Source
Electrolyte **(11,19)**/ Membrane **(14,16)** [Water]	f(T)	f(T)	f(T)	N/A	Incropera and Dewitt, p. 924[113]
[Air] **(3)**	f(T)	f(T)	f(T)	N/A	Incropera and Dewitt, p. 917[113]
PV Cell [Ge] **(15)**	580	5500	310	N/A	Okhotin[114]
Heat Sink **(10,12,13,17,18, 20,22,23,24)** [Stainless Steel]	15.1	8055	480	0.93	Incropera and Dewitt, p. 907[113]
Heat Sink Sides **(21,25)** [Carbon Steel]	60.5	7854	60.5	0.93	Incropera and Dewitt p. 907[113]
Aperture and Receiver **(1,5,6,7)** [Soda Lime Glass]	1.4	2500	750	0.925	Incropera and Dewitt p. 915/p. 930[113]
Gasket **(8,9)** [Rubber]	0.13	1100	2010	N/A	Incropera and Dewitt p. 915[113]
Lens Material (**2,4**) [PMMA]	0.209	119	1500	N/A	(LuciteLux[115]; Evonik Industries[116]; Cadillac Plastic[117])

Table 5.1: Thermophysical Properties of Elements Used in COMSOL and Author's Simulations. See Figure 5.4 for Location of Domains

5.4.2: Modeling Thermal Convective Resistance

The external rate of convection is determined by the regime of heat transfer, which is given by the ratio of the Reynolds (Re) to the Grashof (Gr) numbers in the air just above and below the device. Re is given as

$$Re = V_{Wind} L_{Wind} / \nu_{Air}(T_{Film,i}), \quad (5.17)$$

where V_{Wind} is the wind speed, L_{Wind} is the length of the CPEC module in the direction of airflow and $\nu_{Air}(T_{Film,i})$ is the kinematic viscosity of air at a given film temperature (the average temperature of the top or bottom surface and the ambient). Gr is calculated as,

$$Gr = g\beta_{Air}(T_{Film,i})(T_i - T_{Amb})L_{Char}^3/\nu_{Air}^2(T_{Film,i}), \tag{5.18}$$

where g is the gravitational constant, β_{Air} is the thermal expansion coefficient of air at a given film temperature, T_i is the temperature of the top or bottom surface and L_{Char} is the characteristic length of the top or bottom surface,

$$L_{Char} = \frac{A_{Aperture}}{P_{Aperture}}, \tag{5.19}$$

where $P_{Aperture}$ is the perimeter of the aperture of the CPEC. If $Gr^2/Re^2 << 1$, forced convection dominates. If $Gr^2/Re^2 >> 1$, natural convection dominates, and otherwise, mixed convection is present. For the mixed convection regime, the maximum of the natural and forced convection coefficient is used, though other conventions exist[63].

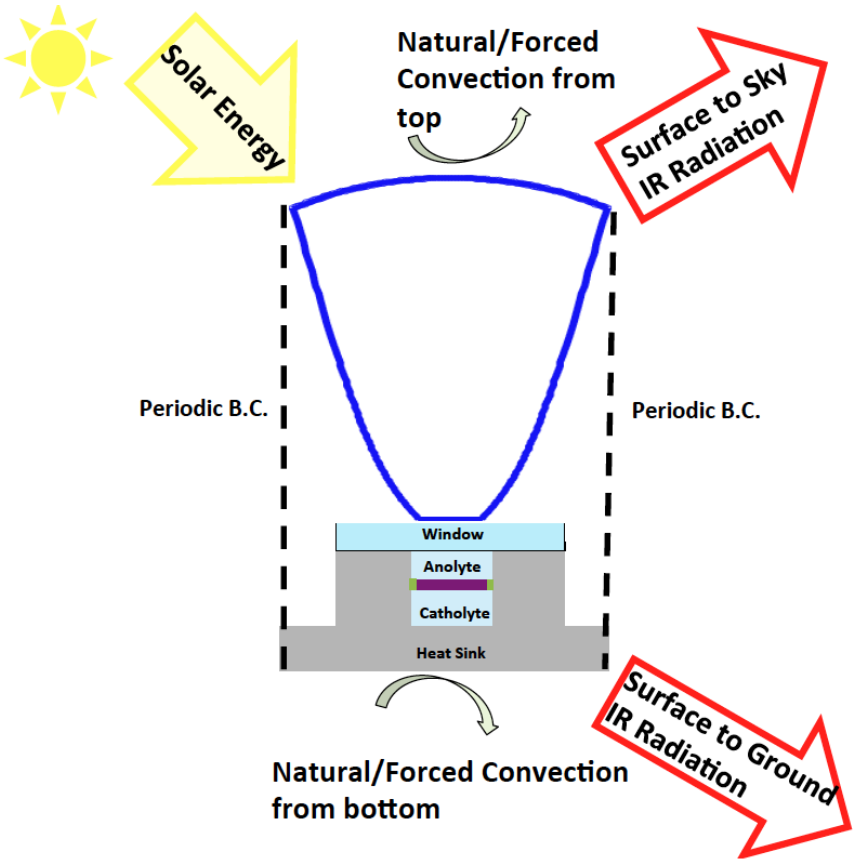

Figure 5.3: Depiction of General Heat Transfer Processes Occurring from Exterior of Integrated Lens/PEC System

The relations used in this work for calculating the convective heat transfer coefficient in the natural and forced convection regimes are summarized in Table 5.2. Though well-known relations exist to determine forced convection on flat plates[113], these generally underestimate the convection coefficients because of the greater turbulence in outdoor environments than that used to develop the more well-known relations[118]. Fortunately, there exist numerous studies that have empirically derived forced convection coefficients from the surfaces of PV modules and buildings[118–122]. The applicability of any given study to a modeling effort is highly dependent on how closely the experimental conditions of the empirically-derived values matches the modeled system. Due to the variance in different studies for the forced convection relations, we chose values from Sparrow and Tien[120] and Sharples and Charlesworth[119] as lower and upper bounds, respectively. The sensitivity analysis resulting from varying the forced convection coefficients is discussed in Chapter 6.

To calculate the thermal resistance to exterior convection from surface *i*, one first calculates the convective heat transfer coefficient using the surface-averaged Nusselt number ($\overline{Nu}_i$),

$$h_{Conv,i} = \frac{\overline{Nu}_i \, K_{Air}(T_{Film,i})}{L_{Char,i}}, \tag{5.20}$$

where $K_{Air}(T_{Film,i})$ is the conductivity of air at the film temperature of surface *i*, and $L_{Char,i}$ is the characteristic length of surface *i* used to derive the relation for $\overline{Nu}_i$ (see Table 5.3). The relations utilized for forced convection give $h_{Conv,i}$ without first having to calculate Nu_i. Then, we calculate the thermal resistance as

$$R_{Conv,i-Fluid} = \frac{1}{h_{Conv,i}A_i}. \tag{5.21}$$

5.4.3: Modeling Thermal Conductive Resistance

In the electrolyte in the PEC, it is assumed that heat transfer is via conduction only. This simplifying assumption is validated below. Because of this assumption, we implicitly ignore the effect of product gas on the electrolyte's thermal and electrical conductivity, as well as light capture. The validity of this assumption will be further addressed below. Thus, for the electrolyte and all other solid components, one calculates the thermal resistance as

$$R_{Cond,i} = \frac{L_i}{k_i(T_i)A_i}, \tag{5.22}$$

where L_i is the length of the component *i* that is parallel to the direction of heat conduction, and A_i is the cross sectional area of component *i* whose surface normal is parallel to the direction of heat conduction. In formulating a network of thermal resistances, it is assumed that heat generation can be represented by a point source

at the center of each domain; otherwise, we cannot invoke the thermal resistance network approximation.

RELATIONS FOR NATURAL CONVECTION

Condition	θ_{Tilt}Range (0° is Horiz.)	Range Ra/Gr	Relation	Comments	Source
Bottom of Heated Plate/Top of Cooled Plate	30-90°	$Ra_g\cos(90° - \theta_{Tilt}) < 1e5$	Eq. 9.27, g replaced by $g\cos(90° - \theta_{Tilt})$	Isothermal Plate, Nu = $\overline{Nu}$, L_{Char} = Area/ Perimeter	p. 546/p. 550 [113]
Bottom of Heated Plate/Top of Cooled Plate	0-90°	$1e5 < Ra_g\cos(90 - \theta_{Tilt}) < 1e11$	Eq. 4	Nu = $\overline{Nu}$, L_{Char} = A/P	[123]
Bottom of Heated Plate/Top of Cooled Plate	0-30°	$Ra_g\cos(90° - \theta_{Tilt}) \leq 1e5$	$\overline{Nu}$ = 0	No convection	N/A
Bottom of Heated Plate/Top of Cooled Plate	0-90°	$Ra_g\cos(90° - \theta_{Tilt}) \geq 1e11$	Eq. 4, $Ra_g\cos(90° \theta_{Tilt}) = 1e11$	Set to max Ra value to extrapolate, Nu = $\overline{Nu}$, L_{Char} = A/P	[123]
Top of Heated Plate/Bottom of Cooled Plate	15-30°	$1.2e3 > Gr_g\cos(90° - \theta_{Tilt}) < 2e6$	Leftmost Equation in Fig. 6	Equation integrated to give $\overline{Nu}$, L_{Char} = Length Along Airflow	[124]
Top of Heated Plate/Bottom of Cooled Plate	15-30°	$Gr_g\cos(90° - \theta_{Tilt}) \geq 2e6$	Leftmost Equation in Fig. 6, $Gr_g\cos(90° \theta_{Tilt})$=2e6	Set to max Gr value to extrapolate. Equation integrated to give $\overline{Nu}$, L_{Char} = L_{Flow}	[124]
Top of Heated Plate/Bottom of Cooled Plate	15-30°	$Gr_g\cos(90° - \theta_{Tilt}) \leq 1.2e3$	$\overline{Nu}$ =0	No convection	N/A
Top of Heated Plate/Bottom of Cooled Plate	30-90°	$Gr_g\cos(90° - \theta_{Tilt}) \leq 3e6$	Second from Left in Fig. 6	Equation integrated to give $\overline{Nu}$, L_{Char} = L_{Flow}	[124]
Top of Heated Plate/Bottom of Cooled Plate	15-75°	$3e6 \leq Gr_g\cos(90° - \theta_{Tilt}) \leq 6e10$	Eq. 9	Gr_C given by values in [63] Nu = $\overline{Nu}$, L_{Char} = A/P	[63,123]
Top of Heated Plate/Bottom of Cooled Plate	All other conditions	All other conditions	$\overline{Nu}$ = 0	No Convection Relation is Reasonable	N/A

RELATIONS FOR FORCED CONVECTION

Condition	θ_{Tilt}Range (0° is Horiz.)	Range Ra/Gr	Relation	Comments	Source
Forced Convection Lower Bound	All	All	Eq. 6		120
Forced Convection Upper Bound	All	All	Those in Table 1	Wind direction is calculated to choose proper relation.	119

Table 5.2: Summary of Forced and Natural Convection Coefficients Used in Model

5.5 Agreement Between Author's Program and COMSOL Modeling Results

5.5.1 Validation of the Conduction Approximation for Heat Transfer in the Electrolyte

In order to be able to simulate a full year's worth of operation, we employed a simplified thermal resistance network, which reduces computation time. To test whether or not this simplification significantly impacted results, the author's program was compared to two simulations generated with COMSOL[125]. One of the

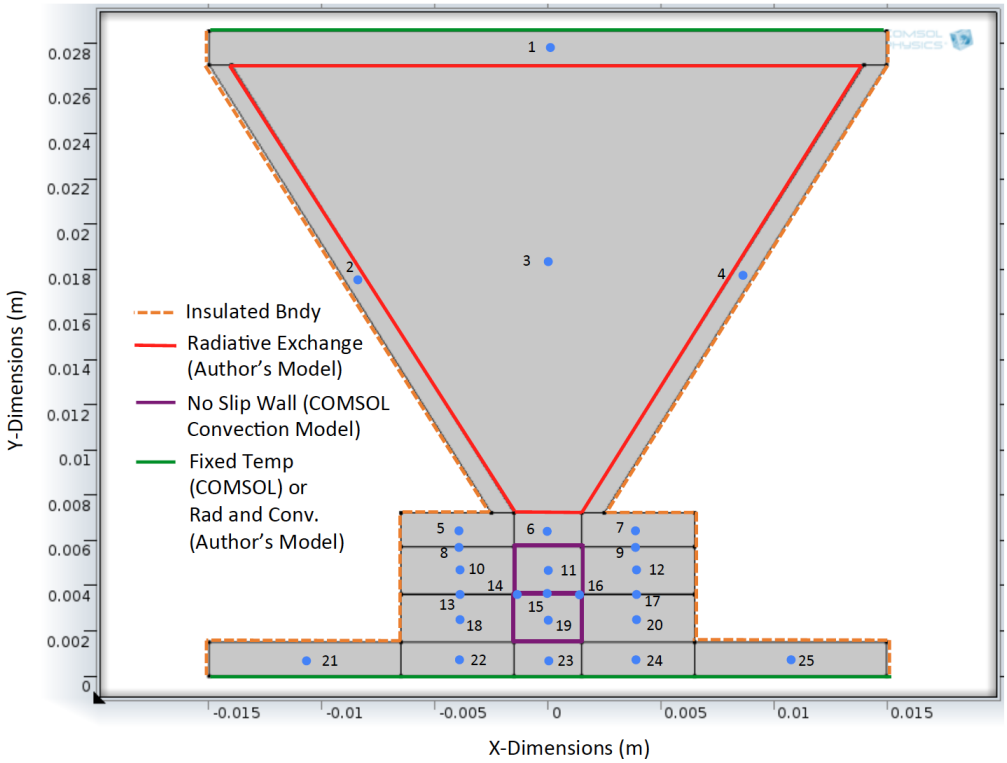

Figure 5.4: Depiction of Domains in COMSOL and Author's Models, as well as Boundary Conditions

COMSOL simulations modeled natural convection in the electrolyte, and the other treated the electrolyte as a solid with the thermophysical properties of water. In all models, the thermophysical properties of the water and ambient air were functions of temperature. The properties of all other domains were set as constants, using data measured at or close to 300 K. The values and data sources for the thermophysical properties of the materials used in the simulation are given in Table 5.1, and the domains to which they are assigned in the models are shown in Figure 5.4.

In the COMSOL modeling, the device is assumed to be oriented horizontally (at a tilt angle of 0° with respect to the ground), and the convection is analyzed in a 2D cross-section of the device's electrolyte chambers. The effects of gas generation in the electrolyte are neglected. The lens is approximated as a trapezoid with the height, receiver width and aperture width of the lens modeled herein. The system pressure is set to 1 atmosphere at the top of the anolyte and catholyte chambers. The natural internal convection is modeled by solving the following equations for an incompressible fluid with no-slip conditions at the walls of the electrolyte chambers,

$$\rho(\mathbf{u}\cdot\nabla)\mathbf{u} = \nabla\cdot\left[-\rho\mathbf{I} + \mu(\nabla\mathbf{u} + (\nabla\mathbf{u})^{\mathrm{T}}) - \frac{2}{3}\mu(\nabla\cdot\mathbf{u})\mathbf{I}\right] + \boldsymbol{F} \tag{5.23}$$

$$\nabla\cdot(\rho\mathbf{u}) = 0 \tag{5.24}$$

$$\rho\mathrm{Cp}\mathbf{u}\cdot\nabla\mathrm{T} = \nabla\cdot(\mathrm{K}\nabla\mathrm{T}) + \mathrm{Q} + \mathrm{Q_V} + W, \tag{5.25}$$

where ρ is the fluid density, **u** is the fluid velocity, **I** is the identity matrix, μ is the fluid's dynamic viscosity, **F** are the body forces on the fluid, Q is the heat generation term due to optical absorption and potential loss, $\mathrm{Q_V}$ is the heat generation due to viscous dissipation and W is the useful work done by the system.

Prior to running the COMSOL simulations, the author's program was run for Barstow, CA. From these results, data for July 23 at 12:00 PM was chosen because of the high direct insolation (929 W/m^2, or 1.05 suns in the AM 1.5 D Spectrum), and associated rate of heat generation in the cell on that day, which would act as a driver to promote natural convection in the electrolyte compartments of the PEC. The Rayleigh (Ra) number at noon in the anolyte, which is calculated as

$$Ra_{Anolyte} = \frac{gPr_{Anolyte}\left(T_{Film,Anolyte}\right)\beta_{Electrolyte}\left(T_{Film,Anoylte}\right)(T_{PV} - T_{Receiver})H_{Anolyte}^3}{\nu_{Anolyte}^2\left(T_{Film,Anolyte}\right)}, \tag{S.30}$$

is 3,547, which implies there will be laminar internal natural convection[126]. In this relation, $Pr_{Anolyte}$ is the Prandtl number of the anolyte, $\beta_{Electrolyte}$ is the thermal expansion coefficient of the anolyte, $H_{Anolyte}$ is the height of the anolyte chamber (2.1 mm), $\nu_{Anolyte}$ is the kinematic viscosity of the anolyte and $T_{Film,Anolyte}$ is the mean of the PV and receiver window temperatures.

The author's program's results were used to generate uniform Dirichlet temperature boundary conditions for the COMSOL models' top and bottom exterior surfaces, at 335.23 and 335.4 K, respectively. The author's model was also used to calculate the heat generation rates in the different domains of the CPEC. These data are shown in Figure 5.5.

In order to verify whether or not it is reasonable to assume that heat transfer in the electrolyte can be treated as conduction in a solid, we compared the two COMSOL models. From the results for the COMSOL models simulating convection

AGREEMENT BETWEEN MODELS AS ASSESSED FROM DATA FOR 12:00 NOON, JULY 23, BARSTOW

DATA DERIVED FROM AUTHOR'S MODEL

HEAT GENERATION TERMS		
Q Anolyte	3.73	[W]
Q Catholyte	1.94	[W]
Q Bottom Window	0.10	[W]
Q Top Window	0.12	[W]
Q Lens Walls	2.81	[W]
Q Electrolyte Walls	0.41	[W]
Q PV + Q Catalyst	13.72	[W]
Q Membrane	0.12	[W]

BOUNDARY CONDITIONS		
Avg. Temp. Back Heat Exchanger	335.40	[K]
Avg. Temp. Top Window	335.23	[K]

RAYLEIGH NUMBERS IN ANOLYTE AND CATHOLYTE	
Ra Anolyte	3547
Ra Catholyte	-5149

AMBIENT CONDITIONS AND COMSOL CONDUCTION MODEL PREDICTIONS

AMBIENT CONDS		
Ambient Temp.	311.45	[K]
Direct Insolation	929.00	[W/m^2]

FLUX OF HEAT THROUGH TOP AND BOTTOM		
Q Transfer Integral Through Top	0.0012	[W]
Q Transfer Through Bottom	20.294	[W]

DOMAIN-BY-DOMAIN PREDICITIONS OF COMSOL MODELS AND AUTHOR'S MODEL, AND AGREEMENT BETWEEN THEM

Domain	5	6	7	10	11	14	15	16	18	19	20	22	23	24
Author's Program	335.59	337.66	335.82	335.45	339.25	339.31	342.11	339.31	335.42	338.04	335.42	335.38	335.43	335.38
COMSOL Convection Model	335.46	336.22	335.46	335.39	337.41	336.62	338.12	336.62	335.25	336.24	335.25	335.07	335.05	335.07
COMSOL Conduction Model	335.45	336.05	335.45	335.39	337.14	336.52	338.26	336.52	335.25	336.51	335.25	335.07	335.06	335.07
Difference Between COMSOL Models	**0.014**	**0.168**	**0.014**	**0.001**	**0.271**	**0.103**	**-0.140**	**0.103**	**-0.003**	**-0.269**	**-0.003**	**0.002**	**-0.006**	**0.002**
Difference Between Conduction Models	**0.138**	**1.612**	**0.365**	**0.061**	**2.107**	**2.786**	**3.848**	**2.785**	**0.168**	**1.525**	**0.167**	**0.306**	**0.375**	**0.305**

Figure 5.5: Various Data Showing Comparison Between the COMSOL and Author's Models

(Figures 5.6 and 5.7), and conduction (Figure 5.8), one can see that the difference in PV cell temperatures is 0.14 °C (See Figure 5.5). This is a small difference. The reason for this is that, for the anolyte and catholyte chambers, the heat sink material creates a nearly uniform wall temperatures at two and three walls, respectively, and the temperature of these walls are close to that of the PV cell. Specifically, in the COMSOL convection model, the temperature of the PV cell is only 2.73 °C warmer than the lateral chamber wall. As a result, there is little thermally-induced instability in the body forces within the electrolyte. Additionally, in the catholyte, the highest temperatures are seen at the top of the chamber, creating a thermally stable temperature stratification in the electrolyte for this particular device orientation with respect to gravity (reflected by the negative *Ra* for the catholyte chamber).

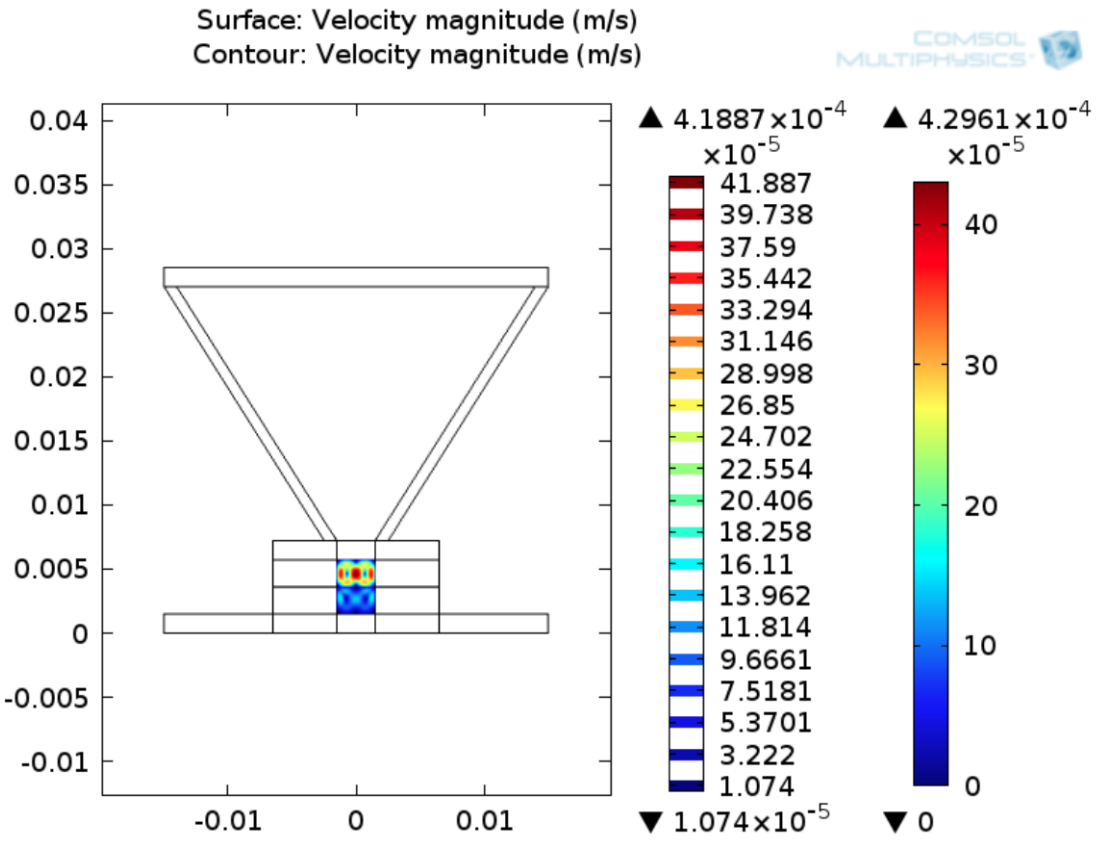

Figure 5.6: Fluid Velocity Profile for Convection Heat Transfer in CPEC

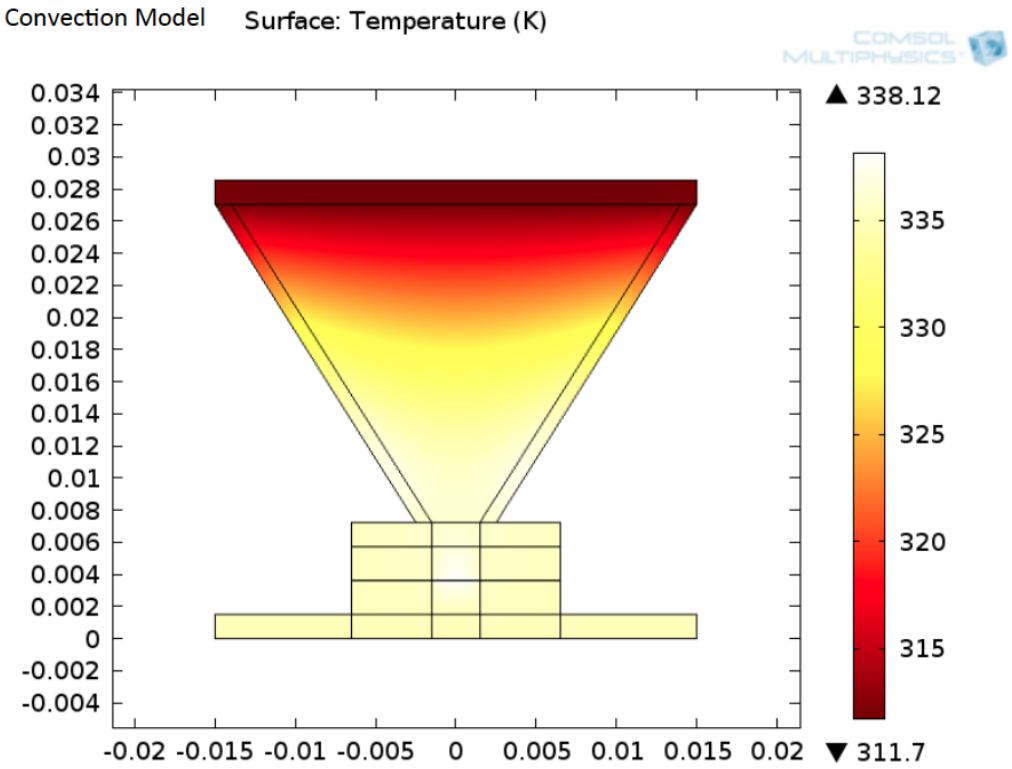

Figure 5.7: Temperature Profile for CPEC, Convection Heat Transfer in Electrolyte

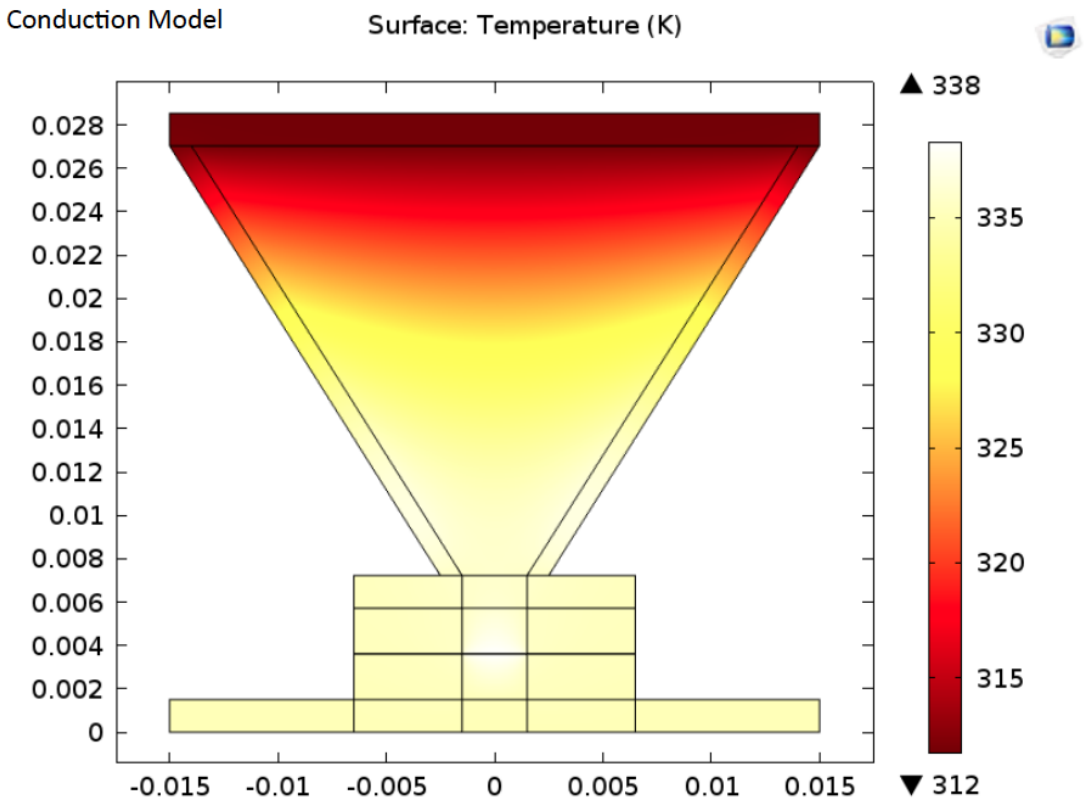

Figure 5.8: Temperature Profile for CPEC, Conduction Heat Transfer in Electrolyte

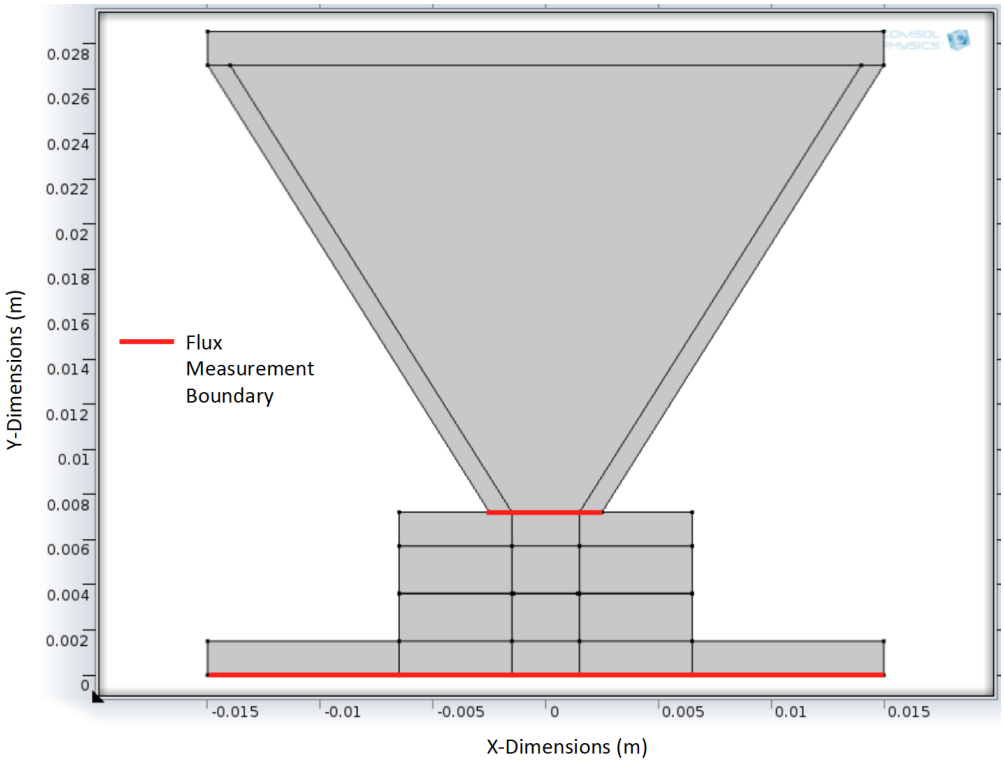

Figure 5.9: Depiction of Where Flux Measurements Were Made to Assess Validity of Ignoring Condition in Lens

Thus, it is reasonable to assume that heat transfer in the electrolyte can be treated as heat conduction in a solid.

Another thing that can be seen from Figure 5.5 is that the rate of heat transfer through the top surface of the electrolyte chamber is 5.9e-3% that through the bottom heat sink (see Figure 5.9 for the boundaries over which flux is measured). In the COMSOL simulations, the lens walls are assumed to be constructed of 1 mm thick PMMA and the lens' interior filled with stagnant air. As a result, heat transfer via conduction and convection through the lens to the top surface of the CPEC is ignored in the author's model.

5.6.2 Validation of the Author's Thermal Resistance Model

The agreement between the PEC component temperatures predicted by the COMSOL models and the author's program is not as good as that between the two COMSOL models. The heat sink temperatures are very close, which makes sense given the imposed Dirichlet boundary conditions on the COMSOL model. The temperature of the PV cell is approximately 3.85 °C higher in the author's model than in COMSOL, or an error of 1.14%.

In order to assess the impact of the difference between the COMSOL and author's predicted PV cell temperature on $\eta_{STH,Avg}$, the η_{STH} of the system was modeled as a function of temperature and concentration ratio. This is shown in Figure 5.10. In the simulation used to generate this figure, the CR is varied between 7.5 to 15 for a system with PEC dimensions and lens transmission properties identical to Design 2 shown in Chapter 3 (3mm wide by 2.1 mm tall electrolyte chambers, and 5% Nafion coverage). For each concentration ratio, the temperature is swept from 273.15 K to 373.15 K.

From Chapter 3, recall that lower temperatures increase the ohmic resistance of the membrane and electrolyte, and higher temperatures decrease V_{OC} and V_{MP} of the PV cell. The increase in the potential losses in the electrolyte and membrane at lower temperatures are shown in Figure 5.11. This figure shows a disaggregation of the different potential losses versus temperature for the 10 X system depicted in Figure 5.10. The reduction in V_{OC} and V_{MP} of the PV cell at higher temperatures is also evident in Figure 5.11. Recall from Figures 3.8 c) and 3.8 d) that when the electrochemical system operates at a total potential drop greater than V_{MP}, it operates off of the "plateau" of the j-V curve of the PV cell, and thus it operates below J_{SC}. This causes a reduction in η_{STH}. Thus, operation at above 360 K or below 280 K for the 10 X system modeled herein would be subject to large temperature-dependent variations in efficiency. In Figure 5.10, the monotonic increase in η_{STH} from 280-360 K for the 10 X system is due to the slight increase in J_{SC} with temperature, per the relations[57] given in Chapter 3.

From Figure 5.10, for a 3.85 °C difference in predicted operating temperature of the PV cell between the COMSOL and author's models, the η_{STH} varies approximately 0.043%. This rate of efficiency variation at full sun holds from approximately 280 K to 360 K, in which η_{STH} varies from 12.01%-12.9%. Thus, the inaccuracy in temperature that results from the author's use of a simple resistor model has a very small impact on the predicted values of η_{STH} throughout the

majority of the CPEC's operating temperature range. This is validated by annual models of system operation presented in Chapter 6.

For the 15 X system, the effects of varying CPEC temperature on η_{STH} are far more pronounced, as the PV cell has less reserve voltage to overcome the increased potential drop in the CPEC resulting from the increased J_{OP}. Similarly, a system that was optimized for higher J_{SC} at the expense of V_{OC} (i.e., a tandem junction device) would also exhibit stronger temperature-dependent effects, which was indeed shown elsewhere[73,53].

During the nighttime, the temperature of all the components in the CPEC except for the lens are typically very similar. The coldest CPEC temperatures also generally occur shortly before dawn, well after the sunset. For example, per the results from Chapter 6 for Barstow, CA, the minimum CPEC temperatures occur at 5:00 am on July 19. At this time, the maximum temperature difference in the components in contact with the electrolyte is 0.013°C. As a result, the predictions of the annual minimum electrolyte temperature should not be greatly affected by the choice to model the electrolyte using a thermal resistance network. This is because the because inaccuracies in the heat transfer rates within the PEC associated with using a thermal resistance network rather than a more detailed finite element model have negligible effects after the temperature of the different components in the CPEC have decayed to a roughly constant value over the course of the night.

Clearly, the overall difference between the predicted temperatures in the COMSOL and author's models will vary more or less, depending on the insolation, heat transfer rates to the surrounds and orientation of the device. However, by modeling a period of high solar resource, the agreement between models during periods when the maximum amount of fuel is generated is best assessed, and the overall agreement is fairly close between models. Furthermore, the effect of using this simple thermal resistance network on η_{STH} is quite small.

5.7 Conclusions

The author's simplified 2-D thermal resistor network model has been shown to provide a reasonable approximation of a more complex set of thermal models constructed in COMSOL. As a result, the simulation framework laid forth in Chapters 3-5 will now be employed to show how the variation of different design parameters would affect device performance. Specifically, geographical location and external convection coefficients are investigated to determine their effect on device performance from a η_{STH}, operational temperature and total annual H_2 produced standpoint.

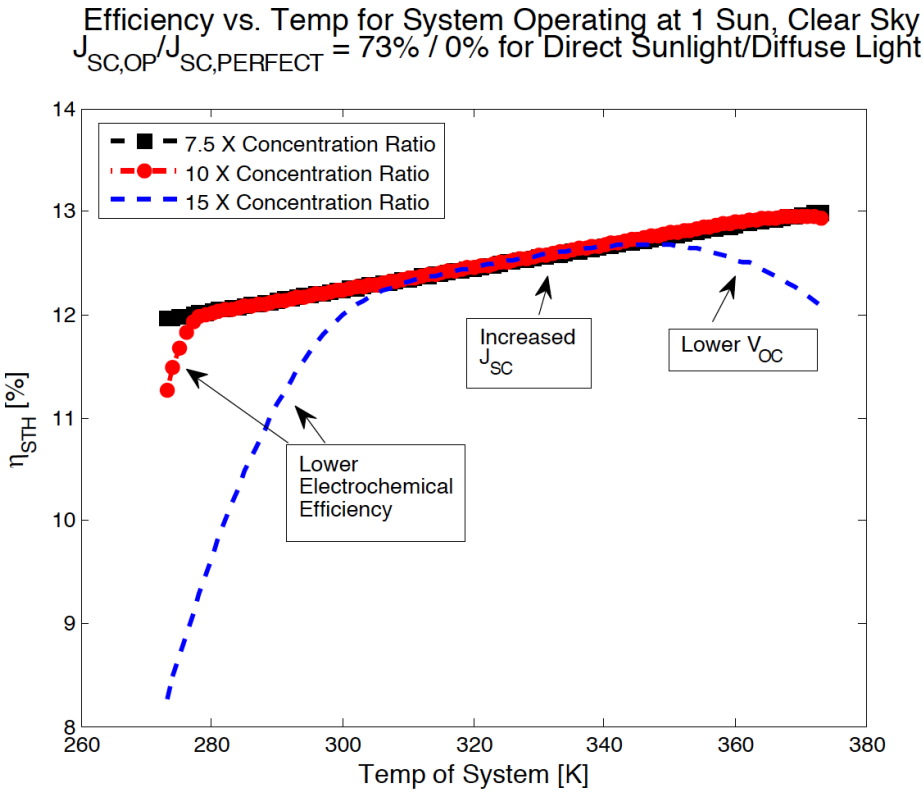

Figure 5.10: Effect of Temperature and CR on η_{STH}

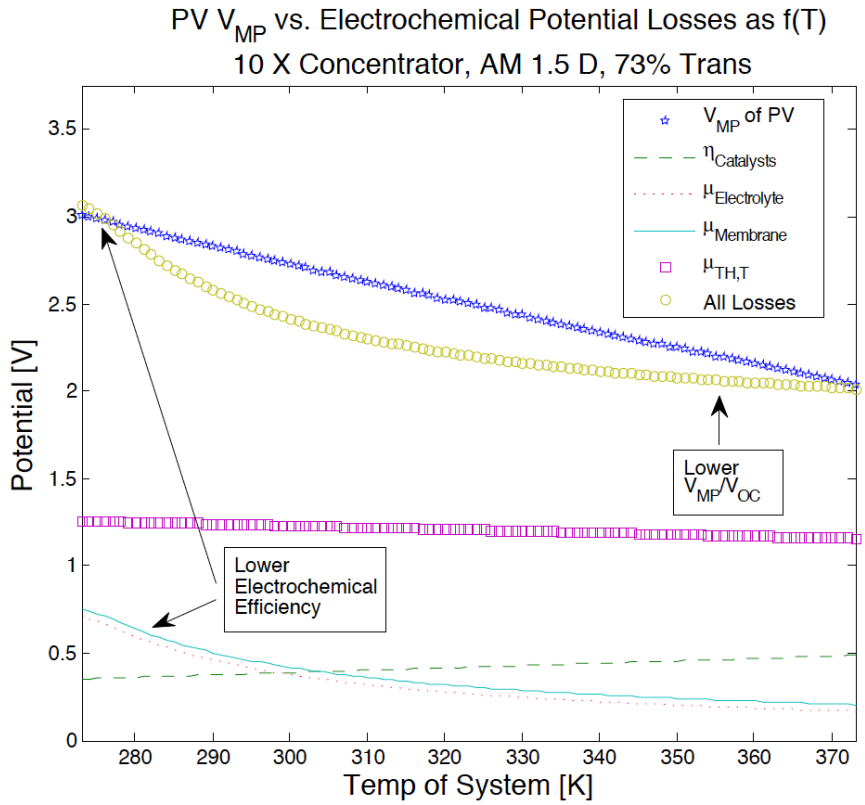

Figure 5.11: Disaggregation of Potential Losses in CPEC at 10 X as f(T)

Chapter 6: Main Findings of Integrated Program

6.1 Introduction

In order to determine the system operation trends predicted by the author's program, the lens detailed in Chapter 4 was used in conjunction with the photoelectrochemical model presented in Chapter 3, and the heat transfer model presented in Chapter 5. A program flow schematic of the integration of these different computational modules is illustrated in Figure 6.1. The results presented below allow the reader to determine what factors affect system efficiency and component temperature, and to gauge the effect of deployment location. This chapter will first present a more detailed set of results of optical behavior for the lens design given in Chapter 4. These will lead to some conclusions about future engineering work that should be performed to manage device temperature.

6.2 Total Program Flow

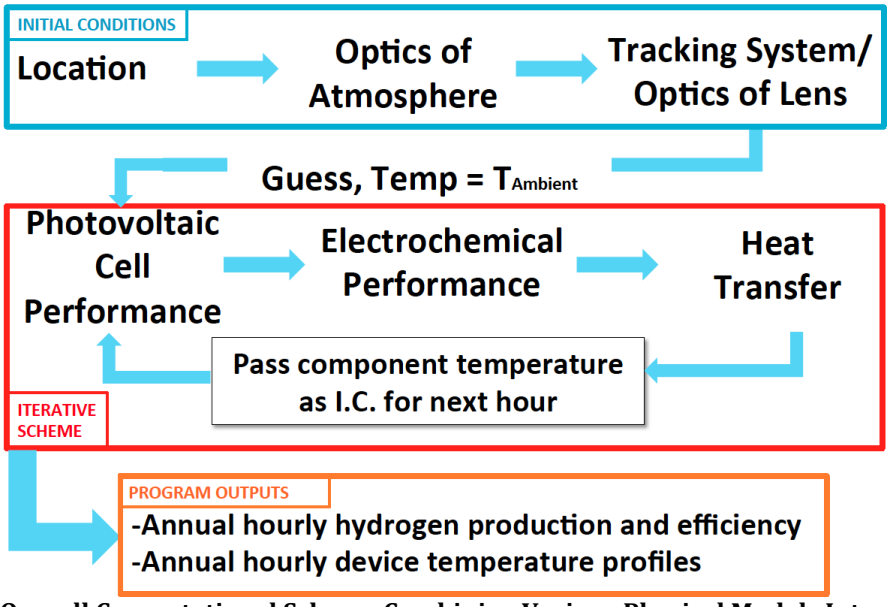

Figure 6.1: Overall Computational Scheme Combining Various Physical Models Introduced in Chapters 3-5

In order to calculate the transient device temperature, H_2 production rates and η_{STH} over the course of a typical year, we begin by choosing a location and system properties (CR, PEC width, membrane width, etc.), then calculate the total time-varying insolation using the weather data for that location using the National Renewable Energy Laboratory's Typical Meteorological Year (TMY) Data[127]. Then, we set the entire device temperature to T_{Amb} for the first hour of the simulation, and, as depicted in Figure 6.1, we calculate j_{HER}, η_{STH} and the waste heat generation

rates given in Equations 5.5 and 5.7-5.9. If there is no captured insolation, these heat generation rates equal zero. Following that, we calculate the temperature for the next hour using the transient heat transfer Equations 5.3 and 5.4. Then, the updated temperature is fed back into the photoelectrochemical efficiency calculation, and so forth, until the last hour of the simulation completes. The entire code is executed in FORTRAN 90 on a personal computer.

6.3 Lens Transmission Behavior

The lens utilized in this study is the second design option presented in Figure 4.9 in Chapter 4. In order to generate profiles of the optical transmission and spatially-varying absorption in the CPEC, simulations were run for the 23 discrete wavelengths (λ_o), so as to balance computational time with simulation accuracy. λ_o is varied between 300 and 2400 nm, which encompasses 99.8% of the total AM 1.5 G irradiance. These discrete values of λ_o were 300, 400, 500, 575, 650, 725, 800, 875, 950, 1025, 1100, 1175, 1250, 1350, 1450, 1550, 1650, 1750, 1850, 1950, 2100, 2250 and 2400 nm. The incident angles over which device performance was measured were ϕ = 0, 15, 30, 45 and 60°, and Θ = 0, 2.625, 5, 5.25 and 10°. The angles ϕ and Θ are respectively the angle that the ray makes about the minor axis of the trough-like lens and the angle that the ray makes about the major axis of the trough-like lens, as depicted in Figure 6.2. The values of θ and Θ were chosen to capture the range of incident angles over which lens transmission would be significant. For $\phi \geq 90°$ and $\Theta \geq 90°$, all energy is rejected from the concentrator. Simulations were run using 2,500 randomly placed rays for each combination of ϕ, Θ and λ_o, and run until the total energy in the simulation was less than $1/500^{th}$ of the original amount at the beginning of the simulation.

For each hour, the array's position is calculated by determining the 2-axis tracking mechanism's position, and the total direct and diffuse resources for this hour are looked up in the TMY database for that particular system's location. Then, the simulation performs 23 discreet simulations at each of λ_o given above. The angle with which direct light contacts the aperture of the lens is calculated, and the appropriate lens transmission and absorption maps are looked up for this particular λ_o. These give the optical transmission to the PV layers, as well as the amount of light absorbed in the electrolyte, lens walls, aperture and receiver, the catalyst and protection layers, and the membrane. If the angle the light makes with the aperture falls between the discreet values of ϕ and Θ given above, the appropriate transmission or absorption value is estimated via bilinear interpolation. For each value of λ_o, the total amount of energy falling within that particular bin of the AM 1.5 spectra can be summed, and multiplied by the respective transmission and absorption values. Thus, the direct light's power is allocated among these various domains. Following that, the diffuse light is simulated by randomly generating 1,000 ray trajectories to simulate isotropic radiation coming from the sky. Each of the incident angles these make on the lens surface is calculated, and the same process is

repeated to calculate how to allocate the diffuse irradiation's power among various domains in the lens, assuming that each diffuse ray has identical irradiance.

Sample transmission and absorption profiles are provided below as Figures 6.3-6.7 From these, it can be determined that only a very small solid angle of light is transmitted into the PV layers, which thus necessitates at least 1-axis tracking. The system is simulated as having 2-axis tracking to further enhance efficiency. This makes sense given the concentration ratio of the device. Outside of this solid angle, most of the light is rejected by or absorbed in the walls of the lens. Additionally, as discussed in Chapter 4, the optical absorption by the electrolyte is quite large in the infrared wavelengths. Other lens transmission and absorption profiles are not shown for brevity.

6.4 Annual System Performance as a Function of Parametric Variation

6.4.1 Overview of Annual Performance Results

In order to simulate device performance across a range of locations, weather data from 4 locations in the TMY dataset were chosen. These were Barstow, CA, which represents a location with extremely good direct solar resource, as well as a hot climate; Albuquerque, NM, which has a good direct solar resource but, owing to its high altitude, a cold winter climate; New Orleans, LA, which has a warm, rainy climate that makes the overall portion of light falling as direct insolation significantly lower than the two desert locations, and Quillayute, WA, which is located in a temperate rainforest, and thus has a very poor direct solar resource. These locations, as well as the direct solar resource, are illustrated in Figure 6.8.

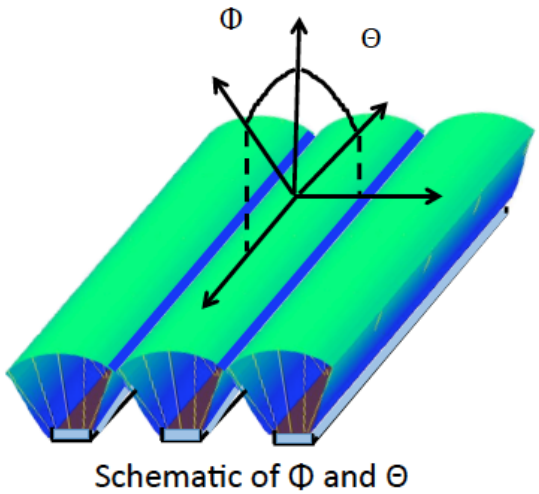

Figure 6.2: Schematic of Angles Used to Quantify Lens Performance

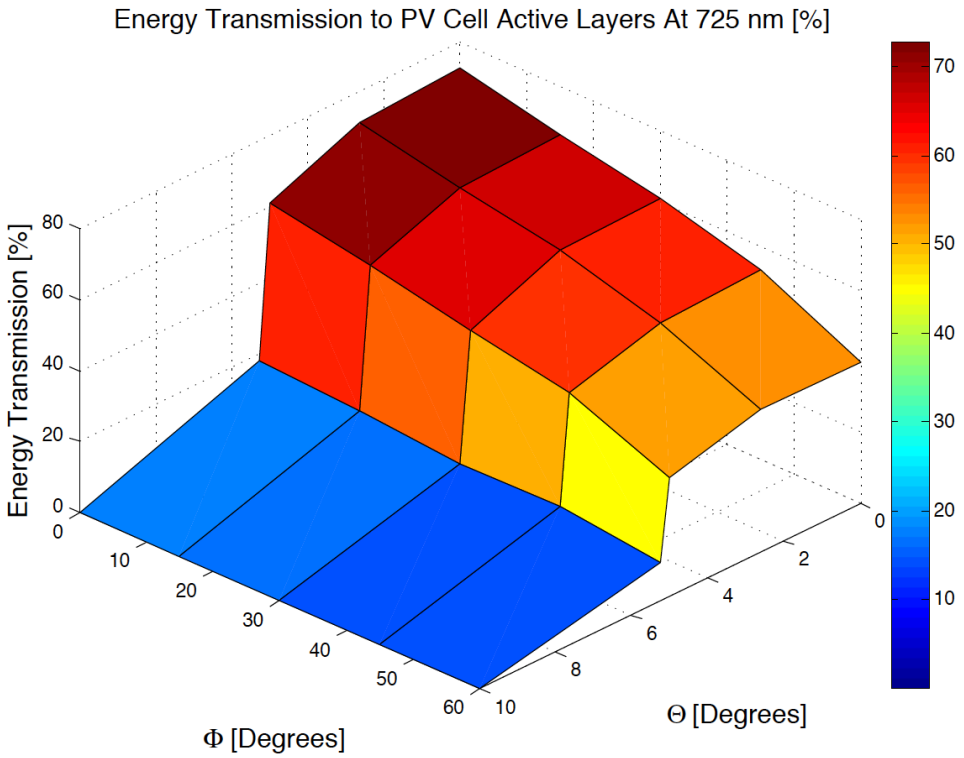

Figure 6.3: Lens Energy Transmission Profile for 725 nm

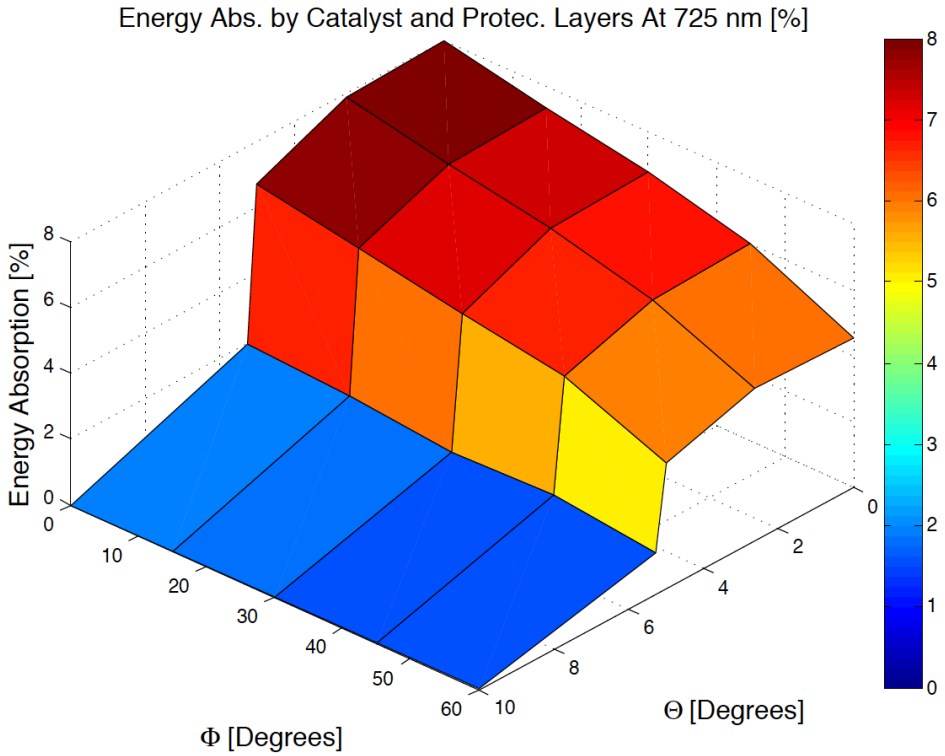

Figure 6.4: Energy Absorbed by Catalyst and Protection Layers at 725 nm

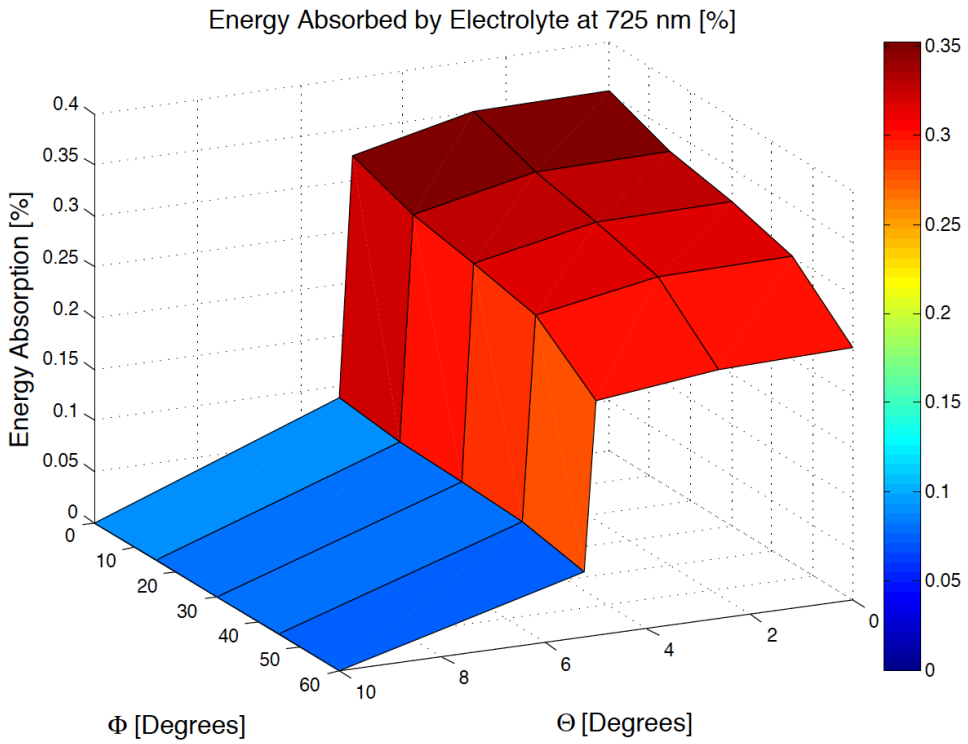

Figure 6.5: Energy Absorbed by Electrolyte at 725 nm, Showing Transmission Window of Water

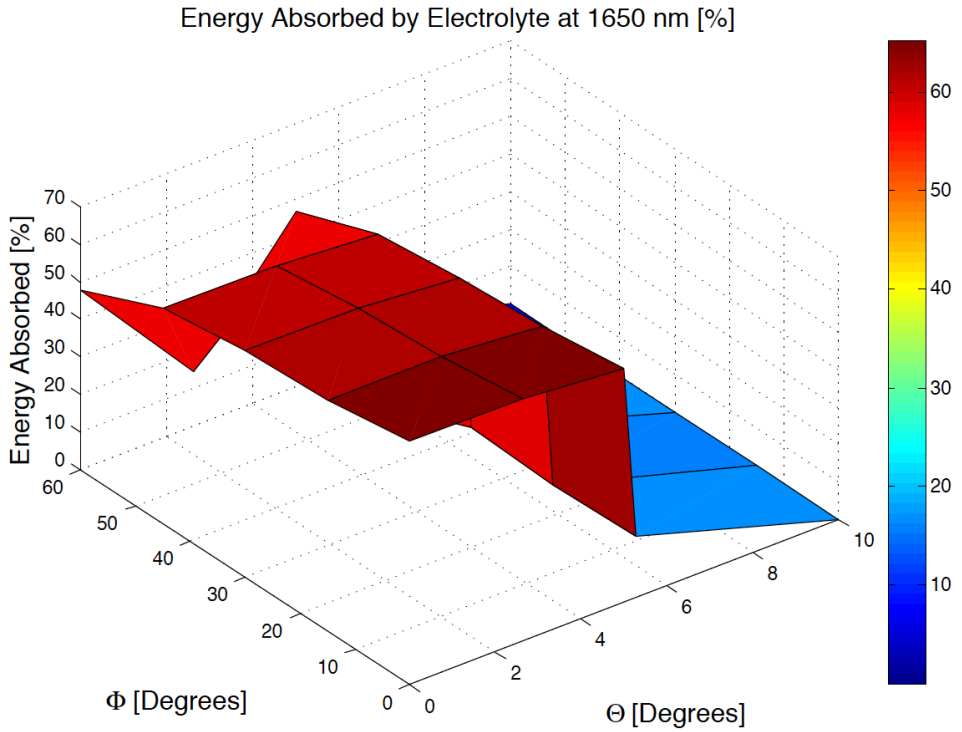

Figure 6.6: Energy Absorbed by Electrolyte at 1650 nm, Showing Opacity of Water

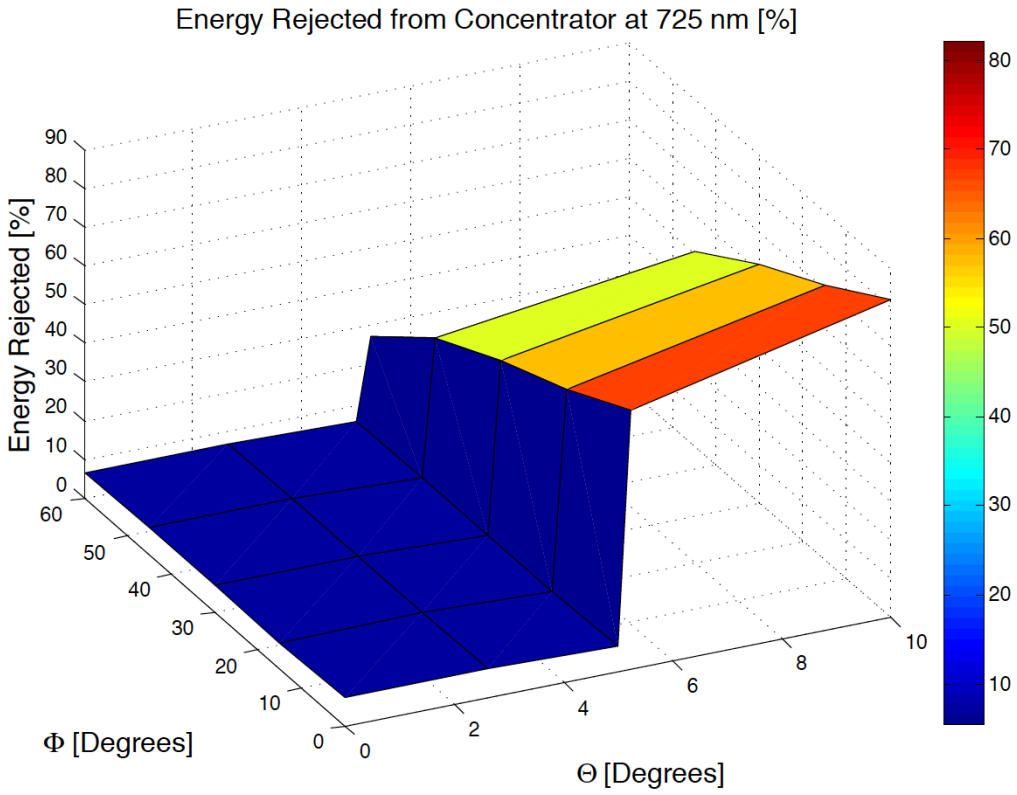

Figure 6.7: Rejection of Light from Concentrator at 725 nm, Showing both Reflectivity within CPEC's Anolyte Chamber and Effect of Acceptance Angle

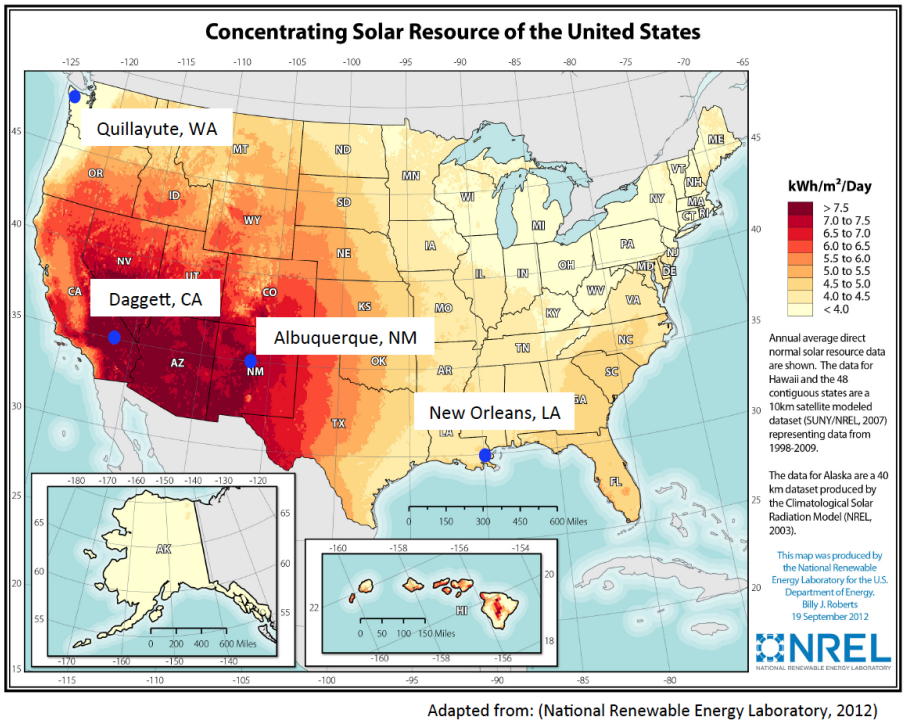

Adapted from: (National Renewable Energy Laboratory, 2012)

Figure 6.8: Map of Direct Solar Resource and Locations of Case Studies

Each device was simulated to be 1 m^2 in overall size (1 m on each side), installed on flat ground with no shading from adjacent arrays, and to have perfect tracking. For conditions when electrolyte temperatures dipped below 0 °C, the electrolyte properties were those at 0 °C, and some implicit pressurization allowed use of saturated liquid water thermophysical properties above 100 °C.

In each location, device performance was simulated over every hour of the year, and the hourly temperature profiles and hydrogen generation rates were calculated. This allows one to determine the number of hours that the average electrolyte temperature is above and below the minimum and maximum estimated safe operational temperature bounds of the device, -4.4 °C and 100 °C, respectively; the average operational temperature throughout the year, the annual produced amount of H_2 per m^2 of aperture (the Specific Fuel Production, or SFP), and the weighted average annual value of η_{STH}. These results are tabulated below in Tables 6.1 and 6.2. The annual weighted average efficiency is given as

$$\eta_{STH,Avg} = \sum_1^{8,760}(\eta_{STH,h} j_{HER,h}) / \sum_1^{8760} j_{HER,h}, \tag{6.1}$$

where $\eta_{STH,h}$ is the η_{STH} at hour h, $j_{HER,h}$ is the current density at hour h, and the bounds of the summation are from the first to the last hour of a non-leap year. The SFP is given as

$$SFP = \frac{1}{yr} \sum_1^{8760} (j_{HER,h}\, \mu_{Thermoneutral} A_{Cell} 3600 \frac{s}{hr} 1\ hr) / (A_{Aperture} \Delta H^0_{H_2O}). \tag{6.2}$$

where $\Delta H^0_{H_2O}$ is the enthalpy of formation of liquid water at standard conditions, or 1.418e8 J/kg

Several trends can be determined from the data presented in Tables 6.1 and 6.2. From the temperature data, it is clear that there are excursions outside of the probable safe operating temperature range for CPECs in all locations, with colder climates predictably having more excursions below -4.4 °C and the hottest climate having the greatest number of excursions above 100 °C.

$\eta_{STH,Avg}$ is 11% or better in Barstow, CA and Albuquerque, NM (locations with good direct solar resource), and declines in areas with lower direct solar insolation resource to 9.1% in Quillayute, WA. These values are well below the instantaneous η_{STH} values modeled by Chen et al.[73], where η_{STH} in excess of 25% were reported for a tandem-junction CPEC with no optical losses, and a trough-like lens with a CR of 10. The effect of varying direct solar resource is clearly evident in the SFP of the CPEC modeled herein, because regions with poor resource have a commensurate drop in annual SFP (ranging from 8.8 kg H_2/m^2-yr in Barstow, to 2.91 kg H_2/m^2-yr in Quillayute). The variation in $\eta_{STH,Avg}$ and the SFP result from the fact that the CPEC is ineffective at capturing diffuse sunlight. This is shown in Fig. 6.3, which shows a transmission profile for the lens at 725 nm, ranging from 73% of energy transmitted from the atmosphere into the PV cell's active layers at

normal incidence, to less than 3.5e-3% at Θ=10°. This transmission profile is a result of the small acceptance angle of the CPC lens.

The effect of varying the forced convection coefficients from that given in Sparrow[120] to that given in Sharples[119] on the total hours of excursion from the safe temperature range, as well as $\eta_{STH,Avg}$, is small. The CPEC only operates one more hour per year above 100 °C with the lower convection coefficient in Barstow, CA, and the change in $\eta_{STH,Avg}$ is less than 0.01%. Similarly, varying the forced convection coefficient from the low to the high bound has only a small effect on the average operating temperature, with a 5.8 °C difference in the average annual operating temperature in Barstow, CA.

The negligible change in $\eta_{STH,Avg}$ as the forced convection relation is varied results from the way in which the CPEC was designed, as discussed in Section 5.6.2 in Chapter 5. The CPEC was designed so that η_{STH} variations would be small for the relevant range of temperatures and captured direct insolation, with a CR of 10. The reason why the number of hours above 100 °C varies only slightly is discussed below.

6.4.2 Typical Operating Temperature Profiles: What are the Important Factors?

In order to elucidate what factors are most influential on the system's operating temperatures over shorter time scales, some hourly data from Barstow, CA was analyzed. The data herein are for the higher forced convection coefficients[119]. The profile for July 19 is shown as Figure 6.9. Several things stand out from this graph. First, the temperature of the PV layer is, logically, the highest within the system when sunlight is being captured by the PV cell, as this is where the majority of heat generation occurs in the device. During typical conditions, 60% of the waste heat is generated in the PV cell and catalysts, 25% is lost due to ohmic drop in the electrolyte (see Figure 5.5 for heat generation profiles under sunny, clear sky conditions), and the great majority of the remaining energy is lost in the lens. Interestingly, the temperature of the PV cell does not track the ambient temperature during the daytime. In fact, what is driving the variation in temperature of the cell during midday is the variation in captured solar flux in the PV cell. This is shown in Figure 6.10, where the variations in hourly temperature of the PV cell line up closely with the transmitted solar resource. Finally, the system quickly adjusts to the ambient and sky temperatures when there is no insolation.

As shown in Figure 6.11, days with extreme high temperature excursions coincide with quiescent ambient conditions. In these figures data from Barstow for July 13 are shown. We find that the electrolyte temperature jumps from typical midday summer operating temperatures to over 108 °C, starting at 2:00 PM. The reason is that, though insolation is declining at this time of day, the wind speed suddenly drops to 0 m/s. Thus, per Fig. 8 b), whereas before forced convection in the range of 12-26 W/m^2K facilitated the removal of heat from the CPEC, the forced convection is replaced by natural convection in the range of 1.5-1.8 W/m^2K. This

	Barstow, Low Conv	Barstow, Hi Conv	Albuquerque	New Orleans	Quillayute
Weighted Average Annual ηSTH [%]	11.2	11.2	11.0	10.0	9.1
Annual kg of H_2 Produced per [sq. m] of Aperture (SFP)	8.79	8.80	7.98	4.85	2.91

Table 6.1: Information Pertaining to Average Annual Device Efficiency

	Barstow, Low Conv	Barstow, Hi Conv	Albuquerque	New Orleans	Quillayute
Annual Hours Below 0 [C], Ambient	85	85	724	45	193
Annual Hours below -4.4 [C], Electrolyte	81	68	425	63	264
Min Temp in Year, Electrolyte [C]	-14.4	-14.3	-19.5	-14.5	-14.2
Annual Hours above 100 [C], Electrolyte	11	12	5	0	0
Max Temp in Year, Electrolyte [C]	107.6	108.3	104.6	93.2	90.3
Avg Operation Temp in Yr (ηSTH>0), Electrolyte [C]	56.3	50.4	21.0	41.0	30.1
Avg Ambient Temp. in Yr [C]	19.7	19.7	13.7	20.4	9.6

Table 6.2: Summarized Results of Annual System Temperature Profiles

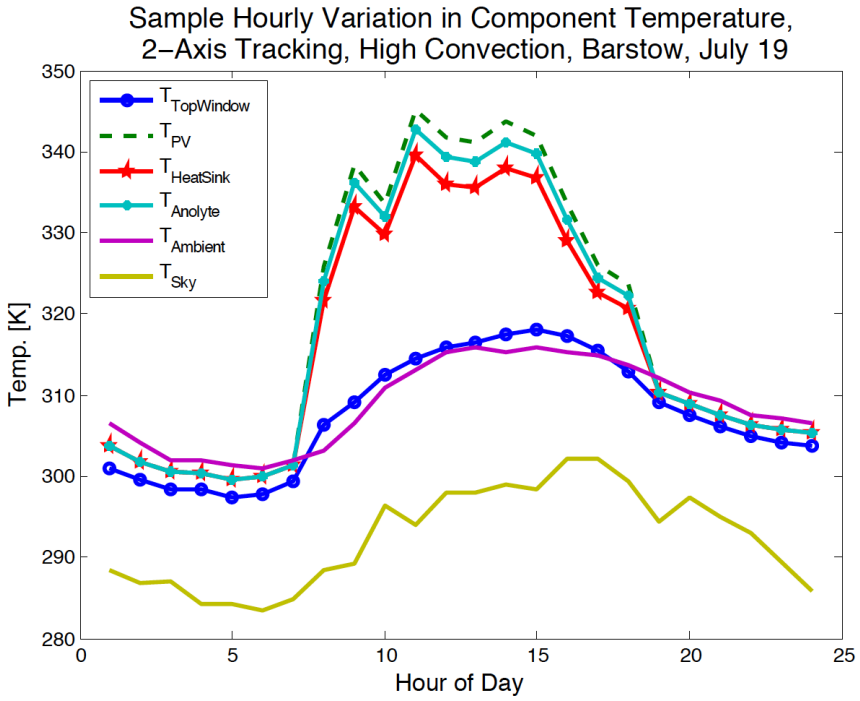

Figure 6.9: Typical Operating Temperature Profile on Summer Day in Barstow

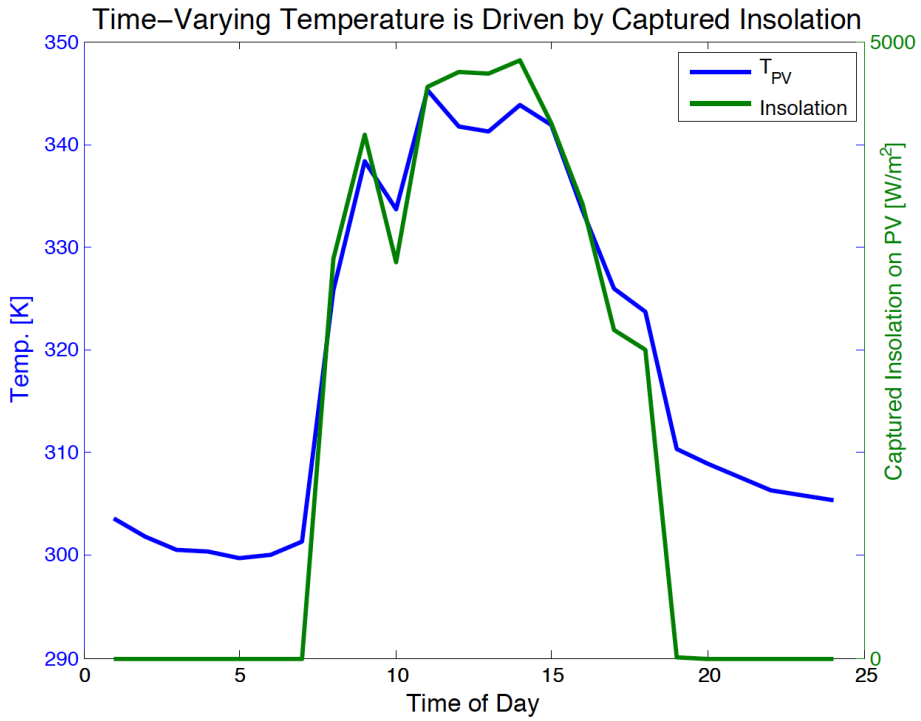

Figure 6.10: Captured Insolation as Driver of the System Temperature

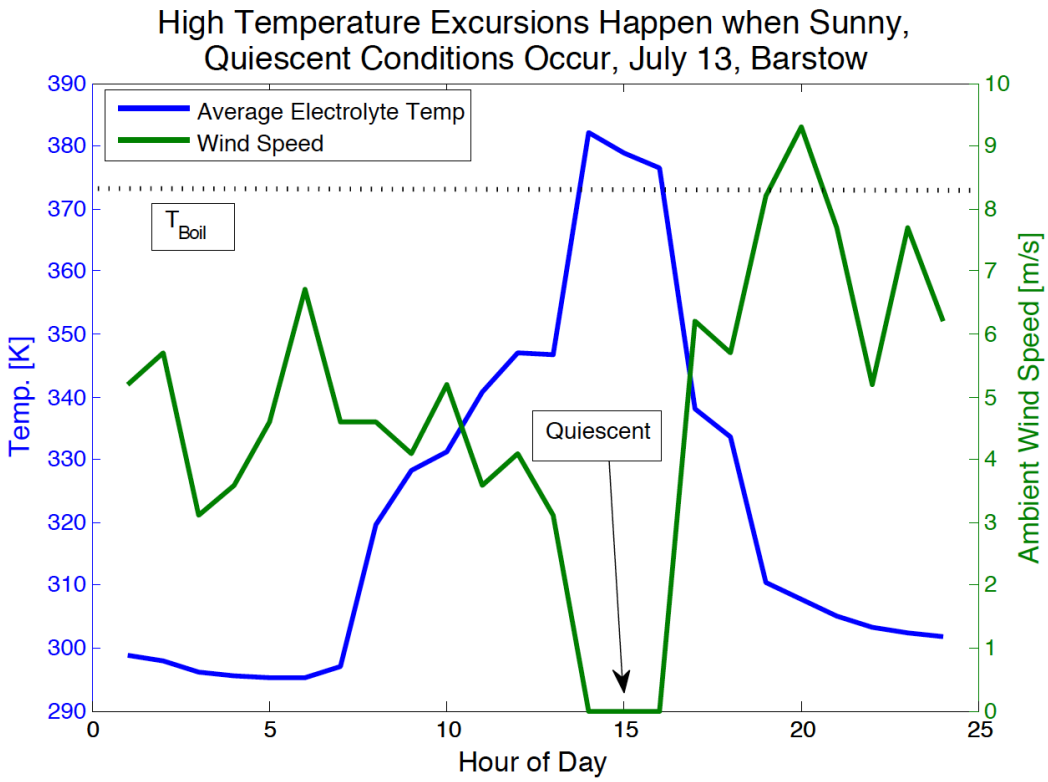

Figure 6.11: Temperature Increases above 100°C as Wind Speed Drops

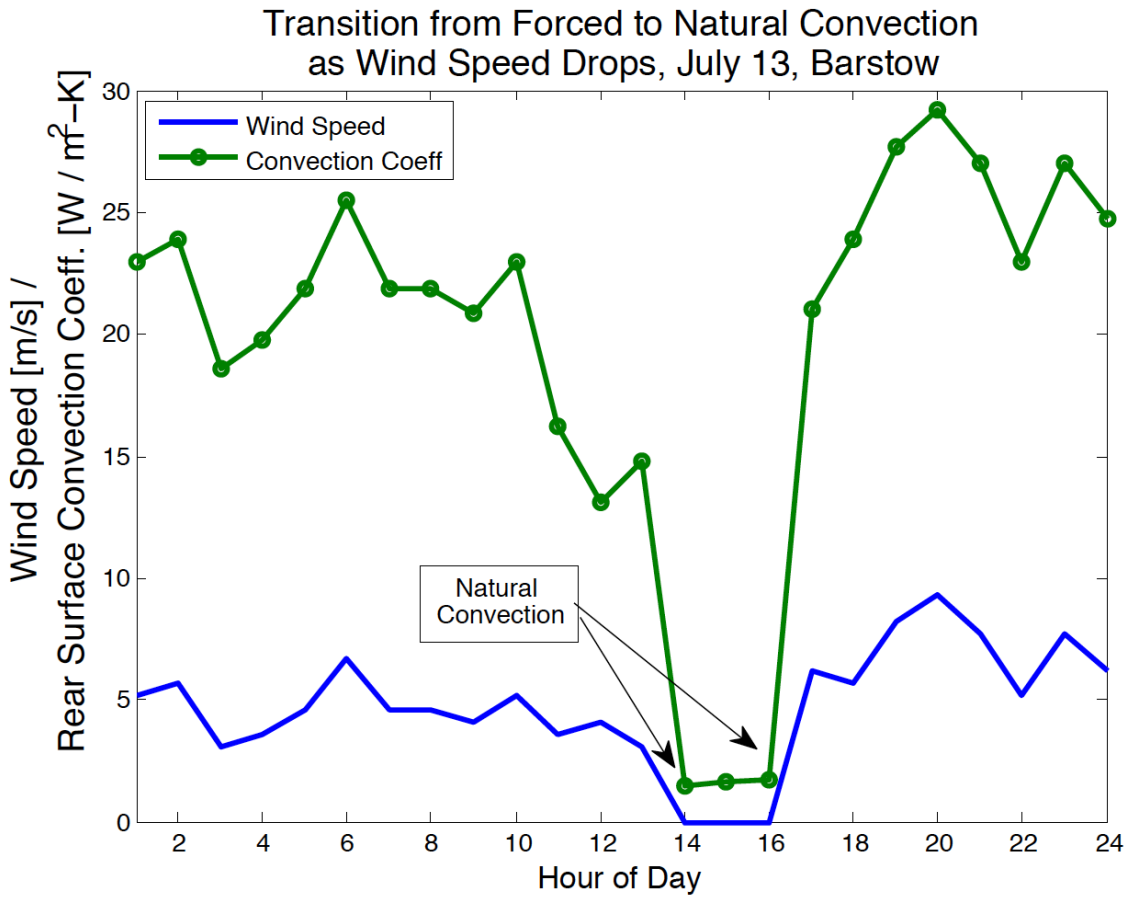

Figure 6.12: During Excursion over 100°C, Wind Speed's Effect on the Regime of Convective Heat Transfer is Evident

causes a spike in temperature, a phenomenon observed throughout the year whenever there are quiescent periods during the middle of a sunny, hot day. This explains why varying the forced convection coefficients had little effect on the total number of hours that the device operated above 100 °C. During cold weather, the ambient temperature is warmer than the sky temperature, and thus a higher convection coefficient actually helps to warm the device somewhat relative to the lower convection scenario.

Excursions below -4.4 °C are a result of cold ambient and sky temperatures. A general correlating trend to the number of hours operating below the lower safe limit is the number of hours where the ambient temperature is below 0 °C, as shown in Table 6.2.

6.4.3 Typical Operating Efficiency Profiles

To further elucidate why η_{STH} varies during operation, we can look at two consecutive days with good and bad direct solar insolation resource. These are shown in Figure 6.13. We see that, on the first day, the η_{STH} is near or slightly above 12% throughout the majority of the day. The following day, however, there is a drop

of η_{STH} in the afternoon. The cause of this is shown in on the graph at the bottom, where the first day shows excellent direct solar resource peaking above 800 W/m^2, whereas the second day has a larger portion of its solar resource incident as diffuse light (exceeding 50% at hour 40 (4:00 pm)), and thus a lower η_{STH}.

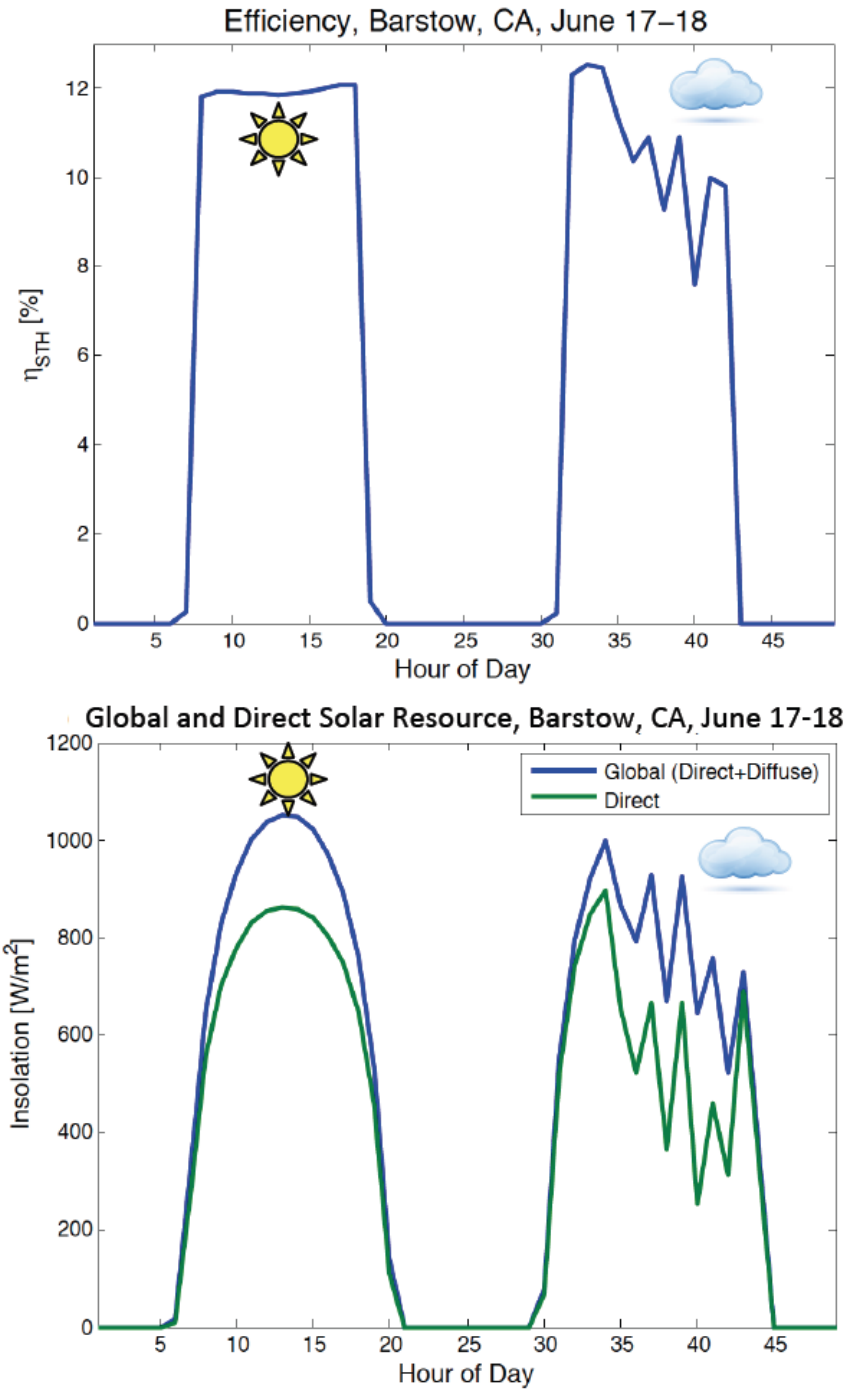

Figure 6.13: Operational Efficiency and Insolation Profiles on 2 Consecutive Days in June in Barstow

6.5 Potential Improvements to Design Thermal Performance

Given the large number of excursions from the desirable temperature range, there are a number of potential ways in which the device could be improved. The fall broadly into the categories of extending the operational temperature window and using active or passive thermal management. It should be noted that the climate data utilized here does not capture record temperatures[127], thus these measures may be ineffective at preventing device failure during record heat or cold.

6.5.1 Extending the Operational Temperature Window

As discussed in Chapter 3, the limits of the device temperature are governed by the necessity of keeping the electrolyte from freezing, as well as maintaining the stability of the membrane. Thus, we could potentially employ methods to broaden the operational temperature bounds of the CPEC and so obviate the need for temperature control methods.

In order to depress the electrolyte freezing point, one could increase the concentration of H_2SO_4 in the electrolyte[62], add supporting electrolytes[128], introduce other additives, or drain the system during cold weather. The modeled system employs 1.0 M H_2SO_4, but, a 2.0 or 3.0 M solution of H_2SO_4 has a freezing point of approximately -11.5 °C or -23.9 °C [62], respectively, the latter of which is below the minimum temperature attained by the CPEC electrolyte in all locations. In this range of molarity, as the solution freezes, the acid will be preferentially concentrated in the remaining liquid[62], which could potentially corrode device components in contact with the acid. Any electrolyte additives must not be preferentially oxidized or reduced by the electrochemical processes, or otherwise harm CPEC components. Additionally, additives may, in the case of a supporting electrolyte, induce polarization losses due to crossover in the PEM[39]. Another potential method to prevent freezing of the electrolyte would be to drain the systems whenever cold weather was predicted, which is similar to the methodology employed for freeze protection of PEM fuel cells in passenger vehicles[130]. The PEMs would likely survive temperatures well below 0 °C if not subject to tearing by the formation of ice[130], though other damage may result in, e.g., the catalyst layers from ice formation or drying. This would also add system complexity. Finally, designing a system that allowed for the formation of ice in the cell without damaging CPEC components would be the most preferable solution to avoid damage from cold temperatures.

In order to increase the maximum operating temperature of the device, various new membranes could be developed in place of Nafion, which is already a research thrust in the PEM fuel cells community[59]. The CPEC could potentially designed without a membrane. This would also tend to reduce solution polarization if supporting electrolytes were added to reduce the freezing temperature[40], but preventing gas crossover would be difficult, as demonstrated elsewhere[131]. Additionally, system pressurization could increase the boiling temperature of the electrolyte. The freezing temperature would be negligibly affected by system

pressurization in the range of realistic pressures, i.e. a few tens of atmospheres at most [132]. Further pressurization would necessitate careful design to prevent device failure due to mechanical stresses. Finally, increasing the total molarity of the supporting electrolyte or H_2SO_4 will increase the electrolyte's boiling temperature[128].

6.5.2 Temperature Management Solutions to Improve CPEC Operation

There are a number of options to passively cool the CPEC. Most concentrating PV systems operate using a finned or pin-type heat sink to reduce the PV cell's temperature, and ensure good thermal contact between the PV cell and this heat sink. This approach was taken by Aroutianian, Arakelyan and Shahnazaryan, and it allowed for passive cooling of their CPEC[133]. Incorporating a heat sink on the back of the device would be useful as long as it could provide sufficient natural convective heat transfer rates to prevent high device temperatures during hot, sunny, quiescent ambient conditions. Literature available on heat exchangers[134] shows that natural convection coefficients of 5 W/m^2-K are reasonably achievable.

In order to model this effect, the data for Barstow were re-run for July 13, which is the day on which the highest CPEC temperature was achieved in all simulated locations. Instead of calculating the external convection coefficients with the methodology explained in Chapter 5, a constant rear external convection coefficient, varying from 0-5 W/m^2-K was used. The radiative heat transfer coefficient is calculated as before with equations 5.14 and 5.15, and the rear surface emissivity set at 0.93. The resulting mean of the anolyte and catholyte temperatures for each hourare shown in Figure 6.14. Enforcing this minimum convective heat transfer coefficient is able to prevent the system from operating above the maximum safe temperature for convection coefficients of 4 W/m^2-K or greater. This neglects the change in forced convection coefficients that would result from employing a heat exchanger rather than a flat plate at the CPEC's rear surface; thus, a full year of analysis is not performed.

The presence of a rear heat sink will change the effective radiative view factor of the heat sink to the surrounds. Thus, to model the extreme case, where there was no radiation from the back surface, the rear surface emissivity was set to 0 and the rear convection coefficient was varied as before. This is shown in Figure 6.15. In these results, a convection coefficient of greater than 10 W/m^2-K is necessary to keep the rear surface temperatures below 100 °C. Clearly, there will be some radiative heat transfer from the rear heat sink; however, further simulation of specific heat sink geometries that account for radiative and convective heat transfer is needed to say whether or not this measure will be sufficient in preventing the device from exceeding 100 °C.

There are several methods possible to enable active cooling of the device. One example would be to pump the electrolyte through the device at such a rate that it would actively cool the PV layers and membrane, as was shown by Dumortier and Haussener[48]. Heat would then be exhausted to the surrounds in an external radiator system or other means. Such a system could also employ insulation, rather than a

heat sink, around the PEC, such that stopping the flow of electrolyte would mean that the CPEC exchanged very little heat with the surrounds during cold weather. This might reduce the number of hours the system operated below -4.4 °C. This measure would add complexity to the system.

Another method to actively cool the device could be to use the tracking equipment to aim the CPEC away from the sun whenever the wind speed dropped below a minimum set point (e.g., dropped to 0 m/s), during high-insolation periods. The effect of this on $\eta_{STH,Avg}$ would depend on the local climate, but would be very small for locations with only a few hours per year of excursion above 100 °C. Additionally, as shown in[24], it is possible to use an electrical resistance heater to provide heating to the device to prevent it from freezing during extremely cold weather. This obviously had a strongly negative effect on the overall EROEI of the system, especially in colder climates. For the simulated PEC in Sathre et al.[24], the annual heating losses per square meter of aperture were on the order of 27-58% of the annual energy yielded per square meter by fuel production.

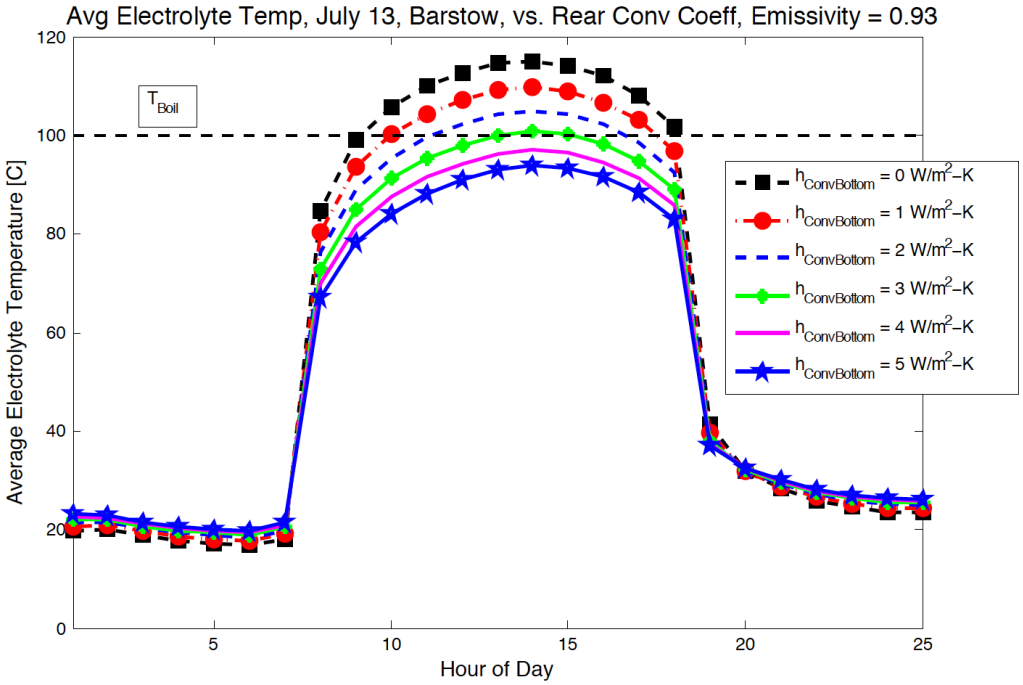

Figure 6.14: Effect of Varying Rear Convective Heat Transfer Coefficient on Average Electrolyte Temperature During Extreme Hot Day

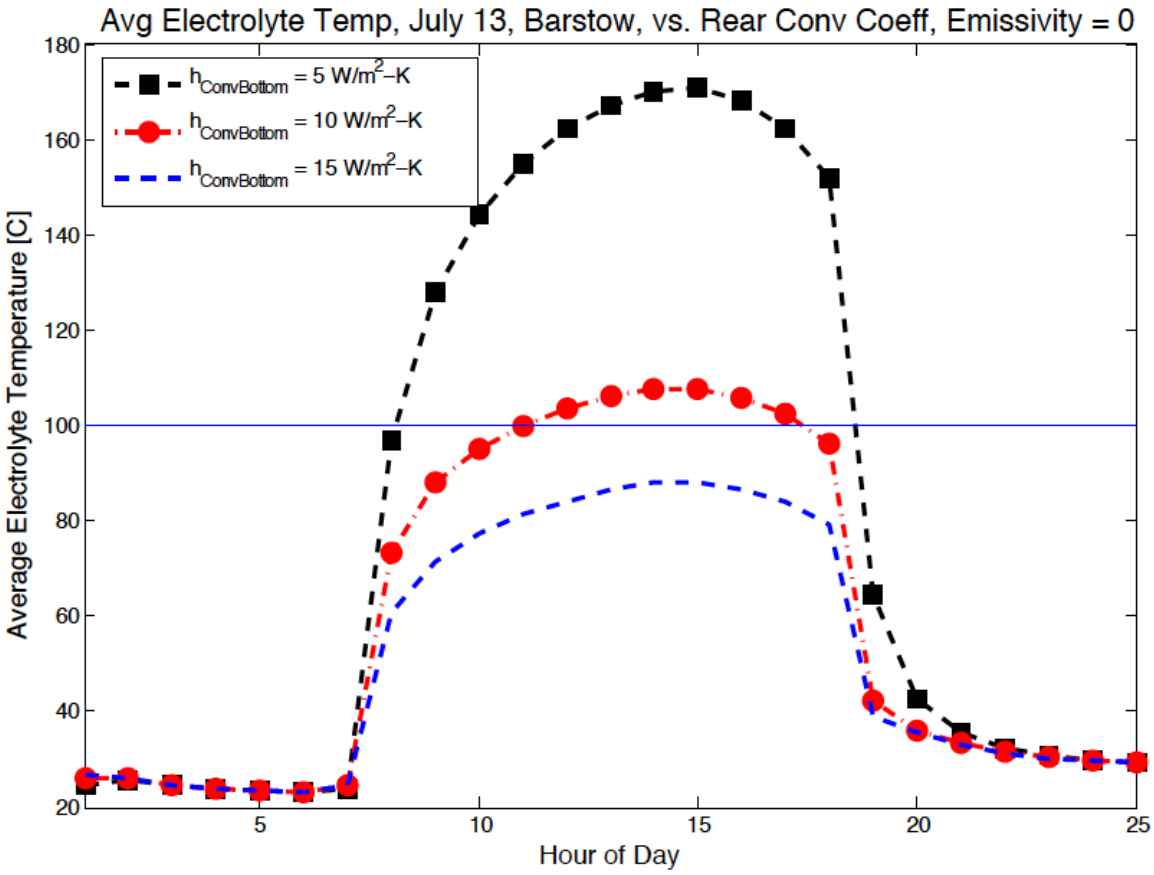

Figure 6.15: Effect on Average Electrolyte Temperature of Varying Rear Convective Heat Transfer, with No Rear Radiative Heat Loss

6.6 Conclusions

Overall, the device performance exhibited here is one that must be improved from a thermal management standpoint. In all locations, it was found that excursions below -4.4°C and/or above 100°C occurred. Using a heat sink to improve heat transfer may help reduce excursions above 100°C. Increasing the solute content of the electrolyte may also prevent freezing in the electrolyte.

This work therefore serves to guide what areas of focus are necessary to enable deployment of PECs that utilize optical concentration. Indeed, given the conclusions of Sathre et al.[24], some sort of temperature management will be necessary regardless of whether or not the PEC uses optical concentration, unless extra engineering work is performed to broaden the operational temperature window of these devices or better manage the device temperature. This obviously stands as an impediment to the deployment of these devices.

Chapter 7: Conclusions

7.1 Introduction

In Chapter 6, it is found that PECs that employ optical concentration can achieve an average weighted operational η_{STH} of 11.2%, while operating for 12 non-consecutive hours per year above 100 °C, and 68 non-consecutive hours per year below -4.4 °C in Daggett, CA. These results are highly location dependent, and for systems deployed in a poor insolation location, e.g., Quillayute, WA, these same values are an average operational η_{STH} of 9.1%, operation for 0 hours per year above 100 °C, and 264 hours per year below -4.4 °C. Overall, the result of these investigations indicate that using optical concentration in conjunction with PECs is a promising means to efficiently produce H_2.

While the computational model presented in this dissertation attempts to account for many of the multiphysics phenomena present in PECs, there are inevitably improvements that can be made that will further its sophistication and predictive capabilities. These improvements are outlined in this chapter with an aim towards guiding future research on the subject.

Additionally, the future direction for the solar fuels community is discussed in this chapter, with an emphasis on the challenges and opportunities for such systems to be developed into commercially viable systems.

7.2 Future Work for Improving Modeling Efforts

In this section, the various improvements that could supplement the modeling work done in this dissertation are discussed. An emphasis is placed on bringing the model's predictions closer to reality, as well as expanding the model's capabilities to consider systems that would potentially be more efficient and operate within a narrower temperature range than the model described herein.

7.2.1 Experimental Validation of the Heat Transfer Model

In order to experimentally validate the conclusions of this model, several different prototypes could be built. The first improvement should be made to the aspect of PECs covered in this dissertation that has received the least attention by the scientific community, which is the thermal performance of PECs.

The convection coefficients used to model the exterior boundary conditions in this work are for devices with typical exterior dimensions on the order of tens of centimeters, e.g. a solar PV module. Typical PECs that have been built are an order of magnitude smaller owing to the difficulty of manufacturing a good, large area protection coating that can prevent electrolyte ingress into the active PV layers. This was the case, e.g., in Verlage et al.[43], and many other investigations like it. Thus, a means of quantifying the exterior convection coefficients for these smaller

prototypes must serve as the first step in validating the thermal model constructed herein.

In order to measure the proper convection coefficients, one could start by measuring the average device exterior surface temperature, e.g. with an IR camera, thermocouples, or both. A concurrent measurement of ambient temperature and wind velocity would give the next required set of data. Then, one could use an electrical strip heater of the same dimensions of the PV cell to deliver some heat flux to a PEC device, allowing for the derivation of the forced and free convection coefficients from the exterior of the device. Within the PEC, further temperature measurements can be made using corrosion-resistant thermocouples, as long as good thermal contact is ensured with the layer whose temperature is desired to be known. Then, by replacing the strip heater with a functioning, calibrated PV cell that can split water under illumination, and by operating this device while collecting the produced products and measuring the PV cell's operating point on its j-V curve, one could calculate the total photoelectrochemical waste heat generation in the PEC. This same system could also estimate the reduction in optical power entering the PV cell by measuring the reduction in J_{SC} when encapsulated in the PEC chassis, and so the amount of heating by light absorption in the PEC could be estimated. Thus, one would have the ability to validate various model parameters by fine-tuning the computational model and experimental prototype until reasonably good agreement was found between the two.

From this starting point, the eventual construction of an optically concentrating PEC would be the ultimate goal, as this would then allow more parameters to be validated, as well as showing design problems not elucidated in the multiphysics model. Additionally, operational criteria, such as the temperatures at which device failure occur, could be determined through destructive tests.

7.2.2 Modeling and Experimental Characterization of Gas Bubbles in the PEC System

Another critical element missing from the multiphysics model presented in this dissertation is the effect of H_2 and O_2 bubbles on device performance. These bubbles affect the performance of demonstrated PECs[43,135], because bubble can scatter light in the electrolyte[136] and on the surface of the PV cells[99], reduce the effective electrode area for electrochemical reactions[137] and reduce the thermal and electrical conductivity (or any property governed by a Fourier's law-like equation) of the electrolytic solution[138,139]. There can also be additional convective effects from the presence of gas bubble evolution at the electrode[40,140,141] on mass and heat transfer. These effects would only become more important as the current densities and required rates of heat dissipation in the device increased due to the presence of optical concentration.

In order to test such effects, it is necessary to characterize bubbles' electrode coverage fraction for a given current density, the size distribution of bubbles in the system (on the electrode surface and in the electrolyte bulk) and the locations where these bubbles are present. The author attempted to characterize several

systems from this standpoint using quartz glass slides coated in FTO and NiFeOx OER catalysts in 1 M KOH solutions. However, the corrosion of transparent conducting oxide layers and various other system components resulted in data that could not be replicated from run to run (the catalyst material would flake off after a few minutes of operation), and is thus left for future investigations. Starting points for investigators looking to more fully characterize the system experimentally can be found in, e.g., Sides[142]. If it is possible to use metallic electrodes instead of glass electrodes and still perform the necessary imaging, this will enhance experimental repeatability. This is because such electrodes could be less prone to corrosion during experimental characterization. Additionally, reducing the ohmic drop in solution (i.e. having small distances between working and counter electrodes) will reduce the operational potential, and thus reduce the chance of electrode corrosion.

Different device architectures could more or less easily prevent the deleterious effects of gas bubble buildup in the system. Potential methods to keep gas bubbles out of the system are to flow the electrolyte in a properly designed system[38], to pressurize the system (reducing the volume of gas bubbles for a given number of moles) and to ensure that as many surfaces as possible within the cell are hydrophilic[143]. The latter requirement arises because the larger contact angles that bubbles in aqueous media make with hydrophobic surfaces mean that surface tension is more effective at holding these bubbles in place than those adhered to hydrophilic surfaces.

Overall, the presence of bubbles represents a problem that the solar fuels community would like to have, and issues pertaining to device stability are more pressing. However, this emerging issue, along with the need to collect product gases and deliver them to some external piping system, will be important if the technology is deployed on any commercial scale.

7.2.3 Implementing Patterned Rather than Planar OER/HER Catalysts

Recent papers in the PEC field have demonstrated the effectiveness of utilizing low surface area coverage fraction catalyst islands, rather than conformal coatings of thin catalyst layers. This enable more efficient light capture while still exhibiting reasonably low catalytic overpotentials[43,144,145]. Part of the reason for this is that the parasitic absorption of light in a thin, conformal catalyst layer can be significant, as found in this work and others[146]. The absorption by a thin catalyst layer can be potentially greater than that in optically thick islands of catalyst on a protection layer, if the photoelectrode area covered by opaque catalyst islands is sufficiently small[144].

Another factor for employing these catalyst islands is that many of the demonstrated systems, including the triple-junction system modeled herein, cannot perform the OER at their illuminated face do the fact that the cells are polarized to provide electrons, rather than holes, at their illuminated surface. The available HER catalysts tend to be optically opaque to visible light, hence patterning is more of a necessity than with IrO_2 or other OER metal oxide catalysts. The author chose not to model this effect due to the fact that the facile computation of electrolyte potential drop given in equations 3.32-3.34 cannot be extended to an electrode with a non-

uniform current density at its surface. To extend this model to allow the modeling of these catalyst islands would require running many COMSOL simulations of the system, solving the Nernst-Planck equation (equation 3.31) and other governing equations for various system conditions and utilizing a lookup table to simulate device performance. The use of the TMM and Equations 4.59-4.62 could, however, be adapted to model a surface covered in patterned catalysts with reasonable accuracy.

In a system operating under concentrated sunlight with catalyst islands, the electrochemical performance would suffer, though photovoltaic performance could be enhanced significantly, as exhibited in Sun et al.[145]. Additionally, this would potentially allow for a multi-layer ARC to be placed on top of the protection layer, as long as it was chemically compatible with the electrolyte and its deposition process did not interfere with charge transport through the protection layer to the catalyst sites, or with the PV cell's operational characteristics. A multilayer ARC could enable broadband transmission, from multiple incident angles[147]. The latter system is depicted schematically in **Figure 7.1**

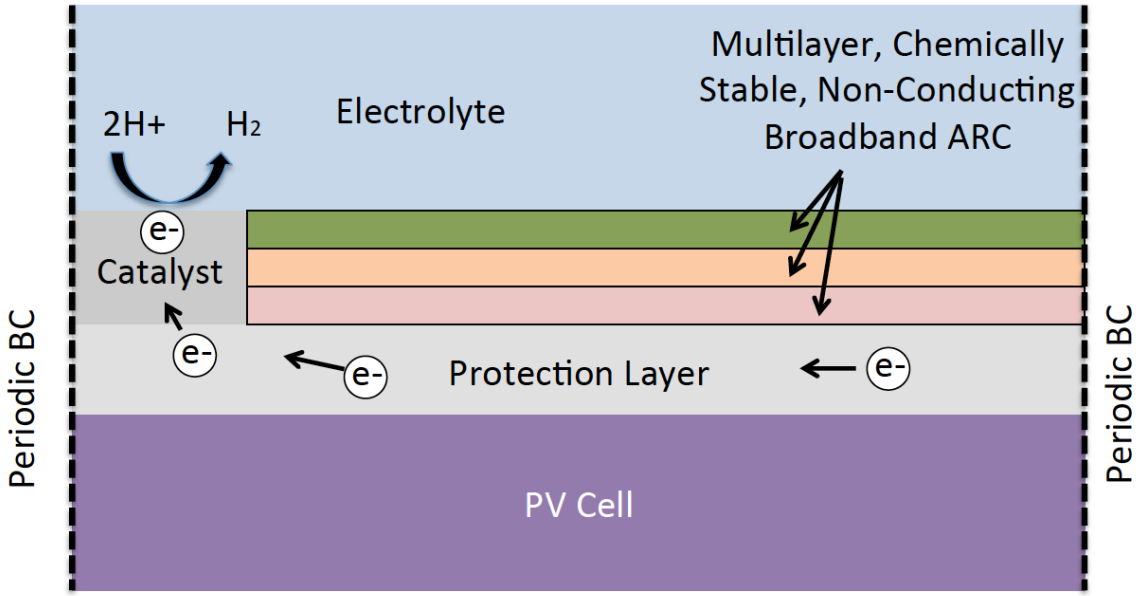

Figure 7.1: Schematic of PEC with Catalyst Islands and Multilayer, Broadband ARCs to Enhance Light Transmission (Not Drawn to Scale)

7.2.4 Assessing the Effect of Electrolyte Freezing Point-Depressing Agents

As shown in Chapter 6, depressing the electrolyte freezing point would be advantageous as it could enable operation in colder climates without the need to heat the electrolyte or protect it from freezing by pumping it out of the device during cold weather. Thus, experimental testing of such additives is necessary to elucidate their potential role in improving the deployed performance of PECs. So too, would be incorporating the effects into the photoelectrochemical model, especially to determine how product selectivity, system component corrosion and polarization losses would be affected by these agents.

7.2.5 Modeling Mechanical Stress as a Result of Pressurization and Thermal Cycling

As shown in Sathre et al.[24], a significant portion of the energy required to operate a PEC plant results from the need for gas compression. This could be reduced by operating the PECs at higher internal pressure, which can be achieved for relatively small increases in the system's overpotential[148]. This extra compression force would impart mechanical stresses on the PEC's various components, and thus modeling the effect of this on the cell would be necessary to prevent another means of (rather catastrophic) device failure. Additionally, mechanical stresses in the system from thermal cycling could potentially cause device failure.

7.2.6 Modeling Diffusion-Limited Electrochemical Behavior

Due to the simplicity of the model employed in this investigation, the effect of diffusion-limited behavior in the system is not modeled. The reason is that this again requires solving the Nernst-Planck equation in COMSOL or some other numerical solver, and thus it was thought that such a system would require too much time to simulate. However, implementing this numerical model will further narrow the phase space for the width of the electrodes in the system (as explored in Chapter 3).

7.2.7 Improving Optical Design and Modeling Capabilities

In order to potentially improve device performance, a parabolic mirror designed to illuminate a PEC should be investigated, as such a design's ability to reduce the average number of reflections that light undergoes prior to entering the PEC could potentially enhance optical throughput. Additionally, this can allow for heat transfer from all sides of the PEC rather than just through the bottom. Employing better optical models to be able to simulate graded index of refraction-type ARCs on the PV cell and other interfaces may be of use, as would investigating the viability of multilayer ARCs on surfaces other than the PV cell. The optimal ARC design might be determined with a genetic algorithm, as shown in, e.g., Shubert et al.[147].

7.2 The Future of PECs

It is imperative that we find a means to power the transportation sector other than fossil fuels. As explained in Chapter 1, it seems unlikely that biofuels or electrification will enable this transition in a meaningful fashion. Additionally, energy storage is absolutely necessary if renewable energy makes up a large fraction of the electricity generation capacity[149], regardless of whether or not the predictions made about the transportation sector turn out to be accurate.

There are many challenges faced by CPECs, and these must all be surmounted in order for commercialization of the technology to occur. As explained in this dissertation, immense efforts must be undertaken to ensure that wireless

PEC devices do not corrode, overheat or freeze. Even if the stability issue is solved in wireless PECs, the difficulty of getting permitting to construct a system that employs many liters of caustic electrolytes in the natural environment or on a rooftop is difficult to surmount.

In addition to the operational challenges faced by wireless PECs, conventional electrolyzers already exist and are superior to PECs in most metrics. Electrolyzer efficiencies of 70% are commercially realizable[43], and it seems hard to imagine beating this significantly with a PEC system when net operating cell potentials of 1.7 V (corresponding to 72% efficiency) are the norm[21]. Even if the operating cell potential can be reduced, there are still optical losses that will reduce the overall η_{STH}. Electrolyzers also generally have lifetimes on the order of 20,000-90,000 hours under continuous operation[150], which is far more than the current state of the art for PECs[36]. Finally, electrolyzers can be placed in doors and in a space that is not illuminated. As a result, the necessity of exposing the electrolyzers to extreme ambient temperatures is not present, and the extra heat generation due to optical absorption and PV cell inefficiency can be avoided. Thus, temperature regulation is an easier task for electrolyzers. Finally, electrolyzers can leverage the declining cost of conventional single-junction PV modules, which makes up the majority of the cost of producing fuel for such systems[151], and have been declining rapidly in price[152]. Wireless PECs cannot use single-junction PV cells and still be efficient[42].

7.3 Conclusions

Ultimately, it is probably too early to make long-term predictions as to the eventual viability of wireless PECs, but there are many improvements that need to be made to the technology. However, we as a species must determine the best solution for storing solar energy. Otherwise, coming generations will get to determine just how bad the effects of climate change are going to be if we continue to use fossil fuels to derive most of our global primary energy supply. It is the author's hope that humans act quickly, and act on a meaningfully large scale.

References

1. Chu, S. & Majumdar, A. Opportunities and challenges for a sustainable energy future. *Nature* **488,** 294–303 (2012).

2. Aalst, M. van *et al. Climate Change 2014: Impacts, Adaptation, and Vulnerability*. *Assessment Report 5* (2014).

3. Farrell, A. E. & Brandt, A. R. Risks of the oil transition. *Environmental Research Letters* **1,** 014004 (2006).

4. *Annual Energy Outlook 2015: Executive Summary*. (2015). at <http://www.eia.gov/forecasts/aeo/executive_summary.cfm>

5. Lewis, N. S. & Nocera, D. G. Powering the planet: chemical challenges in solar energy utilization. *Proc. Natl. Acad. Sci. U. S. A.* **103,** 15729–15735 (2006).

6. *International Energy Outlook 2013: Delivered Energy Consumption by End-Use Sector and Fuel, Total World*. (2013). at <http://www.eia.gov/oiaf/aeo/tablebrowser/#release=IEO2013&subject=0-IEO2013&table=15-IEO2013&region=4M0&cases=ReferenceMd041117>

7. CO2 Emissions from fuel combustion: Highlights (2014 edition). *International Energy Agency* (2014). at <http://www.iea.org/media/freepublications/stats/CO2_Emissions_From_Fuel_Combustion_Highlights_2014.XLS>

8. Amine, K., Kanno, R. & Tzeng, Y. Rechargeable lithium batteries and beyond: Progress, challenges, and future directions. *MRS Bull.* **39,** 395–401 (2014).

9. McCall, T. *The Price of Batteries*. (2011). at <http://www.technologyreview.com/sites/default/files/legacy/jan11_feature_electric_cars_p61.pdf>

10. *Weekly Retail Gasoline and Diesel Prices*. (2015). at <http://www.eia.gov/dnav/pet/pet_pri_gnd_dcus_nus_w.html>

11. Annual energy outlook 2015: Energy consumption by sector and source. *US Energy Information Administration* (2015). at <from http://www.eia.gov/beta/aeo/#/?id=2-AEO2015&region=10&cases=ref2015~highprice&start=2012&end=2040&f=A>

12. Niven, R. K. Ethanol in gasoline: Environmental impacts and sustainability review article. *Renewable and Sustainable Energy Reviews* **9,** 535–555 (2005).

13. Pimentel, D. Ethanol Fuels: Energy Balance, Economics,\rand Environmental Impacts are Negative. *Nat. Resour. Res.* **12,** (2003).

14. Von Blottnitz, H. & Curran, M. A. A review of assessments conducted on bio-ethanol as a transportation fuel from a net energy, greenhouse gas, and environmental life cycle perspective. *J. Clean. Prod.* **15,** 607–619 (2007).

15. McPhail, L. L. & Du, X. Ethanol Strengthens the Link Between Agriculture and Energy Markets. *Econ. Res. Serv. Amber Waves* **10,** 2012 (2012).

16. *Annual Energy Outlook 2013: Liquid Fuels Supply and Disposition*. (2013). at <http://www.eia.gov/oiaf/aeo/tablebrowser/#release=AEO2013&subject=0M>

17. *Major Crops Grown in the United States*. (2013). at <http://www.epa.gov/agriculture/ag101/cropmajor.html>

18. Blankenship, R. E. *et al.* Comparing photosynthetic and photovoltaic efficiencies and recognizing the potential for improvement. *Science* **332,** 805–809 (2011).

19. Singh, M. R., Clark, E. L. & Bell, A. T. Effects of Electrolyte, Catalyst, and Membrane Composition and Operating Conditions on the Performance of Solar-Driven Electrochemical Reduction of Carbon Dioxide. *Phys. Chem. Chem. Phys.* **17,** 18924–18936 (2015).

20. Bard, A. J. & Faulkner, L. R. *Electrochemical Methods: Fundamentals and Applications, 2nd Ed. John Wiley and Sons* (2001).

21. Singh, M. R., Stevens, J. C. & Weber, A. Z. Design of Membrane-Encapsulated Wireless Photoelectrochemical Cells for Hydrogen Production. *J. Electrochem. Soc.* **161,** E3283–E3296 (2014).

22. Green, M. a, Emery, K., Hishikawa, Y., Warta, W. & Dunlop, E. D. Solar cell ef fi ciency tables (version 43). *Prog. Photovoltaics Res. Appl.* **22,** 1–9 (2014).

23. Hu, S., Xiang, C., Haussener, S., Berger, A. D. & Lewis, N. S. An analysis of the optimal band gaps of light absorbers in integrated tandem photoelectrochemical water-splitting systems. *Energy Environ. Sci.* **6,** 2984 (2013).

24. Sathre, R. *et al.* Life-cycle net energy assessment of large-scale hydrogen production via photoelectrochemical water splitting. *Energy Environ. Sci.* - (2014). doi:10.1039/C4EE01019A

25. Nielander, A. C., Shaner, M. R., Papadantonakis, K. M., Francis, S. a. & Lewis, N. S. A taxonomy for solar fuels generators. *Energy Environ. Sci.* **8,** 16–25 (2015).

26. Fujii, K. *et al.* Characteristics of hydrogen generation from water splitting by polymer electrolyte electrochemical cell directly connected with concentrated photovoltaic cell. *Int. J. Hydrogen Energy* **38,** 14424–14432 (2013).

27. Jacobsson, T. J., Fjallstrom, V., Sahlberg, M., Edoff, M. & Edvinsson, T. A monolithic device for solar water splitting based on series interconnected thin film absorbers reaching over 10% solar-to-hydrogen efficiency. *Energy Environ. Sci.* **6,** 3676–3683 (2013).

28. Khaselev, O. A Monolithic Photovoltaic-Photoelectrochemical Device for Hydrogen Production via Water Splitting. *Science.* **280,** 425–427 (1998).

29. Peharz, G., Dimroth, F. & Wittstadt, U. Solar hydrogen production by water splitting with a conversion efficiency of 18%. *Int. J. Hydrogen Energy* **32,** 3248–3252 (2007).

30. Rocheleau, R. E., Miller, E. L. & Misra, A. High-efficiency photoelectrochemical hydrogen production using multijunction amorphous silicon photoelectrodes. *Energy & Fuels* **0624,** 3–10 (1998).

31. Yamada, Y. *et al.* One chip photovoltaic water electrolysis device. *Int. J. Hydrogen Energy* **28,** 1167–1169 (2003).

32. Licht, S. *et al.* Efficient Solar Water Splitting, Exemplified by RuO 2 -Catalyzed AlGaAs/Si Photoelectrolysis. *J. Phys. Chem. B* **104,** 8920–8924 (2000).

33. Fujishima, A & Honda, K. Electrochemical photolysis of water at a semiconductor electrode. *Nature* **238,** 37–38 (1972).

34. Reece, S. Y. *et al.* Wireless Solar Water Splitting Using Silicon-Based Semiconductors and Earth-Abundant Catalysts. *Science.* **334,** 645–648 (2011).

35. Walczak, K. *et al.* Modeling, Simulation, and Fabrication of a Fully Integrated, Acid-stable, Scalable Solar-Driven Water-Splitting System. *ChemSusChem* **40292,** (2015).

36. Ager III, J. W., Shaner, M., Walczak, K., Sharp, I. D. & Ardo, S. Experimental Demonstrations of Spontaneous, Solar-Driven Photoelectrochemical Water Splitting. *Energy Environ. Sci.* (2015). doi:10.1039/C5EE00457H

37. Xiang, C., Chen, Y. & Lewis, N. S. Modeling an integrated photoelectrolysis system sustained by water vapor. *Energy Environ. Sci.* **6,** 3713 (2013).

38. Clark, E. L., Singh, M. R., Kwon, Y. & Bell, A. T. Differential Electrochemical Mass Spectrometer Cell Design for Online Quantification of Products Produced during Electrochemical Reduction of CO2. *Anal. Chem.* 150723133616002 (2015). doi:10.1021/acs.analchem.5b02080

39. Modestino, M. a. *et al.* Robust production of purified H2 in a stable, self-regulating, and continuously operating solar fuel generator. *Energy Environ. Sci.* **7,** 297 (2014).

40. Singh, M. R., Papadantonakis, K., Xiang, C. & Lewis, N. S. An electrochemical engineering assessment of the operational conditions and constraints for solar-driven water-splitting systems at near-neutral pH. *Energy Environ. Sci.* **8,** 2760–2767 (2015).

41. Hu, S. *et al.* Amorphous TiO_2 coatings stabilize Si, GaAs, and GaP photoanodes for efficient water oxidation. *Science* **344,** 1005–9 (2014).

42. Abe, R. Recent progress on photocatalytic and photoelectrochemical water splitting under visible light irradiation. *J. Photochem. Photobiol. C Photochem. Rev.* **11,** 179–209 (2010).

43. Verlage, E. *et al.* A Monolithically Integrated, Intrinsically Safe, 10% Efficient, Solar-Driven Water-Splitting System Based on Active, Stable Earth-Abundant Electrocatalysts in Conjunction with Tandem III-V Light Absorbers Protected by Amorphous TiO2 Films. *Energy Environ. Sci.* (2015). doi:10.1039/C5EE01786F

44. Reece, S. Y. *et al.* Wireless Solar Water Splitting Using Silicon-Based Semiconductors and Earth-Abundant Catalysts. *Science* **334,** 645–648 (2011).

45. Kelly, N. a. & Gibson, T. L. Design and characterization of a robust photoelectrochemical device to generate hydrogen using solar water splitting. *Int. J. Hydrogen Energy* **31,** 1658–1673 (2006).

46. Pinaud, B. a. *et al.* Technical and economic feasibility of centralized facilities for solar hydrogen production via photocatalysis and photoelectrochemistry. *Energy Environ. Sci.* **6,** 1983 (2013).

47. Fabian, D. M. *et al.* Particle suspension reactors and materials for solar-driven water splitting. *Energy Environ. Sci.* (2015). doi:10.1039/C5EE01434D

48. Dumortier, M. & Haussener, S. Design guidelines for concentrated photo-electrochemical water splitting devices based on energy and greenhouse gas yield ratios. *Energy Environ. Sci.* (2015). doi:10.1039/C5EE01269D

49. Zhai, P. *et al.* Net primary energy balance of a solar-driven photoelectrochemical water-splitting device. *Energy Environ. Sci.* **6,** 2380 (2013).

50. Murphy, D. J. The implications of the declining energy return on investment of oil production. *Philos. Trans. A. Math. Phys. Eng. Sci.* **372,** 20130126 (2014).

51. Gupta, A. K. & Hall, C. a S. A review of the past and current state of EROI data. *Sustainability* **3,** 1796–1809 (2011).

52. Dias de Oliveira, M. E., Vaughan, B. E. & Rykiel, E. J. Ethanol as Fuel: Energy, Carbon Dioxide Balances, and Ecological Footprint. *BioScience* **55,** 593 (2005).

53. Haussener, S., Hu, S., Xiang, C., Weber, A. Z. & Lewis, N. S. Simulations of the irradiation and temperature dependence of the efficiency of tandem photoelectrochemical water-splitting systems. *Energy & Environ. Sci.* **6,** 3605 (2013).

54. Winkler, M. T., Cox, C. R., Nocera, D. G. & Buonassisi, T. Modeling integrated photovoltaic-electrochemical devices using steady-state equivalent circuits. *Proc. Natl. Acad. Sci.* **110,** E1076–E1082 (2013).

55. Nelson, J. *The Physics of Solar Cells*. *Imperial College Press* (2003).

56. Zondag, H. A. Flat-plate PV-Thermal collectors and systems: A review. *Renewable and Sustainable Energy Reviews* **12,** 891–959 (2008).

57. Nishioka, K. *et al.* Annual output estimation of concentrator photovoltaic systems using high-efficiency InGaP/InGaAs/Ge triple-junction solar cells based on experimental solar cell's characteristics and field-test meteorological data. *Sol. Energy Mater. Sol. Cells* **90,** 57–67 (2006).

58. Haussener, S., Hu, S., Xiang, C., Weber, A. Z. & Lewis, N. S. Simulations of the irradiation and temperature dependence of the efficiency of tandem photoelectrochemical water-splitting systems. *Energy Environ. Sci. Environ. Sci.* **6,** 3605 (2013).

59. Jalani, N. H., Dunn, K. & Datta, R. Synthesis and characterization of Nafion-MO2 (M = Zr, Si, Ti) nanocomposite membranes for higher temperature PEM fuel cells. *Electrochim. Acta* **51,** 553–560 (2005).

60. Weber, A. Z. & Newman, J. Coupled Thermal and Water Management in Polymer Electrolyte Fuel Cells. *J. Electrochem. Soc.* **153,** A2205 (2006).

61. Berger, A. & Newman, J. An Integrated 1-Dimensional Model of a Photoelectrochemical Cell for Water Splitting. *J. Electrochem. Soc.* **161 ,** E3328–E3340 (2014).

62. Gable, C., Betz, H. . & Maron, S. Phase equilibria of the system sulfur trioxide -- water. *J. Am. Chem. Soc.* **72,** 1445–1448 (1950).

63. Armstrong, S. & Hurley, W. G. A thermal model for photovoltaic panels under varying atmospheric conditions. *Appl. Therm. Eng.* **30,** 1488–1495 (2010).

64. Notton, G., Cristofari, C., Mattei, M. & Poggi, P. Modelling of a double-glass photovoltaic module using finite differences. *Appl. Therm. Eng.* **25,** 2854–2877 (2005).

65. Alonso García, M. C. & Balenzategui, J. L. Estimation of photovoltaic module yearly temperature and performance based on Nominal Operation Cell Temperature calculations. *Renew. Energy* **29,** 1997–2010 (2004).

66. Norwood, Z. & Kammen, D. Life cycle analysis of distributed concentrating solar combined heat and power: economics, global warming potential and water. *Environmental Research Letters* **7,** 044016 (2012).

67. Skoplaki, E. & Palyvos, J. a. On the temperature dependence of photovoltaic module electrical performance: A review of efficiency/power correlations. *Sol. Energy* **83,** 614–624 (2009).

68. Henry, C. H. Limiting efficiencies of ideal single and multiple energy gap terrestrial solar cells. *J. Appl. Phys.* **51,** 4494–4500 (1980).

69. Rodrigo, P., Fernández, E. F., Almonacid, F. & Pérez-Higueras, P. J. Models for the electrical characterization of high concentration photovoltaic cells and modules: A review. *Renew. Sustain. Energy Rev.* **26,** 752–760 (2013).

70. Singh, M. R., Clark, E. L. & Bell, A. T. Thermodynamic and Achievable Efficiencies for Solar-Driven Electrochemical Conversion of Water and Carbon Dioxide to Transportation Fuels. *Proc. Natl. Acad. Sci.* **Article In Press,** (2015).

71. Singh, P. & Ravindra, N. M. Temperature dependence of solar cell performance—an analysis. *Sol. Energy Mater. Sol. Cells* **101,** 36–45 (2012).

72. Green, M. *Solar Cells- Operating Principles, Technology and System Applications*. *Prentice-Hall, Inc.* (1982). doi:10.1016/0038-092X(82)90265-1

73. Chen, Y., Xiang, C., Hu, S. & Lewis, N. S. Modeling the Performance of an Integrated Photoelectrolysis System with 10 x Solar Concentrators. *J. Electrochem. Soc.* **161,** F1101–F1110 (2014).

74. Zohdi, T. I. Electromagnetic Properties of Multiphase Dielectrics: A Primer on Modeling, Theory and Computation. *Springer* (2012). at <http://www.springer.com/us/book/9783642284267>

75. Zohdi, T. I., Li, S. & Qian, D. *Multiscale Simulations and Mechanics of Biological Materials: Modeling and rapid simulation of high-frequency scattering responses of cellular groups*. (John Wiley & Sons Ltd, 2013). doi:10.1002/9781118402955

76. Hecht, E. *Optics 4th edition*. *Optics 4th edition by Eugene Hecht Reading MA AddisonWesley Publishing Company 2001* **1,** (2001).

77. Born, M. *et al.* Principles of Optics: Electromagnetic Theory of Propagation, Interference and Diffraction of Light, 7th (Expanded) Version. *Cambridge University Press* 952 (1999).

78. Byrnes, S. Steve Byrnes's Home Page. (2012). at <http://sjbyrnes.com/>

79. Heavens, O. S. Optical Properties of Thin Solid Films. *Dover Publications, Inc. (New York)* 261 (1991).

80. Nalwa, H. S. *Handbook of Thin Films, Vol. 2*. *Handbook of Thin Films* (Elsevier, 2002). doi:10.1016/B978-012512908-4/50003-5

81. Siegel, R. & Howell, J. *Thermal radiation heat transfer*. *Library* **Ill,** (2002).

82. Han, K. & Chang, C.-H. Numerical Modeling of Sub-Wavelength Anti-Reflective Structures for Solar Module Applications. *Nanomaterials* **4,** 87–128 (2014).

83. Aiken, D. J. High performance anti-reflection coatings for broadband multi-junction solar cells. *Sol. Energy Mater. Sol. Cells* **64,** 393–404 (2000).

84. Winston, R. Principles of solar concentrators of a novel design. *Solar Energy* **16,** 89–95 (1974).

85. Ning, X., Winston, R. & O'Gallagher, J. Dielectric totally internally reflecting concentrators. *Appl. Opt.* **26,** 300–305 (1987).

86. Rabl, A. Comparison of solar concentrators. *Sol. Energy* **18,** 93–111 (1976).

87. Kritchman, E. M. Linear Fresnel lens with polar tracking. *Appl. Opt.* **20,** 1234–1239 (1981).

88. Swanson, R. M. Promise of concentrators. *Prog. Photovoltaics Res. Appl.* **8,** 93–111 (2000).

89. Chaves, J. Introduction to Nonimaging Optics. *CRC Press* 560 (2008).

90. Carvalho, M. J., Collares-Pereira, M. & Rabl, A. Truncation of CPC Solar Collectors and its Effect on Energy Collection. *Sol. Energy* **35,** 393–399 (1985).

91. Leutz, R., Suzuki, A., Akisawa, A. & Kashiwagi, T. Shaped nonimaging Fresnel lenses. *J. Opt. A Pure Appl. Opt.* **2,** 112–116 (2000).

92. Welford, W. T. & Winston, R. High Collection Nonimaging Optics. *Academic Press* 296 (1989).

93. Debije, M. G. & Verbunt, P. P. C. Thirty years of luminescent solar concentrator research: Solar energy for the built environment. *Adv. Energy Mater.* **2,** 12–35 (2012).

94. Reda, I. & Andreas, A. Solar position algorithm for solar radiation applications. *Sol. Energy* **76,** 577–589 (2004).

95. Perez, R., Seals, R., Ineichen, P., Stewart, R. & Menicucci, D. A new simplified version of the perez diffuse irradiance model for tilted surfaces. *Sol. Energy* **39,** 221–231 (1987).

96. Miller, D. C., Kempe, M. D., Kennedy, C. E. & Kurtz, S. R. Analysis of transmitted optical spectrum enabling accelerated testing of multijunction concentrating photovoltaic designs. *Opt. Eng.* **50,** 013003 (2011).

97. Döscher, H., Geisz, J., Deutsch, T. & Turner, J. Sunlight absorption in water – efficiency and design implications for photoelectrochemical devices. *Energy Environ. Sci.* **7,** 2951–2956 (2014).

98. Surendranath, Y., Bediako, D. K. & Nocera, D. G. Interplay of oxygen-evolution kinetics and photovoltaic power curves on the construction of artificial leaves. *Proc. Natl. Acad. Sci.* **109,** 15617–15621 (2012).

99. Leenheer, A. J. & Atwater, H. a. Water-Splitting Photoelectrolysis Reaction Rate via Microscopic Imaging of Evolved Oxygen Bubbles. *J. Electrochem. Soc.* **157,** B1290 (2010).

100. Dodge, M. J. Refractive properties of magnesium fluoride. *Appl. Opt.* **23,** 1980 (1984).

101. Palik, E. Handbook of Optical Constants of Solids, Vol. 2. *Academic Press* 1096 (1991).

102. Palik, E. Handbook of Optical Constants of Solids: Vol. 1. *Academic Press* (1991).

103. Schubert, M. *et al.* Optical constants of GaxIn1-xP lattice matched to GaAs. *J. Appl. Phys.* **77,** 3416–3419 (1995).

104. Backholm, J. & Niklasson, G. a. Optical properties of electrochromic iridium oxide and iridium-tantalum oxide thin films in different colouration states. *Sol. Energy Mater. Sol. Cells* **92,** 1388–1392 (2008).

105. Rakic, A. D., Djurisic, A. B., Elazar, J. M. & Majewski, M. L. Optical properties of metallic films for vertical-cavity optoelectronic devices. *Appl. Opt.* **37,** 5271–5283 (1998).

106. Rakic, A. D., Djurišic, A. B., Elazar, J. M. & Majewski, M. L. Optical Properties of Metallic Films for Vertical-Cavity Optoelectronic Devices. *Appl. Opt.* **37,** 5271 (1998).

107. Zudans, I., Heineman, W. R. & Seliskar, C. J. In situ measurements of chemical sensor film dynamics by spectroscopic ellipsometry. Partitioning of a chromophore. *J. Phys. Chem. B* **108,** 11521–11528 (2004).

108. Khashan, M. A. & Nassif, A. Y. Dispersion of the optical constants of quartz and polymethyl methacrylate glasses in a wide spectral range: 0.2-3 microns. *Opt. Commun.* **188,** 129–139 (2001).

109. Rosell, J. I., Vallverdú, X., Lechón, M. a. & Ibáñez, M. Design and simulation of a low concentrating photovoltaic/thermal system. *Energy Convers. Manag.* **46,** 3034–3046 (2005).

110. Tembhurne, S., Dumortier, M. & Haussener, S. Heat Transfer Modeling in Integrated Photoelectrochemical Hydrogen Generators Using. 1–13 (2014).

111. Brutsaert, W. On a Derivable Formula for Long-Wave Radiation From Clear Skies. *Water Resour. Res.* **11,** 742–744 (1975).

112. Sugita, M. & Brutsaert, W. Cloud effect in the estimation of instantaneous downward longwave radiation. *Water Resour. Res.* **29,** 599–605 (1993).

113. Incropera, F. P. & DeWitt, D. P. *Fundamentals of Heat and Mass Transfer*. *John Wiley and Sons* **5th,** (2002).

114. Okhotin, A. S., Pushkarskii, A. S. & Gorbachev, V. V. *Thermophysical Properties of Semiconductors*. *Atom Publishing House* (1972).

115. Lucite Lux Continuous Cast Physical Properties. at <http://lucitelux.com/docs/Lucite-Lux-Continuous-Cast-Physical-Properties.pdf>

116. Properties of Plexiglass. at <http://www.plexiglas.de/product/plexiglas/en/about/faq/Pages/properties.aspx>

117. Cadillac Plastic. at <http://www.cadillacplastic.co.uk/media/pdfs/Plexiglas/product/PLEXIGLAS_99524.pdf>

118. Kumar, S. & Mullick, S. C. Wind heat transfer coefficient in solar collectors in outdoor conditions. *Sol. Energy* **84,** 956–963 (2010).

119. Sharples, S. & Charlesworth, P. S. Full-scale measurements of wind-induced convective heat transfer from a roof-mounted flat plate solar collector. *Sol. Energy* **62,** 69–77 (1998).

120. Sparrow, E. M. & Tien, K. K. Forced Convection Heat Transfer at an Inclined and Yawed Square Plate—Application to Solar Collectors. *J. Heat Transfer* **99,** 507 (1977).

121. Kind, R. J., Gladstone, D. H. & Moizer, A. D. Corrective Heat Losses From Flat-Plate Solar Collectors in Turbulent. **105,** 7–12 (2013).

122. Palyvos, J. a. A survey of wind convection coefficient correlations for building envelope energy systems' modeling. *Appl. Therm. Eng.* **28,** 801–808 (2008).

123. Fujii, T. & Imura, H. Natural-Convection Heat Transfer From Plate With Arbitrary Inclination. *Int. J. Heat Mass Transf.* **15,** 755–767 (1972).

124. Hassan, K.-E. & Mohamed, S. Natural Convection From Isothermal Flat Surfaces. *Int. J. Heat Mass Transf.* **13,** 1873–1886 (1970).

125. COMSOL Multiphysics 4.3 b). (2013).

126. Hollands, K., Raithby, G. & Konicek, L. Correlation Equations for Free Convection Heat Transfer in Horizontal Layers of Air and Water. *Int. J. Heat Mass Transf.* **18,** 879–884 (1975).

127. *National Solar Radiation Data Base: 1991-2005 Update: Typical Meteorological Year 3*. (2015). at <http://rredc.nrel.gov/solar/old_data/nsrdb/1991-2005/tmy3/>

128. Ge, X. & Wang, X. Calculations of freezing point depression, boiling point elevation, vapor pressure and enthalpies of vaporization of electrolyte solutions by a modified three-characteristic parameter correlation model. *J. Solution Chem.* **38,** 1097–1117 (2009).

129. Ohtake, T. Freezing Point of H2SO4 Aqueous Solutions and Formation of Stratospheric Ice Clouds. *Tellus* **45B,** 138–144 (1993).

130. Hwang, G. S. *et al.* Phase-change-related degradation of catalyst layers in proton-exchange- membrane fuel cells. *Electrochim. Acta* **95,** 29–37 (2013).

131. Jin, J. *et al.* An Experimental and Modeling/Simulation- Based Evaluation of the Efficiency and Operational Performance Characteristics of an Integrated, Membrane-Free, Neutral pH Solar-Driven Water-Splitting System. *Energy Environ. Sci.* **7,** 3371–3380 (2014).

132. Carey, V. *Liquid Vapor Phase Change Phenomena: An Introduction to the Thermophysics of Vaporization and Condensation Processes in Heat Transfer Equipment, Second Edition*. (Taylor Francis Group, 2008).

133. Aroutiounian, V. M., Arakelyan, V. M. & Shahnazaryan, G. E. Investigations of the metal-oxide semiconductors promising for photoelectrochemical conversion of solar energy. *Sol. Energy Mater. Sol. Cells* **89,** 153–163 (2005).

134. Mittelman, G., Dayan, a., Dado-Turjeman, K. & Ullmann, a. Laminar free convection underneath a downward facing inclined hot fin array. *Int. J. Heat Mass Transf.* **50,** 2582–2589 (2007).

135. Lee, M. H. *et al.* P-Type InP nanopillar photocathodes for efficient solar-driven hydrogen production. *Angew. Chemie - Int. Ed.* **51,** 10760–10764 (2012).

136. He, H., Li, W., Zhang, X., Xia, M. & Yang, K. Light scattering by a spheroidal bubble with geometrical optics approximation. *J. Quant. Spectrosc. Radiat. Transf.* **113,** 1467–1475 (2012).

137. Vogt, H. The actual current density of gas-evolving electrodes - Notes on the bubble coverage. *Electrochim. Acta* **78,** 183–187 (2012).

138. Tobias, C. W. Effect of Gas Evolution on Current Distribution and Ohmic Resistance in Electrolyzers. *J. Electrochem. Soc.* **106,** 833 (1959).

139. Sides, P. J. Resistance of a Planar Array of Spheres: Gas Bubbles on an Electrode. *J. Electrochem. Soc.* **129,** 2715 (1982).

140. Vogt, H. Heat transfer at gas evolving electrodes. *Electrochim. Acta* **23,** 1019–1022 (1978).

141. Vogt, H. Heat transfer in boiling and mass transfer in gas evolution at electrodes – The analogy and its limits. *Int. J. Heat Mass Transf.* **59,** 191–197 (2013).

142. Sides, P. J. A Close View of Gas Evolution from the Back Side of a Transparent Electrode. *J. Electrochem. Soc.* **132,** 583 (1985).

143. Janssen, L. J. J. Behaviour of and mass transfer at gas-evolving electrodes. *Electrochim. Acta* **34,** 161–169 (1989).

144. Chen, Y., Sun, K., Audesirk, H., Xiang, C. & Lewis, N. A Quantitative Analysis of the Efficiency of Solar-Driven Water-Splitting Device Designs Based on Tandem Photoabsorbers Patterned with Islands of Metallic Electrocatalysts. *Energy Environ. Sci.* **8,** 1736–1747 (2015).

145. Sun, K. *et al.* Stable solar-driven oxidation of water by semiconducting photoanodes protected by transparent catalytic nickel oxide films. *Proc. Natl. Acad. Sci.* 201423034 (2015). doi:10.1073/pnas.1423034112

146. Trotochaud, L., Mills, T. J. & Boettcher, S. W. An optocatalytic model for semiconductor-catalyst water-splitting photoelectrodes based on in situ optical measurements on operational catalysts. *J. Phys. Chem. Lett.* **4,** 931–935 (2013).

147. Schubert, M. F. *et al.* Design of multilayer antireflection coatings made from co-sputtered and low-refractive-index materials by genetic algorithm. *Opt. Express* **16,** 5290–5298 (2008).

148. Onda, K., Ichihara, K., Nagahama, M., Minamoto, Y. & Araki, T. Separation and compression characteristics of hydrogen by use of proton exchange membrane. *J. Power Sources* **164,** 1–8 (2007).

149. Hydropower storage abroad could support the 'energiewende'. *World Energy Council* (2015). at <https://www.worldenergy.org/news-and-media/local-news/hydropower-storage-abroad-could-support-the-german-energiewende-wec-germany-report/>

150. Carmo, M., Fritz, D. L., Mergel, J. & Stolten, D. A comprehensive review on PEM water electrolysis. *Int. J. Hydrogen Energy* **38,** 4901–4934 (2013).

151. Newman, J., Hoertz, P. G., Bonino, C. a. & Trainham, J. a. Review: An Economic Perspective on Liquid Solar Fuels. *J. Electrochem. Soc.* **159,** A1722–A1729 (2012).

152. Feldman, D. *et al. Photvoltaic System Pricing Trends*. (2014). at <http://www.nrel.gov/docs/fy14osti/62558.pdf>